REPORT DOCUMENTATION PAGE

Form Approved
OMB No. 0704-0188

1. REPORT DATE *(DD-MM-YYYY)*	2. REPORT TYPE	3. DATES COVERED *(From - To)*
30-06-2006	Final	April 1, 2004 - March 31, 2006

4. TITLE AND SUBTITLE
Optimizing the Hot-Corrosion Resistance of Novel gamma-Ni+gamma-prime-Ni3Al-Based Alloys and Coatings

5a. CONTRACT NUMBER
N00014-04-1-0368

5b. GRANT NUMBER

5c. PROGRAM ELEMENT NUMBER

6. AUTHOR(S)
Gleeson, Brian

5d. PROJECT NUMBER

5e. TASK NUMBER

5f. WORK UNIT NUMBER

7. PERFORMING ORGANIZATION NAME(S) AND ADDRESS(ES)
Iowa State University
Department of Materials Science & Engineering
2220 Hoover Hall
Ames, IA 50011-2300

8. PERFORMING ORGANIZATION REPORT NUMBER

9. SPONSORING/MONITORING AGENCY NAME(S) AND ADDRESS(ES)
Office of Naval Research
One Liberty Center
875 North Randolph Street, Suite 1425
Arlington, VA 22203-1995
ATTENTION: Dr. Airan Perez

10. SPONSOR/MONITOR'S ACRONYM(S)
ONR

11. SPONSOR/MONITOR'S REPORT NUMBER(S)

12. DISTRIBUTION/AVAILABILITY STATEMENT

DISTRIBUTION STATEMENT A
Approved for Public Release
Distribution Unlimited

13. SUPPLEMENTARY NOTES

14. ABSTRACT

High temperature degradation by hot corrosion (650-1000 C) and/or oxidation (>1000 C) can severely reduce the longevity of advanced gas turbine engine components. The protection of high-temperature components against hot corrosion or oxidation is typically conferred by the application of either a diffusion or overlay metallic coating that is able to form a continuous, adherent, and slow growing oxide scale. There are currently no coatings that provide adequate protection to both hot corrosion and oxidation. This study assesses and advances the performance of novel modified gamma-Ni + gamma-prime Ni3Al alloys and coatings. Significant progress was achieved in this study towards the targeted goal of establishing a metallic coating that is highly resistant to both hot corrosion and high temperature oxidation.

15. SUBJECT TERMS
Hot-corrosion, coatings, liquid salt, high-temperature oxidation

16. SECURITY CLASSIFICATION OF:			17. LIMITATION OF ABSTRACT	18. NUMBER OF PAGES	19a. NAME OF RESPONSIBLE PERSON
a. REPORT	b. ABSTRACT	c. THIS PAGE			Brian Gleeson
U	U	U	UU	105	19b. TELEPHONE NUMBER *(Include area code)* 515-294-4446

ONR Contract No. N00014-04-1-0368

Optimizing the Hot-Corrosion Resistance of Novel γ-Ni+γ'-Ni_3Al-Based Alloys and Coatings

B. Gleeson

Dept. Materials Science and Engineering
2220 Hoover Hall
Iowa State University
Ames, IA 50011-2300

July, 2006

Final Scientific Report: 1 April 2004 – 31 March 2006

Prepared for:
Dr. Airan Perez
Office of Naval Research
One Liberty Center
875 North Randolph Street, Suite 1425
Arlington, VA 22203-1995

ABSTRACT

High temperature degradation by hot corrosion (650-1000°C) and/or oxidation (>1000°C) can severely reduce the longevity of advanced gas turbine engine components. The protection of high-temperature components against hot corrosion or oxidation is typically conferred by the application of either a diffusion or overlay metallic coating that is able to form a continuous, adherent, and slow growing oxide scale. However, as is shown in this study, the resistance of state-of-the-art commercial Pt-modified β-NiAl diffusion aluminides and CoCrAlY-based overlay coatings against both Type I (*i.e.*, 900°C) and Type II (*i.e.*, 705°C) hot corrosion is limited. Thus, there are currently no coatings that provide adequate protection to *both* hot corrosion and oxidation. There is indeed a particular need for such protective coatings because many advanced aero, marine, and industrial gas-turbines operate in both hot corrosion and oxidation regimes in their duty cycle. Gleeson *et al.* [1] recently reported that a wide range Pt+Hf-modified γ'-Ni_3Al + γ-Ni alloy compositions form a thin, planar, adherent, and slow growing Al_2O_3 scale. In fact, the results reported suggest that Pt+Hf-modified $\gamma'+\gamma$ coatings offer a viable superior alternative to β-NiAl(Pt)-based coatings. Thus, a main aim of the present study was to establish and assess optimum target $\gamma'+\gamma$ coating compositions for extending the service life of high-temperature gas turbine components to hot corrosion and oxidation conditions. Both Type I and Type II hot corrosion behavior of the Pt+Hf-modified $\gamma'+\gamma$ alloys were assessed. Quite interestingly, it was found that the Type I resistance of $\gamma'+\gamma$ alloys improved with up to about 10 at.% Pt addition, but then decreased significantly with increasing Pt content up to 30 at.% (the maximum level studied); however, under Type II conditions the resistance of $\gamma'+\gamma$ alloys improved with increasing Pt content up to 30 at.%. To further improve hot corrosion resistance of Pt+Hf-modified $\gamma'+\gamma$ alloys, the effects of systematic additions of Cr, Si, and Cr+Si were assessed. High-temperature oxidation testing of the various modified $\gamma'+\gamma$ alloys was also carried out in air at 1150°C under both isothermal and cyclic oxidation conditions in order to better assess the potential for achieving superior combined resistance to both oxidation and hot corrosion. Finally, the Type I and Type II hot corrosion resistance of novel Pt+Hf-modified $\gamma'+\gamma$-based diffusion coatings developed at ISU were studied and compared with state-of-the-art commercial coatings. The "ISU $\gamma'+\gamma$ coatings" were found to have improved overall resistance to hot corrosion compared to the state-of-the-art commercial coatings. Thus, significant progress was achieved in this study towards the targeted goal of establishing a metallic coating that is highly resistant to *both* hot corrosion and high temperature oxidation.

1. INTRODUCTION

The advancement in high-temperature engineering alloys and coating systems has led to increases in both power and efficiency of gas-turbine engines over the past 60 years. Aero, industrial, and marine gas-turbines also face various harsh operating conditions and surface degradation can occur by not only high temperature oxidation (>1000°C), but also hot corrosion (~ 850-1000°C for type I and 600-800°C for type II) [2]. Of particular concern in this study is hot corrosion, which is an accelerated degradation process that involves deposition of corrosive species (*e.g.*, sulfates, chlorides) from the surrounding environment (*e.g.*, combustion gas to the surface of hot components). The deposition of molten corrosive species is then followed by destruction of the protective thermally grown oxide (TGO) scale, which had formed on the component surface. Salt-induced hot corrosion can be a particularly significant degradation mechanism in marine environments and when a contaminated lower-grade fuel is used. The severity of oxidation and hot corrosion processes in aircraft, land-based power generation, and marine gas-turbines is summarized in Table 1 [3].

Advanced gas-turbines consist of low-pressure turbine (LPT) and high-pressure turbine (HPT) sections, and hot corrosion attack is more frequently observed in the LPT than in the HPT. This is because the LPT sections operate at lower temperatures compared to HPT, thus allowing a significant amount of corrosive contaminants to accumulate on the blade surface [4]. It has also been observed that hot corrosion is usually greatest at the hottest point on the concave surface of the blade, which is about mid-way along the length of the blade [4]. Hot corrosion attack on gas-turbine materials can be reduced to a certain extent with the use of high quality fuels and improved filtration systems. However, for both cost and practical reasons, these are not reliable solutions. The more appealing option is to improve the hot corrosion resistance of turbine blade material itself.

Superalloys used for gas turbine blades and vanes encompass a large group of metals which have improved strength at higher operating temperatures. The improvements in the strength of superalloys corresponded to additions of elements such as W, Mo, Ta, Ti, which confer poor hot corrosion and oxidation resistance. Hence, in

gas-turbines the superalloy components are usually protected by a diffusion or overlay metallic coating that is able to form a protective α-Al_2O_3 scale [5].

The most widely used diffusion coatings are based on the aluminide β-NiAl, while overlay coatings are typically based on an MCrAlY composition in which M represents Ni, Co, or Ni + Co. The performance of coatings depends upon their chemical composition and microstructure. The use of protective coatings and high-quality aviation fuels does not usually cause extensive degradation of the coated superalloy systems below about 5,000 hours, at least in aircraft engines [6]. However, for flights in marine atmosphere at lower altitude or for shipboard turbines the life expectancy dramatically drops below 5,000 hours.

Table 1. Comparison of severity of degradation mechanisms for various gas-turbine engine applications [3].

Gas-turbine engine application	**Oxidation**	**Hot corrosion**	**Interdiffusion**
Aircraft engines	Severe	Moderate	Severe
Land-based industrial power generation engines	Moderate	Severe	Moderate
Marine gas-turbine engines	Moderate	Very Severe	Light

The quest for higher component operating temperatures in gas-turbine engines was mostly dominated by superalloy processing technology until the past 20 years. The development of thermal barrier coating (TBC) systems coupled with modern cooling systems has allowed for an almost 150°C reduction at the superalloy blade surface temperature thereby allowing the gas-turbine engine combustion temperature to be above the melting temperatures of superalloys [7]. As shown in figure 1, technological developments in superalloys have led to a progressive increase in the operation temperatures of the gas-turbine components [8]. The major mode of TBC failure is delamination of the outermost ceramic layer from the underlying metallic bond coat [7]. The hot corrosion and oxidation behavior of the metallic bond coats has a major impact on the life of a TBC.

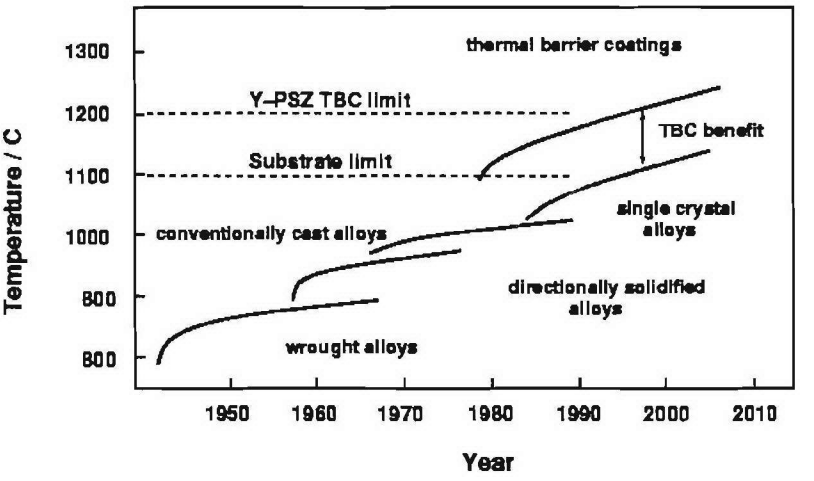

Figure 1. Increase in operational temperature of turbine components [8].

The purpose of this study is to assess in a systematic manner the hot corrosion and oxidation behavior of novel Pt+Hf-modified $\gamma' + \gamma$ alloys and coatings in order to gain a better fundamental understanding of the effects of $\gamma' + \gamma$ composition and assemblage on degradation behavior. A targeted significant outcome of this study is the establishment of an optimum coating composition that is highly resistant to *both* hot corrosion and oxidation.

2. TECHNICAL BACKGROUND

2.1 Superalloys in Gas-Turbine Engine

Superalloys are Ni-, Co-, and Fe-based alloys based on the face centered cubic (FCC) crystal structure and are generally used at elevated temperatures as the blades and vanes in the turbine section of an engine. Ideally, they provide high-temperature strength and resistance to both hot corrosion and oxidation. Superalloys have solubility for various elements, thus allowing a wide range of alloys with different properties. Strengthening of superalloys is achieved by solid-solution hardening (by substituting elements with slightly different atomic diameter, *e.g.* Co, Fe, Mo, W, V, Ti, Al), precipitation hardening (by forming precipitates such as γ'-$Ni_3(Al,Ti)$), and by formation of a carbide-dispersion (by favorable distribution of carbides). The latter is particularly the case for Co-based alloys. The upper temperature limit of superalloys depends upon the melting

temperature and dissolution of the strengthening phases. Superalloys are available in cast or wrought (usually heat treated or processed) forms. Developments in casting technologies made it possible to produce directionally-solidified and single-crystal superalloys (figure 1).

2.2 High-Temperature Protective Coating Systems

2.2.1 High-Temperature Surface Protection

A metallic coating improves reliability and durability of turbine blades in harsh operating temperatures, under thermal cycling and in aggressive environments, thus enabling higher efficiencies and longer operating lifetimes [6]. Metallic coatings are preferred for the surface protection of superalloys because coatings can be tailored for the surrounding aggressive environment. This in turn allows for the development of superalloy substrates with much improved strength. Application of a coating also provides an opportunity to refurbish worn surfaces after some time in service, allowing the use of superalloy substrate for extended operating lifetimes before replacement.

Advanced high-temperature protective coatings must provide adequate resistance to both oxidation and hot corrosion, while being chemically and mechanically compatible with the superalloy substrate. Apart from providing environmental protection, coatings should exhibit the following characteristics [2-15]:

- be well bonded to the substrate
- ability to form a thin, continuous, slow-growing, and adherent thermally grown oxide (TGO) scale
- be self-healing in forming a protective TGO scale
- does not degrade the mechanical properties of the superalloy substrate
- has high-temperature diffusional stability
- be ductile enough to withstand substrate deformation without cracking

Protective coatings on superalloys do not function as inert barriers, but rather they provide protection by interacting with oxygen in the aggressive environments to form a dense, continuous and adherent TGO scale. The TGO layer often acts as a diffusion product layer that inhibits inward diffusion of oxidizing species such as oxygen and sulfur and outward diffusion of metal species. Finally, the TGO layer should not crack or spall during thermal cycling. Therefore, protective coatings must be rich in elements like

Al, Cr or Si, which participate in the formation of protective oxide scales of Al_2O_3, Cr_2O_3, or SiO_2, respectively. Among these oxides, Cr_2O_3 is not suitable above about 950°C, especially in high-velocity gases, due to formation of volatile CrO_3 [9]. Silica-forming ceramic coatings (SiC, Si_3N_4) are deposited on carbon-based materials at higher temperatures (> 1000°C) [10]; however, the use of silica-forming metallic coating on superalloys is limited. A metallic coating must contain a large amount of silicon in order to form an SiO_2 scale. Silicon in a coating tends to diffuse rapidly into the substrate, forming low melting phases and brittle silicides by interacting with the superalloy substrate. Hence, most high-temperature protective coatings are Al_2O_3 formers. The growth rate of the Al_2O_3 scale the forms generally determines the life for coatings, since this (together with coating/substrate interdiffuson) controls the rate and extent of aluminum depletion from the coating.

In Al_2O_3-forming coatings, silicon and chromium additions have been found to be beneficial in improving oxidation and hot corrosion resistance [2-5,13-15]. Chromium addition in the coating decreases the amount of aluminium required for the formation of an Al_2O_3 scale [17]; but the development of advanced single-crystal superalloys with improved strength meant reductions in chromium and silicon contents. The scale growth and spallation rates can be controlled by small additions of reactive elements such as yttrium, cerium, hafnium and zirconium [18-20]. Precious-metal additions such as platinum, palladium, and ruthenium are also known to improve oxidation and hot corrosion resistance [21-24]. Addition of platinum in the diffusion aluminide coating promotes the formation of a slow growing, continuous, and adherent oxide scale [20].

2.2.2 Coating Processes

Superalloy coating processes are often divided into two main categories: one involves the reaction of an outer surface layer from reactive chemical vapor deposition with the selective chemical species (*i.e.* diffusion coating process) and the other involves deposition of metallic species with desired protective compositions onto the substrate (*i.e.* overlay coating process). There are various factors that influence the coating selection process in advanced gas turbine, and these include [2-16]:

1. Gas and deposit composition

2. Gas and/or deposit and superalloy temperature
3. Thermal cycling
4. Superalloy specimen geometry, since overlay coatings are line-of-sight process
5. Superalloy composition
6. Required protection time and cost of the coating deposition process
7. Gas pressure and velocity
8. Possible effects of the coating process on the mechanical and thermal properties of the superalloy substrate
9. Effects of interdiffusion between the coating and superalloy substrate during the high-temperature exposure

Conventionally cast, directionally solidified or single crystal superalloy substrates in high- and low-pressure turbine components are often protected against oxidation and hot corrosion using a Pt-modified diffusion aluminide or a MCrAlY (where M is Ni, Co or Ni + Co) overlay coatings. A short summary of these coatings is presented in the next section, while more comprehensive reviews about the various types of coatings can be found in the references [11-15].

2.2.2.1 Diffusion Coatings

Coating processes which involve enrichment of Al, Cr, and Si via diffusion process into the superalloy surface are widely used in industry. Diffusion coatings can be applied on gas turbine engine components using various techniques such as slurry cementation, powder pack cementation, and chemical vapor deposition (CVD).

A pack cementation process is itself a type of CVD process that involves both the component and the powder reactants in a same semi-sealed retort. The "pack" of powder reactants mixture consists of Al/Cr/Si and/or other element-powder, a halide (*e.g.* NH_4Cl) as a chemical activator, and inert filler (*e.g.* Al_2O_3). The retort is then placed in the furnace in an inert atmosphere and on heating the metal powder reacts with the activator to form a vapor that in turn reacts with the surface of the superalloy thereby enriching it with the metal to be coated [6]. The most commonly used diffusion based β-NiAl coatings by pack cementation process can be classified as either low-activity (outward growing) or high-activity (inward growing) coatings. Low-activity β-NiAl coatings are

formed by the predominant outward diffusion of nickel, while high-activity coatings are formed by the predominant inward diffusion of aluminium [6]. In pack aluminizing of Ni-based alloys the phases of interest are NiAl, Ni_3Al, and Ni_2Al_3. The final phase structure of the coating can be controlled by the concentration and temperature of the pack constituents and the time and temperature of the post-heat treatment. A further factor that influences the properties of aluminide coating is the variation in the substrate composition. As a consequence a different processing methodology is often required for each superalloy to obtain desired coating results.

Modified aluminide coating can be prepared by depositing another layer prior to the aluminizing process or by co-depositing elements from pack or slurry. For example, chromizing is performed prior to the aluminizing process to develop chrome-modified aluminide coatings with improved hot corrosion resistance; however, their oxidation resistance is rather poor [70]. Similarly Si-modified aluminide coatings can be produced using slurry or process to produce $CrSi_2$-dispersed β-NiAl coatings, which exhibit improved hot corrosion resistance [25]. A significant advancement in the diffusion coating processes was made with the inclusion of noble metal-Pt in the aluminide coatings (Pt-modified β-NiAl coatings). Platinum-modified aluminide coatings are now widely used in the gas turbine industry, outperforming most of the other diffusion aluminide coatings under the cyclic oxidation and hot corrosion conditions [3-6]. A commercially used Pt-modified aluminide coating is prepared by electroplating 5-10 μm platinum into the superalloy surface followed by heat treatment process prior to the pack cementation aluminizing treatment. A typical coating composition of Al-rich Pt-modified β-NiAl coating is Ni-(38-42 at%)Al-(8-10 at%)Pt and its microstructure is shown in figure 2 (a). Pt-modified aluminides are also widely used in thermal barrier coatings as the bond-coat with an electron beam physical vapour deposition (EBPVD) ceramic coat as the top-coat. More detailed discussion about the pack cementation process can be found elsewhere [6, 16].

Recently, Gleeson *et al.* [26] at ISU developed a novel Pt(+Hf)-modified γ′-Ni_3Al + γ-Ni coating using the pack cementation deposition technique. The coating has a nominal composition of Ni-(20-22 at%)Al-(15-20at%)Pt-1wt%Hf and consists primarily of γ′, figure 2 (b). The phase structure of the coating is more compatible with the

substrate ($\gamma+\gamma'$), thus reducing the undesired topologically closed packed (TCP) phases in the interdiffusion zone. The brittle TCP phase in the coatings decreases the strength of the superalloy-coating system. Therefore, Pt(+Hf)-modified γ'-Ni_3Al + γ-Ni coatings are more suitable for advanced gas-turbine engine components from a mechanical standpoint. Preliminary results indicate that the Pt(+Hf)-modified γ'-Ni_3Al + γ-Ni coatings exhibit excellent oxidation resistance and offer superior viable alternative to the current state-of-art β-NiAl(Pt)-based diffusion coatings. However, hot corrosion resistance of these coatings is not established and is the main focus of the current research.

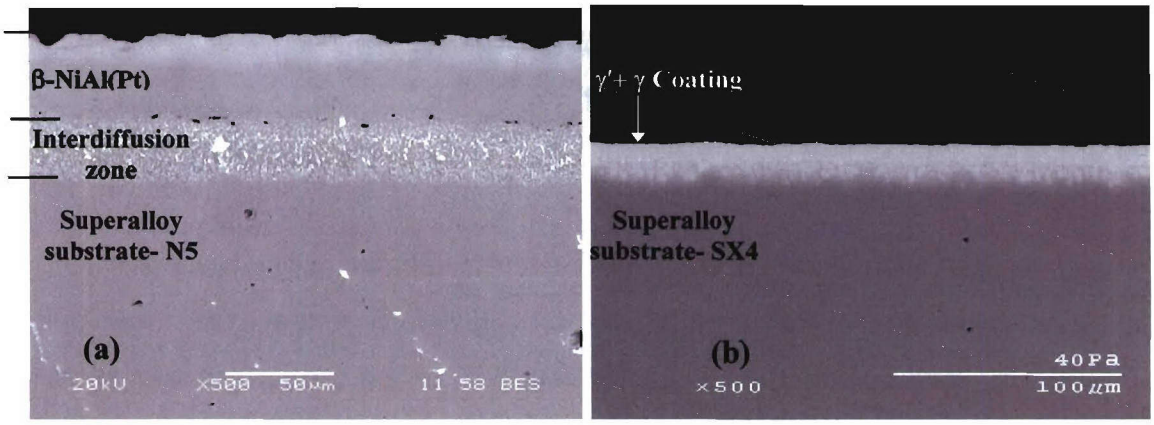

Figure 2. As-deposited diffusion aluminide coatings: (a) Commercially used Pt-modified β-NiAl coating [Ni-(38-42 at%)Al-(8-10 at%)Pt] (b) Pt+(Hf)-modified γ-Ni+ γ'-Ni_3Al coating [Ni-(20-22at%)Al-(15-20 at%)Pt-0.5 at%Hf] developed at ISU

2.2.2.2 Overlay Coatings

Diffusion based coatings have excellent oxidation resistance, but rather poor Type I hot corrosion resistance. To combat this problem, research led to the development of MCrAlY overlay coatings. The final composition of a diffusion coating is dependent on the substrate composition; hence it is intrinsically difficult to obtain an ideal coating composition of optimum oxidation and hot corrosion resistance with improved ductility. In MCrAlY type overlay coating a pre-alloyed material with composition required to form protective TGO layer is applied to the superalloy surface by processes that require interdiffusion to ensure that the coating is metallurgically bonded to the substrate. In MCrAl overlay coating composition is selected to give optimum environmental resistance

and ductility, while the active element Y is added to improve the oxide scale adhesion and to decrease oxidation rates. Most commonly used overlay coating processes are EBPVD and plasma spraying.

In physical vapor deposition, the required deposit composition is achieved from the vapor of a source and there is no need for chemical reaction between the substrate and the coating. The EBPVD process specifically involves vaporization of an ingot of the selected coating composition in a vacuum using focused electron beam as the evaporation source. The composition of the deposited coating will often be different from the ingot due to the differences in vapor pressures of the elements and the composition of the ingot must therefore be adjusted accordingly. With the advancements in EBPVD coating technology, elements with a wide range of vapor pressure can be evaporated from a single source. More detailed information about the EBPVD process is presented elsewhere [27]. A typical coating microstructure of as-deposited CoCrAlY with nominal coating composition of Co-25Cr-14Al-0.5Y is shown in figure 3. The phase structure of CoCrAlY coating shows the precipitation of β-CoAl in a γ-matrix the cobalt solid-solution. The post-heat treatment is used to bond the coating and the substrate with the creation of a limited interdiffusion zone. The structure and composition of the CoCrAlY coating is constant throughout its thickness. The phase orientation in the as-deposited EBPVD coating is perpendicular to the substrate due to the nature of the process.

Air plasma spraying is a thermal spray method in which an electric arc creates plasma that can reach temperatures of more than 1600°C. The plasma spraying process involves injection of pre-alloyed coating material into a high-temperature plasma where it is fully melted and propelled towards the substrate. The molten particles impact the substrate surface and are rapidly solidified, forming a continuous but typically porous coating. With the help of high-temperature plasma it is possible to spray any material of tailored compositions and microstructures. The structure, composition and properties of a given coating are influenced by various factors such as the amount of preheat, plasma gun characteristics and gun to workpiece distance. Advancements in plasma spraying technology have made it possible to spray coatings in low-pressure vacuum chambers. This type of technique is known as low-pressure plasma spraying (LPPS) and is used for spraying MCrAlY coatings, as it minimizes the formation of oxide defect within the as-

deposited coating structure. The advantages of LPPS also include higher powder particle velocities and broader spraying patterns. Plasma spraying coatings can also be applied in an inert gas shroud, especially Ar. A typical structure of NiCrAlY coating with a YSZ top coat is shown in figure 4. Plasma spraying process gives more compositional flexibility compared to the EBPVD process because vapor pressure of the coating elements is not an issue in the plasma spaying process. A detailed overview of plasma spraying process can be obtained from the reference [28].

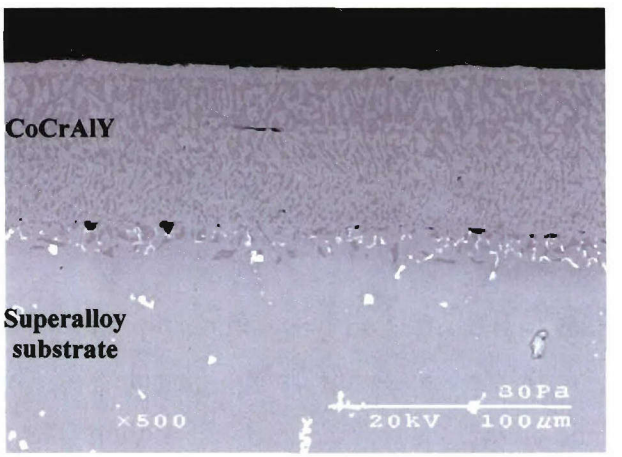

Figure 3. As-deposited CoCrAlY (Co-25Cr-14Al-0.5Y) overlay coating deposited by EBPVD process.

As-deposited overlay coatings when compared to diffusion coatings have little or no interdiffusion zone between the coating and the substrate, hence mechanical properties of the superalloy substrate are initially unaffected in the case of overlay coatings. Overlay coatings by plasma spraying or EBPVD show improved hot corrosion resistance than diffusion aluminides [3-5, 11-15]; however, both types of overlay coatings are line of sight processes and it is quite difficult to obtain uniform coating thickness for the complex shapes of turbine blades or vanes. Moreover, the internal cooling passages of the airfoils can not be coated using the overlay coating processes. Another disadvantage of overlay coatings is that coating processes are more expensive than the diffusion coating processes.

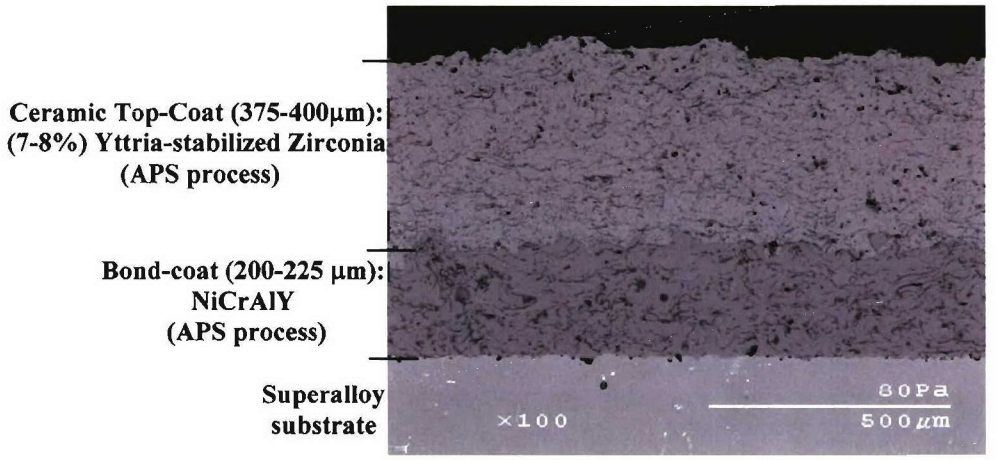

Figure 4. As-deposited NiCrAlY (Ni-25Cr-14Al-0.5Y) overlay coating (LPPS) with YSZ top coat (APS) both deposited using plasma spraying processes.

2.2.2.3 Miscellaneous Coatings

Coatings similar to the diffusion type can also be produced by an electrophoretic deposition process. In this process fine metal particles of desired composition are electrodeposited by immersion of substrate into the solution. The coated substrate is then subjected to a diffusion heat treatment in a protective atmosphere to produce a coating structure similar to diffusion aluminides (figure 5). Creech *et al.* [29] developed an electrophoretic process for the co-deposition of Pt and Si on Ni-based superalloys with or without additions of other minor elements. Electrophoretic deposition differs from electroplating in that particles of any composition rather than just ions can be deposited. Compared with physical vapor deposition, electroplating, spraying or dipping, the electrophoretic process is deemed to be the most suitable method for coating non-uniform geometries; however, it is still not better than diffusion aluminide coatings for depositing internal passages of airfoils

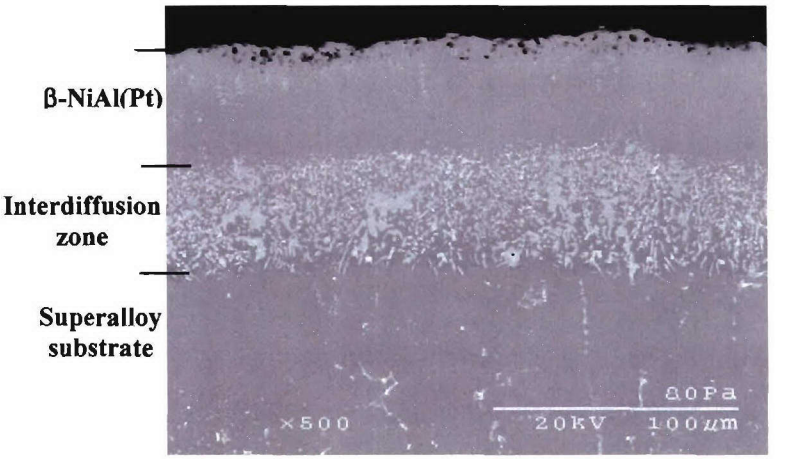

Figure 5. As-deposited Pt-modified β-NiAl coating [Ni-(36-40 at%)Al-(6-8 at%)Pt] deposited by electrophoretic process.

2.2.2.4 Thermal Barrier Coatings

Thermal barrier coatings (TBCs) are the most promising development in superalloy coatings research and they have been in use in gas-turbine aero engine hot sections for the past 20 years. TBCs consist of a top coat made of low-thermal conductivity ceramics which provides thermal insulation to metallic components from the hot gas stream in the gas-turbine engines. The use of a TBC and advanced cooling systems enables modern-gas turbine engines to operate at combustion gas temperatures well above the superalloy melting point by providing temperature reductions of up to at least 150°C in the superalloy surface temperature (figure 6) [7, 30]. Alternatively, TBC's provide extra protection to superalloy components from foreign object damage (*i.e.* erosion and impact damage) and extreme environmental conditions (*i.e.* hot corrosion) thereby improving engine efficiency and materials performance. Recently, Padture *et al.*[7] and Gleeson [30] presented reviews on TBC's for gas-turbine engine applications.

Typically, the structure of advanced TBC systems consists of two layers– a ceramic top-coat (100-400 μm) and an underlying metallic bond-coat (50-225 μm). The metallic bond-coat layer provides environmental resistance against the oxidation and even hot corrosion. The bond coat is usually applied either by a diffusion or overlay process. The metallic bond-coat application procedure and compositions are similar what

was described in the earlier sections of diffusion and overlay coating application processes. The ceramic top-coat layer provides thermal insulation and is made of yttria-stabilized zirconia (YSZ).

Pure zirconia undergoes the following transformations:

$$\text{Monoclinic} \xleftrightarrow{1170^{\circ}C} \text{Tetragonal} \xleftrightarrow{2370^{\circ}C} \text{Cubic}$$

The $t \rightarrow m$ transformation on cooling is martensitic in nature and can result in cracking due to volume change (4-5%).Thus certain stabilizers such as Y_2O_3, MgO, CeO_2, Sc_2O_3, In_2O_3 and CaO are used to inhibit this transformation; however, 7-8% Y_2O_3-stabilized zirconia found most suitable for the TBC applications [7, 30]. At lower levels of yttria, t-phase of YSZ transforms to a mixture of m-YSZ and c-YSZ and the $t \rightarrow m$ may still exist, as shown in ZrO_2-Y_2O_3 phase diagram (figure 7) [31]. With the additions of about 7-8% yttria and the rapid deposition rate of the top-coat, the deposited YSZ exists in a closely related but metastable t′ phase rather than the stable t phase. The metastable t′ phase is more suitable for TBC applications because t′-YSZ phase does not undergo any transformation on cooling and is stable even at room temperature [31].

YSZ has a low thermal conductivity, high oxygen permeability, high melting temperature (~2700°C), high-temperature stability, thus making it a natural material choice for the ceramic top-coat layer. To accommodate more stresses induced by thermal-expansion mismatch and thermal shock, YSZ is made strain tolerant by introducing numerous pores and pathways. A typical example of a TBC system with EBPVD top-coat (125-150μm) and diffusion aluminide (Pt-modified β-NiAl: 60-70μm) bond-coat is shown in figure 8.

The metallic bond-coat is sufficiently rich in Al to form a TGO scale of α-Al_2O_3 during the top-coat deposition process and during oxidation. In addition to imparting oxidation/hot corrosion resistance, the TGO serves to bond the ceramic top-coat and metallic bond-coat. In general, it has been also found that TGO failure (*i.e.* spallation and/or cracking) is the ultimate cause of failure mechanism of commercial TBC systems [30]. As a consequence the durability and reliability of TBC systems is critically dependent on the TGO scale. The ideal TGO scale for the TBC system should be

continuous, slow-growing, thin, and adherent to both ceramic top-coat and metallic bond-coat.

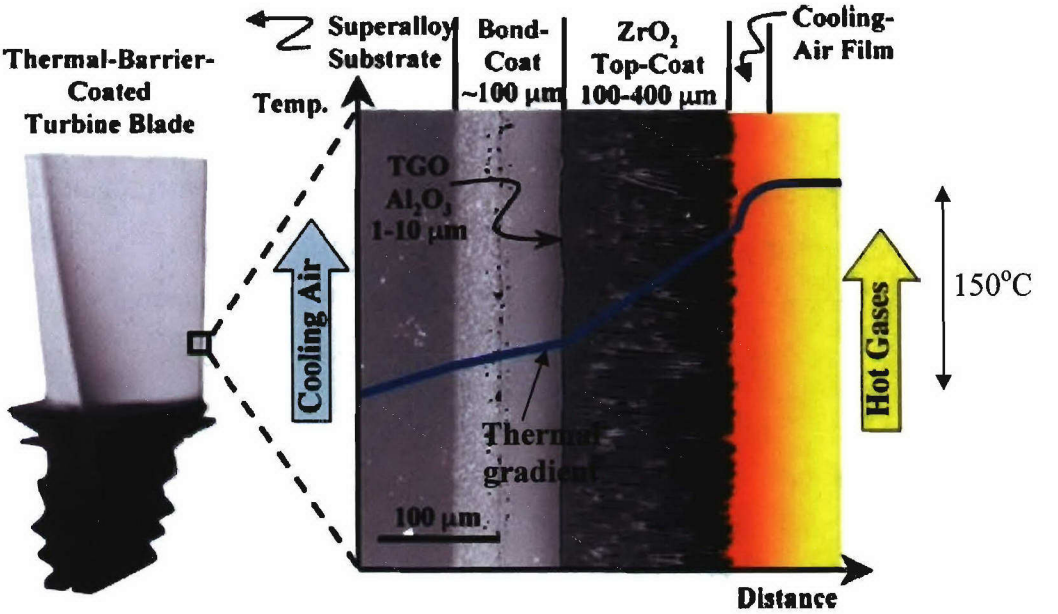

Figure 6. A cross-sectional SEM image of TBC system showing thermal gradient (70-150°C) produced within the various TBC layers [7, 30].

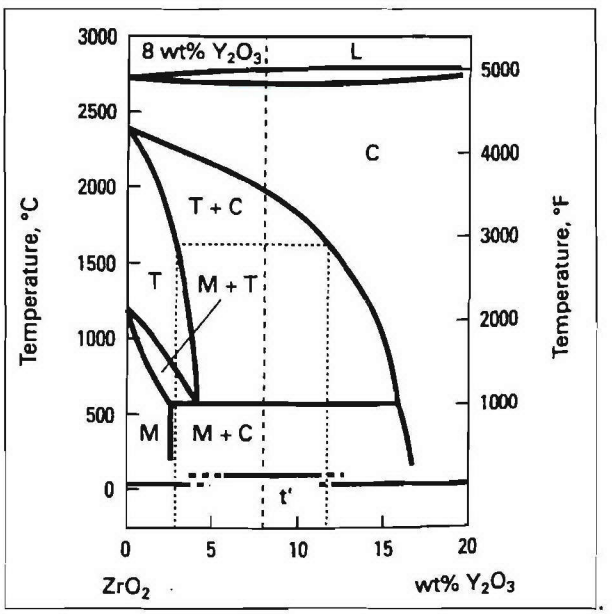

Figure 7. Phase diagram of Zirconia-Yttria system [31].

The initial Al-rich metallic coatings have the Al_2O_3 re-healing capacity, which is an important criterion for metallic coatings; however, in the TBC system, initial spallation of TGO is responsible for the failure of ceramic-top coat. Platinum enrichment in the aluminide coating improves the Al_2O_3 scale adhesion making it an ideal candidate for the metallic bond-coat in the TBC systems. Recently it was discovered that Pt-modified β-NiAl coatings and alloys may undergo martensitic transformation resulting in the continuous surface undulations during thermal cycling [32]. These surface undulations known as "rumpling" may result in the delamination of the top-coat. Rickerby *et al.* [33] and Gleeson *et al.* [26] have developed novel bond-coats that have γ-Ni+ γ′-Ni_3Al phase structure making it more compatible with the superalloy substrate than the current state-of-the-art MCrAlY and Pt-modified β-NiAl coatings. These novel bond-coat structures may help in the development of next-generation TBC systems extending the operating life times.

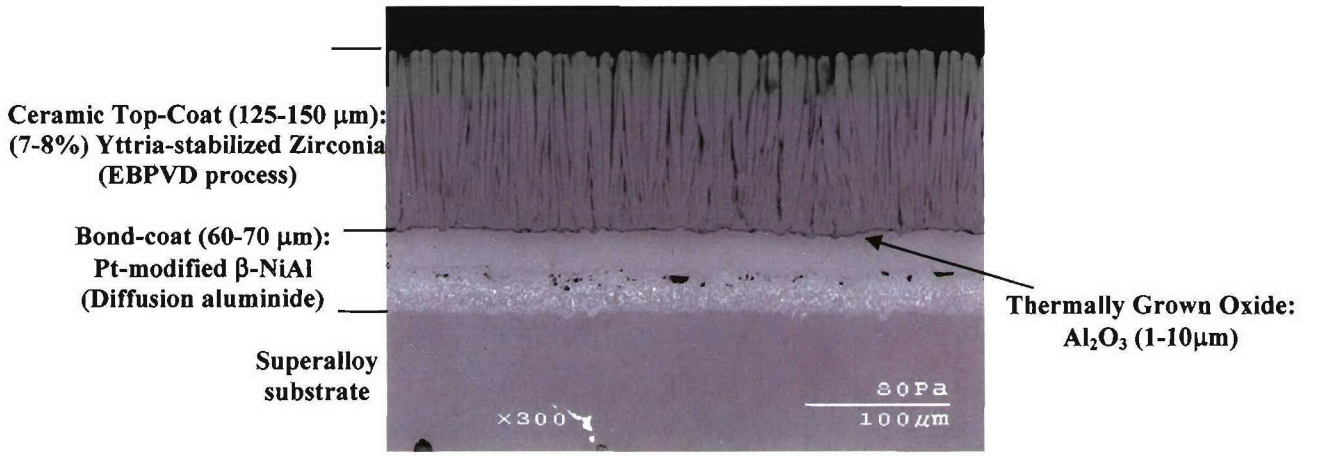

Figure 8. An example of TBC system showing cross-sectional SEM of YSZ top-coat (EBPVD process), thermally grown oxide-Al_2O_3, Pt-modified aluminide bond-coat (diffusion process), and superalloy substrate.

2.3 Background on Hot Corrosion

2.3.1 Mixed Oxidant Corrosion

Materials used in high temperature applications encounter variety of corrosive environments containing two or more oxidizing components. CO, CO_2, H_2O, SO_3/SO_2, N_2, halogens, and molten alkali salts are the most common types of mixed oxidants other than O_2 that industrial applications encounter. Coking, nitridation, chlorination, sulfidation, and hot corrosion are some of the high temperature degradation mechanisms that occur due to exposure to mixed oxidizing reactants. The presence of these secondary oxidants affects oxidation behavior of an alloy resulting in corrosion products which are less protective than the protective TGO layer.

Molten-salt-induced hot corrosion is the focus of current research. It is an accelerated form of oxidation that is induced by the presence of a thin layer of molten oxidants on the surface of metals and alloys. It occurs in various advanced gas turbine engine components.

2.3.2 Formation of Na_2SO_4 in a Gas Turbine Environment

The molten oxidants in marine gas turbine environments are primarily composed of sulfates of alkaline earth metals. The sea environment is the primary source of these corrosive salts. Sea salt enters gas turbine engines as an aerosol and also as a fuel contaminant. It has been found that Na_2SO_4 alone or combined with K_2SO_4, $CaSO_4$, $MgSO_4$ and NaCl causes hot corrosion attack of gas turbine engine components [2, 34, 35]. Na_2SO_4 is a minor constituent of sea salt, and is not found easily in air. Both coal and aviation fuel oils contain varying amounts of sulfur, which on combustion forms SO_2 and SO_3. Dew point calculations showed that NaCl present in the form of vapor under the gas turbine engine conditions [34]. Sodium sulfate is formed when NaCl reacts with SO_2/SO_3, oxygen and/or water in the following manners:

$$2NaCl + SO_3{:}SO_2 + O_2{:}1/2O_2 \rightarrow Na_2SO_4 + Cl_2 \qquad (1)$$

$$2NaCl + SO_3 + H_2O \rightarrow Na_2SO_4 + 2HCl \qquad (2)$$

$$2NaCl + SO_2 + H_2O + 1/2\ O_2 \rightarrow Na_2SO_4 + 2HCl \qquad (3)$$

DeCrescente and Bornstein [34] studied the formation and thermodynamic stability of Na_2SO_4 in gas turbine engine environment and calculated equilibrium constants for the

above reactions. They showed that the complete conversion of NaCl to Na_2SO_4 is possible in a gas turbine engine atmosphere.

2.3.3 Hot Corrosion Characteristics: temperature dependence and microstructural appearance

Typically there are two different forms of hot corrosion mechanisms that are reported for gas turbine engine components. Depending upon temperature and their microstructural appearance, hot corrosion is divided into Type I (high-temperature hot corrosion) and Type II (low-temperature hot corrosion) hot corrosion. The temperature dependence and corrosion rates of these forms of hot corrosion are compared with oxidation rate in figure 9 [35]. Both forms of hot corrosion depend upon various factors such as salt composition and its melting temperature, alloy composition, gas composition, salt flux rate, thickness of salt scale, temperature and thermal cycles, thickness, and composition of thermally grown oxide (TGO) scale.

2.3.3.1 Type I-High Temperature Hot Corrosion (HTHC)

Type I hot corrosion mainly occurs at a higher temperature range between 850-950°C [35, 36]. The microstructural appearance of Type I hot corrosion is characterized by a broad corrosion front with internal oxides beneath the porous non-protective external oxide scale. Internal sulfides are typically observed below the internally oxidized zone. Depletion of reactive elements (e.g. Al and Cr) and enrichment of noble elements such as Pt (if present) is also observed beneath the oxide scale. A schematic representation of microstructural appearance with various zone distributions is shown in figure 10 (a). An SEM image of a Pt-modified β-NiAl after 100 hours of exposure under Type I conditions at 900°C is shown in figure 10 (b). Type I corrosion is characterized by a change in surface color (*e.g.* green color in Ni-based alloys due to the formation of NiO), severe cracking and a substantial weight gain. Type I hot corrosion in alloys and coatings occurs above the melting temperature of the salt deposit. The most significant source of Type I hot corrosion is Na_2SO_4 (T_{melt} = 884°C) [39]; however, its melting point can be lowered by addition of other impurities such as vanadium, chlorides and other sulfate mixtures, thus broadening the range of Type I hot corrosion. For instance, Na_2SO_4 combined with dissolved salts like $CaSO_4$ and $MgSO_4$ forms an eutectic with a melting point as low as 650°C [37]. Na_2SO_4 also forms an eutectic with NaCl (T_{melt} = 620°C) that is present in the

marine atmosphere [35]. Vanadium present as an impurity in low-grade fuel oils forms vanadium oxides upon combustion. Sodium vanadates formed by the reaction between V_2O_5 and Na_2SO_4 have lower melting point than the pure Na_2SO_4. It is possible to form various salt deposits with lower melting temperatures; however, proto-typical salt, Na_2SO_4, was used in the present study.

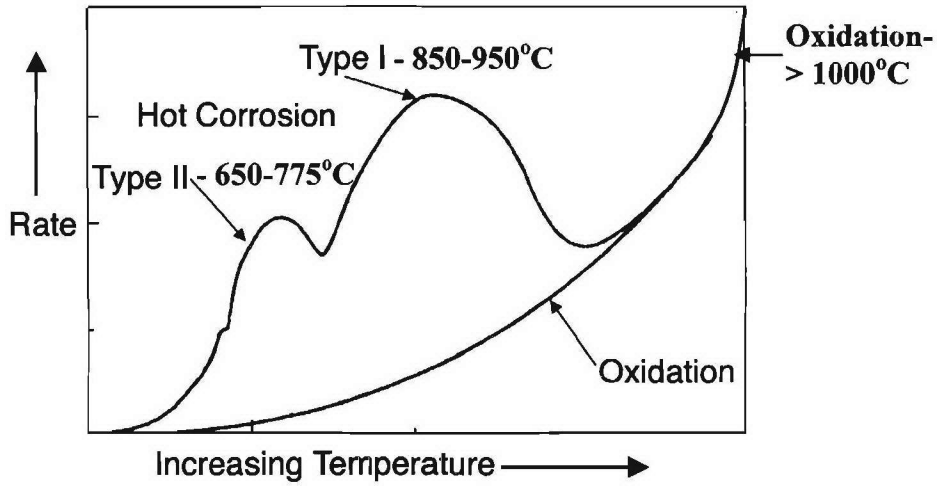

Figure 9. A schematic of comparison between temperature dependence and corrosion rates produced by the two forms of hot corrosion and oxidation [35].

2.3.3.2 Type II-Low Temperature Hot Corrosion (LTHC)

Typically Type II hot corrosion occurs at a lower temperature range between 650-775°C [35, 36, 38]. This form of degradation is often characterized by a pitting attack at least during the initial stage. The microstructural appearance reveals internal voluminous oxides with very little or no internal sulfides and depletion zone. A schematic representation and SEM image (Pt-modified β-NiAl) of Type II hot corrosion is shown in figure 11. Liquid formation of salt deposit in Type II hot corrosion depends upon the alloy underneath and also on the surrounding gaseous environment. Type II hot corrosion occurs at least 125°C below melting temperature of Na_2SO_4 and liquid formation of deposit is generally believed to be due to eutectic Na_2SO_4-MSO_4 (where M is Co or Ni). Both eutectic (Na_2SO_4-$NiSO_4$ → T_{melt} = 671°C and Na_2SO_4-$CoSO_4$ → T_{melt} = 565°C) temperatures are below 700°C. $CoSO_4$ and $NiSO_4$ can be formed from the following reactions in Co- and Ni-based alloys,

$$CoO\,(s) + SO_3\,(g) \rightarrow CoSO_4\,(s) \quad (4)$$

$$NiO\,(s) + SO_3\,(g) \rightarrow NiSO_4\,(s) \quad (5)$$

In these reactions a higher P_{SO_3} is required for the formation of an eutectic Na_2SO_4-MSO_4 at lower temperatures. SO_3 and SO_2 are more stable in Type II than in the Type I temperature range, as their stability decreases with increase in temperature. It should be noted that ΔG_f for the $SO_2 + 1/2\ O_2 \rightarrow SO_3$ reaction suggests that the reaction is possible only in the Type II temperature range (< 780°C). Such aggressive high temperature degradation mechanisms (Type I and Type II hot corrosion) involve breakdown of protective reaction product barrier followed by dissolution of an oxide by what is referred to as a "fluxing" action. Hot corrosion degradation by such fluxing reactions and models describing these reactions are explained in detail in the next few sections.

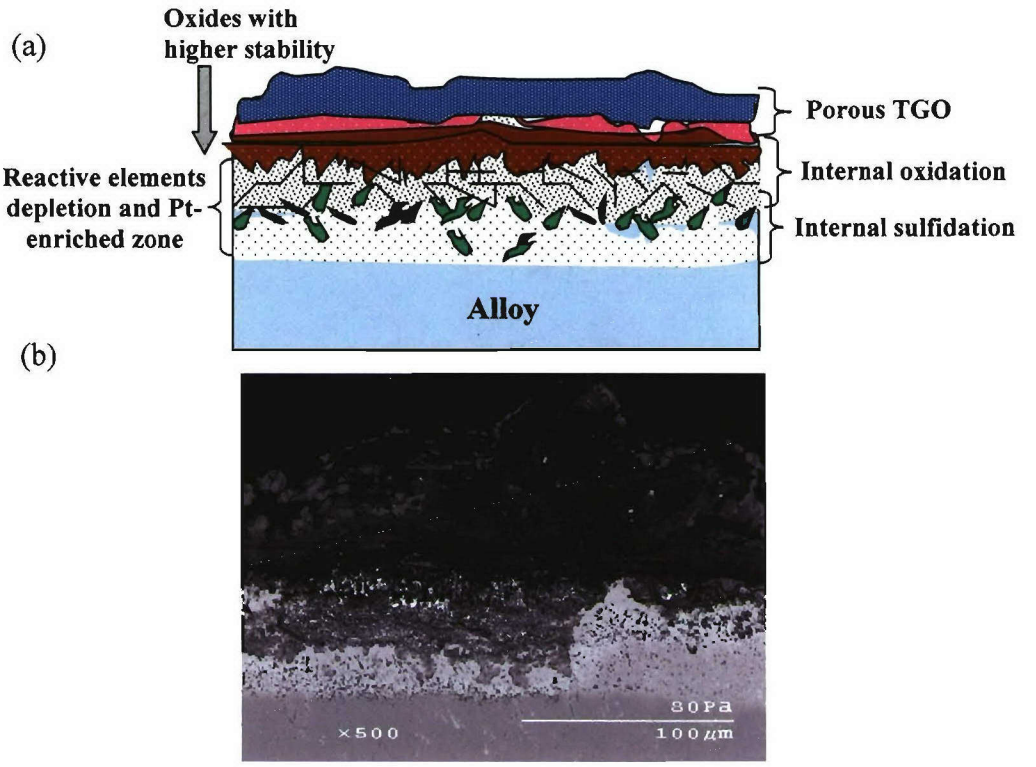

Figure 10. (a) A schematic of microstructural appearance showing zone distribution in Type I hot corrosion (b) SEM image showing Type I hot corrosion in Pt-modified β-NiAl coating on Ni-based superalloy.

(a)

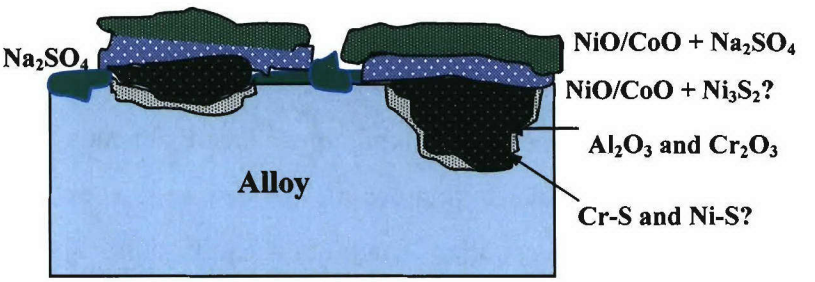

(b)

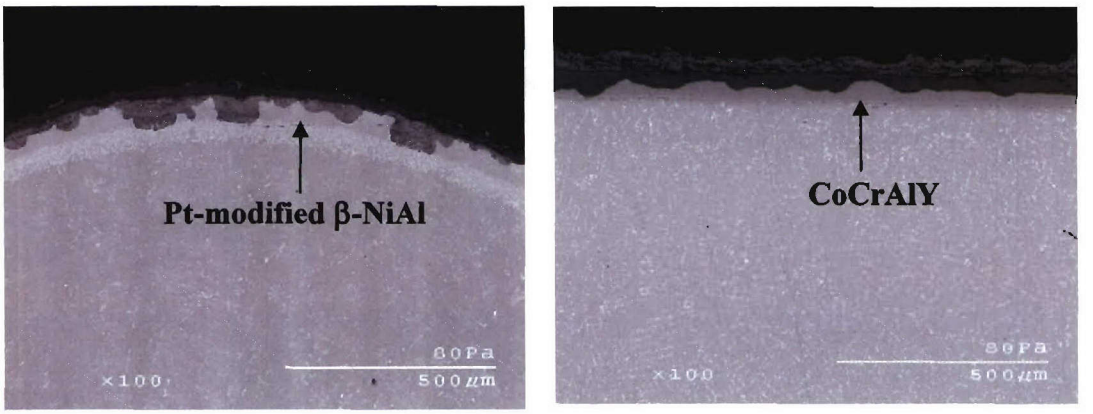

Figure 11. (a) A schematic of microstructural appearance showing zone distribution in Type II hot corrosion (b) SEM image showing Type II hot corrosion in Pt-modified β-NiAl and CoCrAlY coating.

2.3.4 Deposit Induced Degradation-Salt Fluxing Reactions

Thermodynamic phase stability diagrams are quite useful in describing any compositional changes that may occur in the deposit. For instance, in hot corrosion, metal-sulfur-oxygen stability diagrams delineate the stability regions of the various phases that may exist for different activities of the oxidants. High temperature stability diagrams are quite similar to Pourbaix diagrams in aqueous environments [39]. The 900°C phase stability diagram for the Na-O-S [39] system in figure 12 illustrates various phase stability regions that are present when Na_2SO_4 is in contact with the oxide or metal. Activities of O_2 and SO_3 are used as coordinates, where activity of SO_3 can be replaced with Na_2O activity in the same figure, in accordance with the equilibrium,

$$Na_2SO_4 \rightarrow Na_2O + SO_3 \qquad (6)$$

The acidity of the molten salt is expressed as log (PSO_3) and the basicity as log (aNa_2O). The deposit may become more basic due to an increase in the oxide ions concentration *i.e.* activity of Na_2O is increased or it may turn more acidic if the oxide ion concentration is decreased *i.e.* PSO_3 is increased. A fluxing mechanism depends upon the oxide ion concentration in the melt. Acidic fluxing occurs when oxide ion concentration in the melt is low compared to the value required to maintain equilibrium. The acidic dissociation reaction is given as,

$$MO = M^{2+} + O^{2-} \qquad (7)$$

Similarly in basic fluxing oxide ion activity is high compared to the value required to maintain equilibrium and forms a complex anion as shown below,

$$MO + O^{2-} = MO_2^{2-} \qquad (8)$$

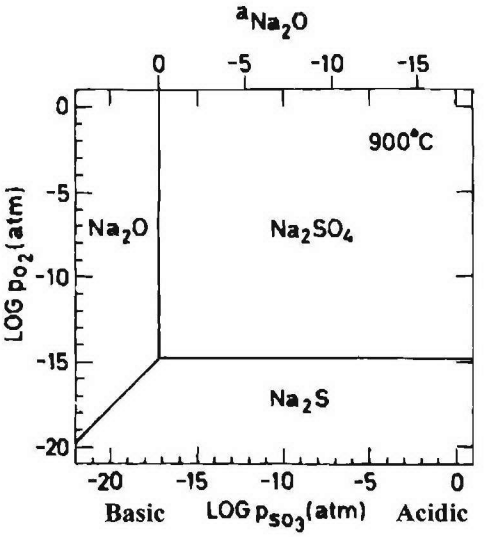

Figure 12. Phase stability diagram for Na-S-O system at 900°C [39].

These fluxing reactions are very similar to anodic and cathodic reactions in aqueous environments. Basic and acidic fluxing of an oxide can be explained by considering an example of NiO fluxing in Na_2SO_4. Gupta and Rapp [40] measured solubility of NiO in Na_2SO_4 as a function of log(a_{Na_2O}) (or log P_{SO_3}) and their results are shown in figure 13. The solubility of NiO has a minimum at log a_{Na_2O} = -10.3 and it increases with increase in log(a_{Na_2O}) (*i.e.* decrease in log P_{SO_3}) according to the reaction,

$$2NiO + O^{2-} + \tfrac{1}{2}O_2 = 2NiO_2^- \qquad (9)$$

The above reaction corresponds to the basic fluxing of NiO in Na_2SO_4. The solubility of NiO also increases below the minimum with decrease in $\log(a_{Na_2O})$ (*i.e.* increase in log P_{SO_3}) according to the reaction,

$$NiO = Ni^{2+} + O^{2-} \quad (10)$$

This corresponds to the acidic fluxing of NiO, suggesting that at higher values of $\log(a_{Na_2O})$, NiO dissolves as NiO_2^- and at lower values as Ni^{2+}.

2.3.5 Basic and Acidic Fluxing Model

The concept of fluxing of an oxide is used to interpret various propagation modes in hot corrosion. Researchers have developed fluxing models for each type of fluxing mechanism. The next section discusses fluxing mechanisms and models for various hot corrosion conditions.

2.3.5.1 Goebel-Pettit Model for Basic Fluxing

Bornstein and DeCrescente [41-43] first proposed the concept of basic fluxing. Goebel *et al.* [44, 45] subsequently developed and described the model by a thermochemical approach. This model considers that metal is covered by an oxide scale which is continuously dissolved in the molten deposit. It is also assumed that a compositional gradient is established across the deposit layer. The basic fluxing model is explained here using an example of Na_2SO_4 induced hot corrosion in Ni at 900°C. In basic fluxing, oxide ions are produced in the Na_2SO_4 layer due to the removal of oxygen and sulfur from the deposit via reaction with the alloy or metal as shown in equation 11 below,

$$SO_4^{2-} = SO_3 + O^{2-} = \tfrac{1}{2}S_2 + \tfrac{3}{2}O_2 + O^{2-} \quad (11)$$

It should be noted from this equation that an increase in O_2 or O^{2-} activity necessarily means a decrease in sulfur activity and vice versa. From estimated oxygen and sulfur activities in a gas turbine environment, the phase stability diagram suggests that NiO is predominantly formed resulting in depletion of oxygen near the Na_2SO_4/NiO interface. An oxygen activity gradient is produced by initial oxidation of Ni throughout the Na_2SO_4

layer. Decrease in oxygen activity at the Na_2SO_4/NiO interface results in a higher sulfur activity beneath the NiO layer. An increased sulfur activity promotes formation of nickel sulfide, which decreases sulfur activity and eventually increases oxide ion activity. Higher oxide ion activity would then favor fluxing or dissolution of NiO by oxide ions via reaction 9.

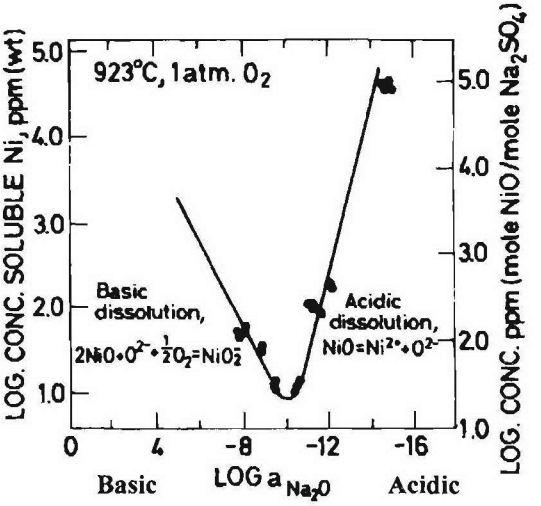

Figure 13. The solubility of NiO in Na_2SO_4 at 1atm O_2 and 927°C as a function of basicity a_{Na2O} in Na_2SO_4 [40]

The hot corrosion conditions create a gradient of O^{2-} and O_2 activity such that O^{2-} activity decreases and O_2 activity increases when going from the Na_2SO_4/NiO interface through the Na_2SO_4/gas interface. Nickelate ions formed from the above reactions then diffuse away from Na_2SO_4/NiO interface to a point where the O^{2-} activity is low and O_2 activity is high. This leads to the precipitation of NiO_2^- to NiO resulting in a discontinuous, non protective and porous oxide scale increasing the mobility of liquid Na_2SO_4 through the scale. Basic fluxing explained using this model is maintained until Na_2SO_4 is consumed. The fluxing model proposed by Goebel and Pettit [44] for hot corrosion of Ni is shown in figure 14. Such a basic fluxing mechanism has distinctive microstructural features of porous, non-protective oxide scale and sulphide particles are found in the alloy substrate below the oxide scale. This form of basic fluxing depends on the production of oxide ions from the molten deposit; hence, a continuous supply of molten deposit is required for the attack to continue. This suggests that basic fluxing hot

corrosion is not self-sustaining and is usually restricted to high temperatures (Type I ~ 900°C).

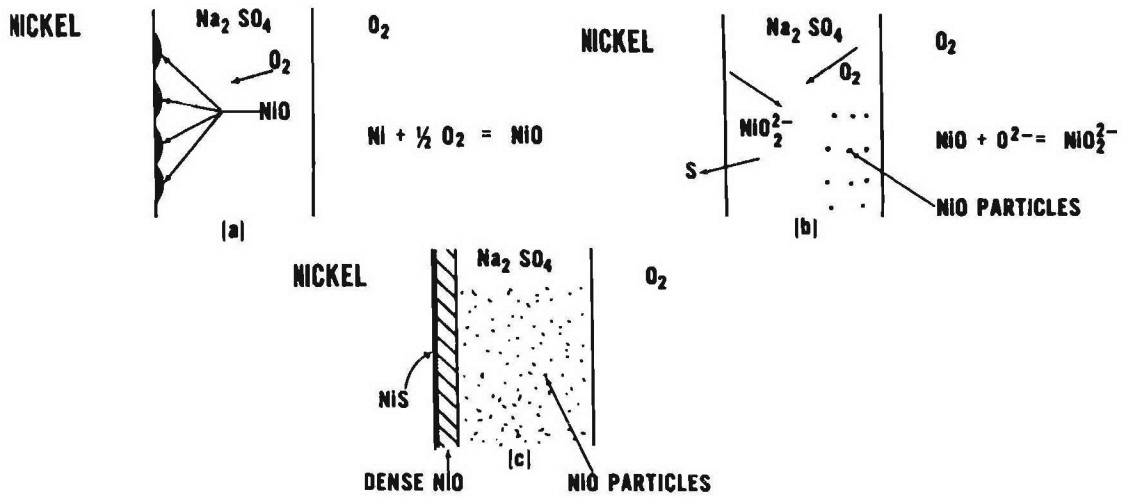

Figure 14. Model for Na_2SO_4-induced accelerated oxidation of pure nickel. (a) Oxygen activity gradient is produced by initial oxidation of nickel. (b) Sulfur enters alloy and oxygen ions react with NiO to form nickelate ions. (c) Sulfur activity decreases and oxide ions are no longer produced, Na_2SO_4 becomes saturated with Ni, and a continuous NiO scale is formed [44].

2.3.5.2 Rapp-Goto Criterion of Oxide Fluxing

Rapp and Goto [46] considered a fluxing model based on oxide solubilities in the molten deposit. According to these authors, hot corrosion attack is sustained through a dissolution-precipitation mechanism if "negative solubility gradient" of the protective oxide is maintained at some distance from oxide/salt to salt/gas interface. Using this Rapp-Goto model, Shores [47] provided the following quantitative expression for the earlier Goebel-Pettit model of dissolution-precipitation mechanism;

$$\left[\frac{d\,[\text{Solubility of oxide}]}{dx} \right]_{x=0} < 0$$

Here x = 0 is the salt/oxide boundary and x > 0 corresponds to the salt layer. This so-called Rapp-Goto criterion does not involve consumption of sulfur or any change of molten deposit with time and is applicable to both acidic and basic fluxing. The negative

solubility gradient of an oxide is a consequence of the negative gradient of O^{2-} or $S_2O_7^{2-}$ in the melt. Rapp [48] considered two specific conditions to explain the acidic and basic fluxing using the Rapp-Goto criterion. In basic fluxing, basic solute (*e.g.*, O^{2-}) has a higher solubility at the oxide/salt interface than at the salt/gas interface resulting in higher solubility for oxide at the oxide/salt interface than at the salt/gas interface. The concentration gradients produced are also shown in the figure 15. It should be noted that due to oxidation of Ni, oxygen is consumed and P_{O_2} decreases at the oxide/salt interface but basic fluxing occurs if the solubility of an oxide is higher at oxide/salt interface.

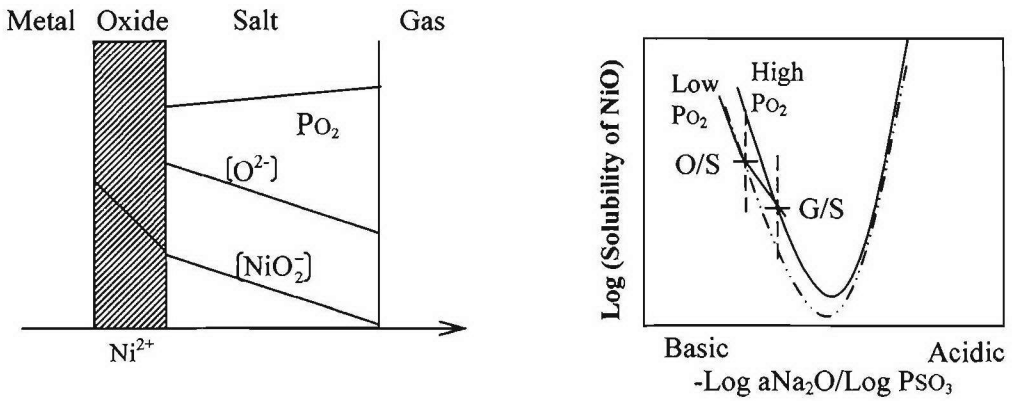

Figure 15. A schematic diagram of concentration gradients applying Rapp-Goto criterion of basic fluxing with O^{2-} as oxidant. For the establishment of "negative solubility gradient" in basic fluxing, solubility of oxide in the melt should be higher at O/S interface than G/S interface.

For acidic fluxing, $S_2O_7^{2-}$ is formed from the following reaction,

$$2SO_4^{2-} = S_2O_7^{2-} + O^{2-} \quad (12)$$

The dominant acidic solute (*e.g.*, $S_2O_7^{2-}$) has a higher solubility at the oxide/salt interface than at salt/gas interface (figure 16). For a constant P_{O_2} acidic fluxing is sustained if solubility of an oxide is higher at oxide/salt interface than at gas/salt interface *i.e.*, if a negative solubility gradient is maintained. Rapp [48] determined and compiled solubilities of various oxides as a function of melt basicity and oxygen activity for pure fused Na_2SO_4 at 1200 K and at 973 K for SiO_2 (figure 17). In the range of this study SiO_2

does not form an ionic solute, and its low solubility is independent of basicity or acidity. According to Rapp [48], under the operating conditions of a gas turbine, the P_{SO_3} values produced are in the range where both Cr_2O_3 and Al_2O_3 exhibit minimum in their solubilities.

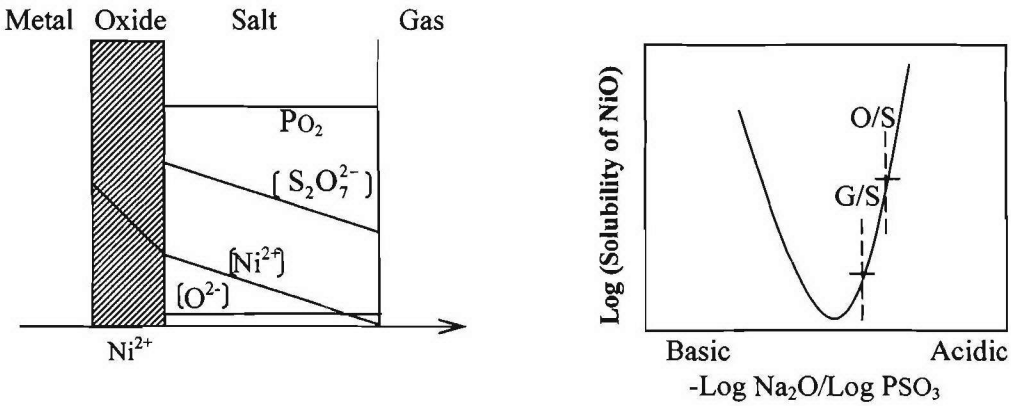

Figure 16. A schematic diagram of concentration gradients applying Rapp-Goto criterion of acidic fluxing $S_2O_7^{2-}$ with as oxidant. For the establishment of "negative solubility gradient" in basic fluxing, solubility of oxide in the melt should be higher at O/S interface than G/S interface.

Shores [47] examined the Rapp-Goto criterion for different conditions and confirmed that the reactions are not always self-sustaining. For example, Shores showed that basic fluxing is not self-sustaining and molten deposit becomes more basic over a period of time. Hot corrosion attack eventually stops unless more salt is deposited. This condition is shown in figure 18. Shores [47] considered various possibilities and determined when fluxing would occur. Luthra [49-52] used the Rapp-Goto criterion and developed a model for hot corrosion in Type II conditions.

Stringer [38] concluded that fluxing by Na_2SO_4 is not likely to be important in a gas turbine due to following reasons:

1. The salt deposits in gas turbine are very thin and gradients of basic and acidic solute (O^{2-} or $S_2O_7^{2-}$) can not be expected.
2. Acidic fluxing will not occur because of low P_{SO_3} available at high temperatures creating positive or zero solubility gradient. However, Shores [47] showed that the Rapp-Goto criterion for acidic fluxing is satisfied in the presence of strong acidic refractory metal oxides at higher temperatures.

3. Oxides such as NiO have minimum solubility at $a_{Na_2O} = 10^{-10}$ atm and basic fluxing of NiO occurs at $a_{Na_2O} > 10^{-10}$ atm. Basic fluxing of NiO is not possible in gas turbine atmosphere because salt deposit is too acidic (*i.e.* $a_{Na_2O} < 10^{-10}$ atm), suggesting that acidic solute should be dominant in creating a positive solubility gradient. To address this valid question Otsuka and Rapp [53] conducted a potentiometric experiment to track basicity and the oxygen activity at the substrate/salt interface during hot corrosion of Ni. They found that initially an acidic solute was dominant but after some time salt film was reduced and deposit became less acidic. Nickel sulfides were formed and the coupon was severely corroded while at the same time local salt chemistry shifted towards higher basicity. Their findings suggest that even in acidic gas turbine environment basic fluxing of NiO is possible thus satisfying negative solubility gradient criterion.

As mentioned earlier the Rapp-Goto criterion can be applied to both basic as well as acidic fluxing. This led researchers to develop separate models for acidic fluxing reactions. Acidic fluxing of alloys in a gas turbine engine environment occurs by at least two different processes. One of which is known as "gas phase induced acidic fluxing" where the component that produces acidic conditions can be present in the surrounding gas. Another possibility is that the acidic component can be present as an oxide of an element in the alloy and this type of fluxing is known as "alloy phase induced acidic fluxing". The models describing these two processes will be discussed in the next section.

2.3.5.3 Gas Phase Induced Acidic Fluxing

In this type of acidic fluxing, component is supplied to the salt deposit from the surrounding gas. Typically, in gas turbine engine environment there are two types of acidic components, SO_3 and V_2O_5. As discussed earlier, SO_3 is produced due to the combustion of sulfur in the fuel, while V_2O_5 can be present as an impurity in the fuel.

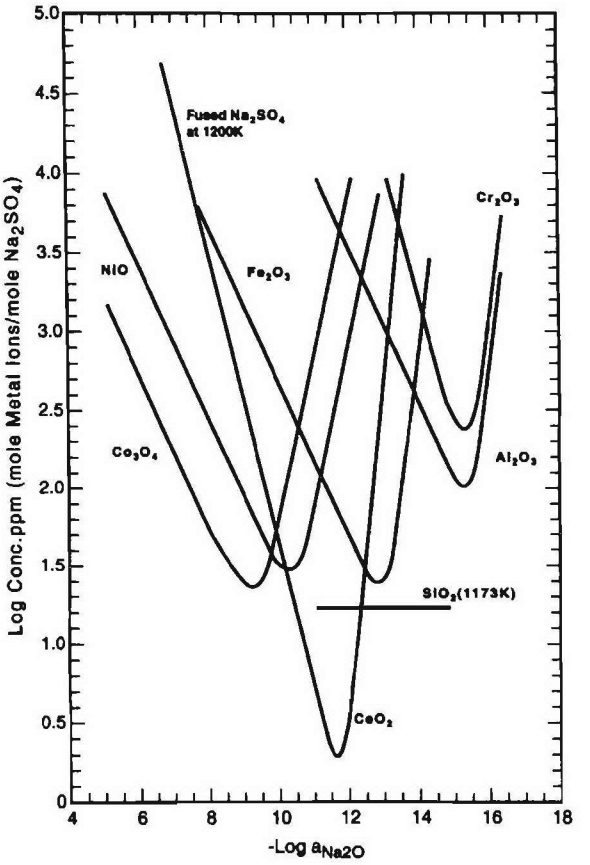

Figure 17. Measured solubilities for several oxides in pure fused Na_2SO_4 [48].

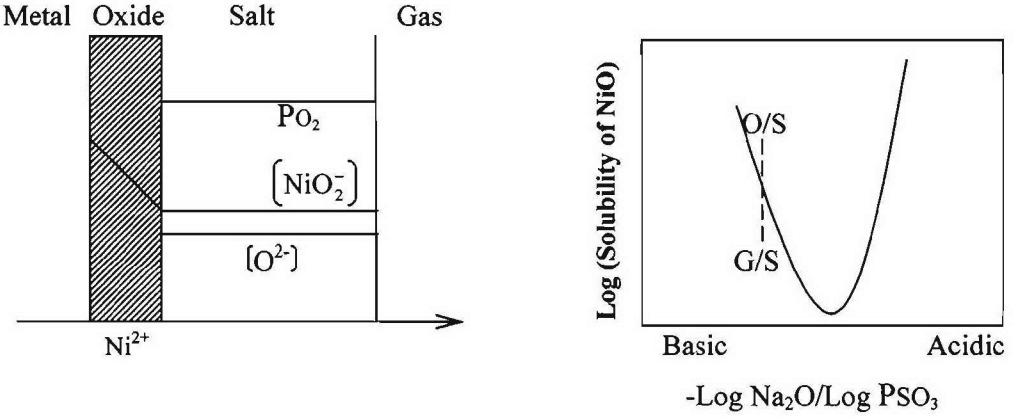

Figure 18. A schematic diagram of concentration gradients with no O^{2-} gradient because of fast transport. A condition for "negative solubility gradient" of oxide is not satisfied hence fluxing does not occur.

SO_3-gas phase induced attack is the focus of this current proposed research. In case of SO_3-gas phase induced attack, SO_3 may react with Na_2SO_4 in the following manner to produce lower melting temperature products such as sodium pyrosulfate (T_{melt} = 401°C),

$$Na_2SO_4 + SO_3 = Na_2S_2O_7 \quad (13)$$

However, liquid formation of the deposit in SO_3-gas phase induced attack is not likely due to sodium pyrosulfate formation, but is instead due to the formation of eutectic Na_2SO_4-MSO_4 (where M is Ni or Co) liquid.

SO_3-gas phase induced acidic fluxing goes through a maximum at 700°C. As discussed in the earlier section, Type II hot corrosion or gas-phase induced acidic fluxing depends upon the partial pressure of SO_3 which decreases with increase in temperature. Therefore, SO_3-gas phase induced hot corrosion rate decreases considerably above 800°C and at 900°C Type I or basic fluxing conditions are favored. Since quite high P_{SO_3} is available at the oxide/salt interface, the reaction between oxide (*i.e.* NiO or CoO) and SO_3 is much faster and more stable than the reaction between SO_3 and Na_2SO_4. This mode of attack gives Type II hot corrosion. There are various models developed to explain SO_3-gas phase induced attack. Luthra *et al.* [49-52], proposed that non-protective Al_2O_3 and Cr_2O_3 oxide scales are formed in presence of salt deposit due to rapid removal of nickel and/or cobalt from the alloy. Nickel and cobalt diffuse outward to react with the deposit not allowing the formation of protective and continuous Al_2O_3 and Cr_2O_3. These oxides of nickel and/or cobalt then become soluble in the acidic melt at the salt/oxide interface.

SO_3-gas phase induced acidic fluxing mechanisms of the Ni- and Co-based alloys are quite similar to the mechanisms explained for pure Ni [39, 54] and Co [55, 56]. The hot corrosion product in Ni- and Co-based alloys also consists of two layers: (i) Eutectic liquid layer of Na_2SO_4+ MSO_4 (where M is Ni or Co) as an outer layer and (ii) inner layer of Ni_3S_2 + NiO in Ni-based alloys or only CoO/Co_3O_4 in case of Co-based alloys. The pits or internal attack usually consist of sulfate mixture, Cr_2O_3 and/or Al_2O_3. The pitting type of attack is because breakdown of protective Cr_2O_3 or Al_2O_3 scales followed by fluxing of NiO or CoO and their spinels. The sulfate formation of NiO and CoO and even Ni/Co components of spinels above critical SO_3 pressures causes gas phase induced

acidic fluxing in these alloys. Ni-S formed during the corrosion may partially react with Cr to form more stable Cr_2S_3. The outward diffusion of Ni through NiO + Ni-S layer is much faster than the outward diffusion of Co through CoO/Co_3O_4 layer. However, Co-based alloys are more susceptible to Type II hot corrosion than Ni-based alloys. The main reason for this is that $CoSO_4$ is more stable than $NiSO_4$ with respect to CoO and NiO, respectively. As a consequence, $CoSO_4$ can form at a lower P_{SO_3} than $NiSO_4$. In addition, the eutectic mixture of $Na_2SO_4 + CoSO_4$ has a much lower melting temperature (565°C) than that of $Na_2SO_4 + NiSO_4$ (T_{melt} = 671°C); hence the Co-based alloys are likely to be more susceptible to Type II attack than the Ni-based alloys at lower temperatures. Luthra and Shores [57] also showed that CoO is a better catalyst for the $SO_2 + ½\ O_2 \rightarrow SO_3$ reactions than NiO as this increases P_{SO_3} at the CoO surface than at the NiO surface.

Barkalow and Pettit [58] proposed another model for gas-phase induced acidic fluxing suggesting that the P_{O_2} at the oxide/salt interface is too low to form oxides of cobalt and nickel and SO_3^{2-} ions are formed from the following reaction,

$$SO_4^{2-} = SO_3^{2-} + ½\,O_2 \quad (15)$$

Al_2O_3 is assumed not to be stable in such melts because of the following reaction,

$$3SO_2 + Al_2O_3 \rightarrow 2Al^{3+} + 3SO_3^{2-} \quad (16)$$

A dissolution-precipitation mechanism is followed so that non protective oxide particles are formed at the salt/gas interface where P_{O_2} is higher. This model does not assume that the salt deposit will be in liquid form at the low SO_3 pressures.

2.3.5.4 Alloy Phase Induced Acidic Fluxing

Acidic conditions in the salt deposit are also favored by the incorporation of certain oxides such as MoO_3 [45] and WO_3 [59]. These oxides dissolve in the melt in following manner,

$$MoO_3 + Na_2SO_4 \rightarrow Na_2MoO_4 + SO_3 \quad (17)$$

$$WO_3 + Na_2SO_4 \rightarrow Na_2WO_4 + SO_3 \quad (18)$$

Thermally grown oxides (NiO, CoO, Al_2O_3 and Cr_2O_3) can dissolve into the melt at regions with higher $MoO_3/WO_3/V_2O_5$ activity and precipitates where activity of these oxides is low. During initial formation of Na_2MoO_4/Na_2WO_4 and its dissolution in

deposit, an increase in local concentration of PSO_3 causes rapid sulfate-induced corrosion of an alloy. Alloy-induced acidic fluxing occurs till Mo, W or V component of the alloy is completely consumed suggesting that alloy induced fluxing is self-sustaining and only one application of salt layer may cause complete destruction of alloy. This type of acidic fluxing occurs at high temperatures where refractory metal oxides are more stable providing sufficient amount of oxides for making the melt acidic.

2.3.6 Hot Corrosion Degradation Sequence

Hot corrosion rate of an alloy changes with time. Pettit and Meier [2, 60] proposed that hot corrosion follows two stages of degradation, an initiation followed by a propagation stage. A schematic representation of hot corrosion degradation sequence is shown in figure 19. Pettit and Giggins [61] using weight-change kinetics and microstructural analysis showed that hot corrosion underwent a marked change with increase in severity. Hot corrosion resistance for an alloy is often provided by a protective reaction product formation. Initiation stage is slow and involves formation of an oxide scale which would have been formed in the absence of salt deposit; while propagation mode is more catastrophic and involves fluxing or complete breakdown of an oxide barrier. Hot corrosion resistance depends on the extent of protection provided by the protective reaction product thereby prolonging initiation stage and by inhibiting propagation stage. Hot corrosion degradation sequence proceeds by replacing the protective product with a less protective reaction product.

2.3.6.1 Initiation Stage of Hot Corrosion

An alloy forms various oxides during initiation stage and a competition exists for the formation of continuous oxide layer. Under equilibrium conditions, the most stable and slow growing oxide scale is established at the oxide/metal interface. In a gas turbine engine application most alloys form Al_2O_3 and/or Cr_2O_3 as a protective TGO scale. Consequently, an established protective reaction product offers resistance to the growth of various fast growing external oxides and to the salt penetration. It avoids direct contact between the alloy surface and the salt deposit thereby delaying initiation stage. The composition of a protective layer depends on the chemical composition of the alloy itself.

The initiation stage begins in a very similar to the transient oxidation without salt deposit and is also quite similar for both Type I and Type II hot corrosion. As the initiation stage progresses, salt deposit begins to affect the reaction product beneath the salt deposit. Initiation stage is evident when some time is lapsed before deposit can form a non-protective reaction product. In Type I hot corrosion Cr and Al are sufficiently depleted below subsurface level thus allowing oxide scale to be penetrated. The breakdown of protective scale is often associated with the transport of secondary oxidant through the scale.

The mechanisms by which secondary oxidant penetrates the oxide scale is not clear. The secondary oxidants could penetrate through pores and cracks present in the oxide scale. Singh and Birks [62] have shown that lattice diffusion could not establish a sufficient sulfur activity to form sulfides below TGO scales. However, Kim *et al.* [63, 64] observed sulfur penetrating through the oxide grain boundaries in pre-existing Cr_2O_3 and Al_2O_3 scales with no evidence of cracks and pores in the scale. The breakdown of Cr_2O_3 and Al_2O_3 is possible in high sulfur pressure atmospheres due to developments of sulfide channels through the scales [65, 66]. The initiation stage ends when salt or sulfur penetrates protective scale by forming sulfide particles beneath the scale. This stage is usually more evident for Type I than Type II hot corrosion. In Type II conditions the initiation stage continues by the reaction between external Ni or Co oxides and the solid Na_2SO_4 forming eutectic $Na_2SO_4 + MSO_4$ (where M is Ni or Co) liquid. This reaction is faster in Co-based alloys leading to smaller initiation time compared to Ni-based alloys. It is also possible that the initiation stage may not visibly exist in some alloys with poor hot corrosion resistance. Consequently, degradation directly goes into the propagation stage when molten deposit comes in contact with such alloys. Alloys which are unable to develop a continuous and protective layer of Cr_2O_3 or Al_2O_3 in the presence of a salt deposit have poor hot corrosion resistance. The duration over which the scale provides protection against hot corrosion is influenced by a number of factors listed below [2, 60, 61]:

1. Alloy composition
2. TGO-reaction product composition and thickness
3. Alloy processing
4. Gas composition

5. Salt composition and its physical state
6. Salt deposition flux
7. Temperature
8. Thermal cycles
9. Erosion
10. Specimen geometry
11. Thickness of the salt scale
12. Pre-oxidation treatment

2.3.6.2 Propagation Stage of Hot Corrosion

Hot corrosion rates are much larger in the propagation stage and the alloy must be replaced from service at this stage. Various types of propagation modes are evident through the microstructural features. The propagation stage proceeds when reactants from the gas diffuse through the deposit or elements from alloy dissolve and diffuse out at the salt/gas interface [2, 60, 61]. Diffusion of reactants through the deposit often changes composition and such changes play an important role in various types of propagation modes [60]. A reaction between deposit and metal/oxide forms a non protective reaction product during propagation mode. Non-protective reaction product formation is often due to fluxing of an oxide in the molten salt. Fluxing mechanisms have already been discussed in the previous sections.

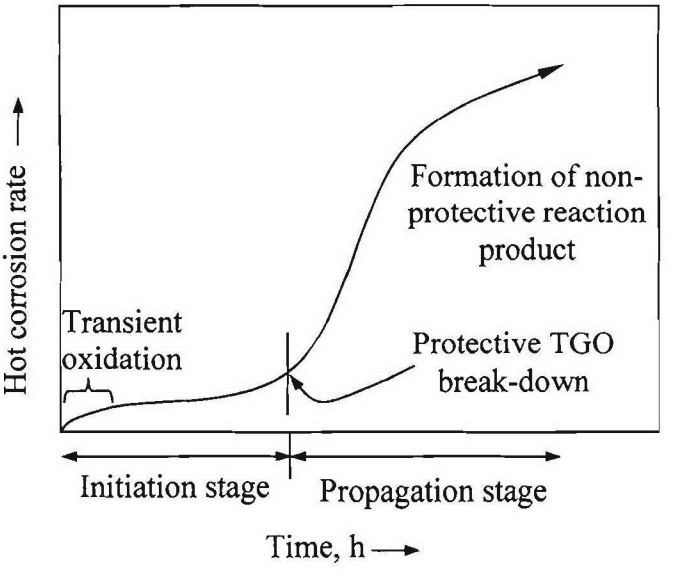

Figure 19. A schematic representation of hot corrosion degradation sequence.

2.3.7 Hot Corrosion of Pt-modified Alloys/Coatings and MCrAlY-Based Coatings

The hot corrosion resistance of coatings often depends on chemical composition, microstructure, and deposition method. Hot corrosion resistance of aluminide coatings is improved by the addition of modifying elements like Pt [67, 68], Cr [69, 70] and Si [72]. Platinum addition has been found to improve Type I hot corrosion and oxidation resistance of β-NiAl coatings [67, 68, 72, 73]. Indeed, addition of Pt tends to reduce surface spallation by promoting the slow growth of extremely adherent α-Al_2O_3 scale [68]. Haynes *et al.* [74] and Zhang *et al.* [75] found that, along with improved scale adhesion, Pt also helped in decreasing detrimental effects of high S levels in the substrate and reducing the amount of voids at the scale/metal interface. The hot corrosion resistance of Pt-modified β-NiAl coating depends upon the substrate and their behavior has been studied on various substrates by researchers over the past 30 years. Addition of Cr has been shown to improve hot corrosion resistance of aluminide coatings at both low and high temperatures [69, 70]. In addition, Cr can be beneficial by decreasing the amount of Al in the alloy required to form a protective Al_2O_3 scale layer [17]. Malush *et al.* [76, 77] and Dust *et al.* [78] found that Cr+Pt modified aluminide coatings exhibited excellent hot corrosion resistance. The MCrAlY overlay coatings have optimum composition and have excellent hot corrosion resistance. The CoCrAlY-based coating is known to have relatively good resistance to high-temperature Type I hot corrosion; however, their low-temperature Type II hot corrosion depends upon the Cr content [52]. Luthra [52, 79] showed that Cr-rich CoCrAlY coatings have better Type II hot corrosion resistance than conventional CoCrAlY coatings. The NiCrAlY and NiCoCrAlY are other types overlay coatings often used in gas-turbine engines and hot corrosion resistance of these coating was previously studied by the number of researchers [81, 82]. Hot corrosion resistance of various commercial and developmental coatings will be studied and compared in this thesis.

2.4 Oxidation Behavior of Pt-Modified Ni-Based Alloys and Coatings: Brief Overview

The effect of alloying addition on the oxidation behavior of Ni-Al system relevant to this proposal will be discussed in detail in this section. Aluminide coatings are used to improve high-temperature oxidation resistance of Ni-based and Co-based superalloys by forming thermally grown protective oxide scale. The addition of platinum group metals (PGM) such as Pd [21], Ir [22] and most commonly Pt [23, 24, 72, 73] to β-NiAl promotes the formation of thin, continuous, and adherent α-Al_2O_3 scale. Although Pt has been known to improve oxidation performance of β-NiAl diffusion-aluminide coatings the exact mechanisms by which it helps are unclear. Jackson *et al.* [82] and Schaeffer *et al.* [83] found Pt-enrichment at the surface of the alloy and proposed that Pt retarded the diffusion of refractory elements from the substrate. Recently, Cadoret *et al.* [84, 85] reported increased growth rate of an oxide scale with Pt addition during the initial stages of oxidation of β-NiAl alloys. It was found that transition from θ-Al_2O_3 to α-Al_2O_3 was delayed in the presence of Pt leading to thickening of an oxide scale before the transformation. The researchers proposed that prolonged transition favored the relaxation of stresses and slow growth of alumina scale during the transient oxidation. This is attributed to the increase in the Al diffusion in the alloy, thus promoting the oxide growth and limiting the formation of interfacial cavities. In fact, Gleeson *et al.* [1] recently showed using the ternary diffusion couples that the interdiffusion coefficient for Al in its own concentration gradient D_{AlAl} increases with increasing Pt content. Both the groups found that Pt improved the alumina scale adherence in β-NiAl and $\gamma+\gamma'$ alloys.

The beneficial effect of Pt in $\gamma+\gamma'$ was studied in detail and ascribed that Pt is non-reactive and decreases the chemical activity of aluminum [1]. Pt partitions solely to Ni sites in ordered $L1_2$ crystal structure of γ' thereby increasing the Al:Ni atom fraction. The Al enrichment at the surface kinetically favors the alumina formation. The short-term oxidation studies by Hayashi *et al.* [86] further showed that Pt-containing γ'-based alloys show subsurface Pt-enrichment thus promoting alumina formation. The beneficial effect of Pt was also seen at lower temperatures around 700°C and 900°C and during transient oxidation [86].

Other ternary alloying additions such as Si and Ti additions promote alumina scale formation in NiCrAlY-based coatings [87]. The beneficial effect of Si on the cyclic

oxidation behavior of aluminide coatings was also observed by other researchers [88]. The amount of critical concentration required to form a protective scale in binary alloys can be decreased by additions of elements that form oxide of intermediate thermodynamic stability to the oxides of the elements present in the binary alloy. For instance, it is well known that with additions of Cr in M-Al (where M =Ni, Co or Fe) alloys lower amount of Al is needed to establish and maintain an alumina scale. This phenomenon is known as third element effect or gettering effect [17]. Brumm and Grabke [89] also showed that Cr_2O_3 formed during initial stages of oxidation acts as nuclei for the formation of α-Al_2O_3. However, the addition of Cr to NiAl is reported to accelerate θ-Al_2O_3 to α-Al_2O_3 phase transformation and leads to higher k_p values [89]. Pint et al. [90] observed that Cr additions up to 10at% in Hf containing NiAl alloys resulted in the faster scale growth as well as scale spallation. Phillips and Gleeson [91] also showed that higher Cr additions were detrimental for the oxidation resistance of NiAl alloys. Unfortunately, higher Cr additions are quite beneficial for improving hot corrosion resistance which led the researchers to conclude that high-temperature oxidation and hot corrosion resistance are not possible to achieve at least in β-NiAl [92].

It is generally known that segregation of sulfur impurities at the oxide/alloy interface significantly decreases the oxide adherence [93, 94]. It has been also observed that detrimental effects of S can be reduced by addition of Pt or by the additions of reactive elements such as Zr, Y, and Hf [18]. Pint *et al.* [19, 20] reported that the addition of 0.05at% Hf to β-NiAl results in slowest-growing and most adherent alumina scale observed in β-NiAl and proposed that Pt additions in the β-NiAl may be unnecessary with the correct amount of reactive element-Hf additions.

The oxidation behavior of β-NiAl aluminide coatings can be influenced by various factors. Al present in the coating diffuses from the coating into the substrate and also diffuses out to maintain Al_2O_3 scale effectively depleting Al in the coating. A recent study by Pint [95] showed the beneficial effect of Pt and Hf for various levels Al in Ni-Al system. However, lower Al (> 34.7at %) containing alloys (β+γ') without Pt addition experienced higher mass gain indicating the formation of Ni-rich oxides.

The beneficial effect of Pt in β-NiAl is very well known and the work by Coupland *et al.* [96, 97] and Tatlock et al. [98-100] showed that Pt also improves

oxidation and hot corrosion resistance of alloys with $\gamma+\gamma'$ compositions. Felten [101] studied the effect of Pt with Cr addition in low Al (12 at.%) based $\gamma+\gamma'$ alloys and showed that these alloys were indeed alumina formers. A very recent study of the Ni-Pt-Al system with Hf additions by Gleeson *et al.* [1] led to the foundation for the novel $\gamma+\gamma'$ coatings as an alternative to β-NiAl aluminide coatings. These authors showed that certain unique Ni-Al-Pt-based alloy compositions, which are sufficiently low in aluminum content (20-22 at%) to be free of β-NiAl, are excellent candidates for the development of novel coatings (and bond coats) that confer significantly improved component oxidation performance. Specifically, was been found that Pt-containing γ'-$Ni_3Al+\gamma$-Ni alloys modified with up to 2.0 wt.% Hf form highly adherent, planar, slow-growing α-Al_2O_3 scales during both isothermal and cyclic oxidation at high temperature (maximum temperature studied thus far has been 1150°C). Moreover, the presence of platinum in the alloys decreases the thermodynamic activity of aluminum to the extent that it is below the aluminum activity in common Ni-base superalloys used for aero-engine turbine applications. As a consequence, and in complete contrast to β-NiAl-containing coatings, aluminum diffuses from the substrate alloys to the novel $\gamma'+\gamma$ coating compositions. This is a significant development in that the novel coating compositions offer the combined beneficial properties of (1) forming a slow-growing, planar and adherent TGO scale of α-Al_2O_3, (2) not depleting in aluminum due to coating/substrate interdiffusion during service, and (3) being compatible with a superalloy substrate in terms of phase constitution and, hence, coefficient of thermal expansion. Figure 20 (a) compares the 1150°C cyclic oxidation kinetics of bulk alloys of the following Pt-modified alloys: β-NiAl (50 at.% Al), γ'-$Ni_3Al+\gamma$-Ni (22 at.% Al), and Hf-modified γ'-$Ni_3Al+\gamma$-Ni (22 at.% Al). It is seen that the β alloy (based on the commonly used bond coat composition) underwent weight loss, which is indicative of TGO spallation, while the better performing $\gamma'+\gamma$ alloys did not show notable evidence of scale spallation. The performance of the Pt+Hf-modified alloy is particularly superior, undergoing minimal weight gain and, therefore, an exceptionally slow rate of TGO scale thickening. The TGO scales that formed on the $\gamma'+\gamma$ alloys with and without Hf addition were found to be an adherent, continuous, compact and planar layer of α-Al_2O_3. In the

same figure 20 (b) the best performing Hf-modified β-NiAl (Ni-50Al-0.05at% Hf) data by Pint *et al.* [102] is compared. An almost similar weight gain is observed for the best performing Pt+Hf-modified γ'-Ni_3Al+γ-Ni (Ni-22Al-30Pt-1wt%Hf) and Hf-modified β-NiAl (Ni-50Al-0.05at% Hf).

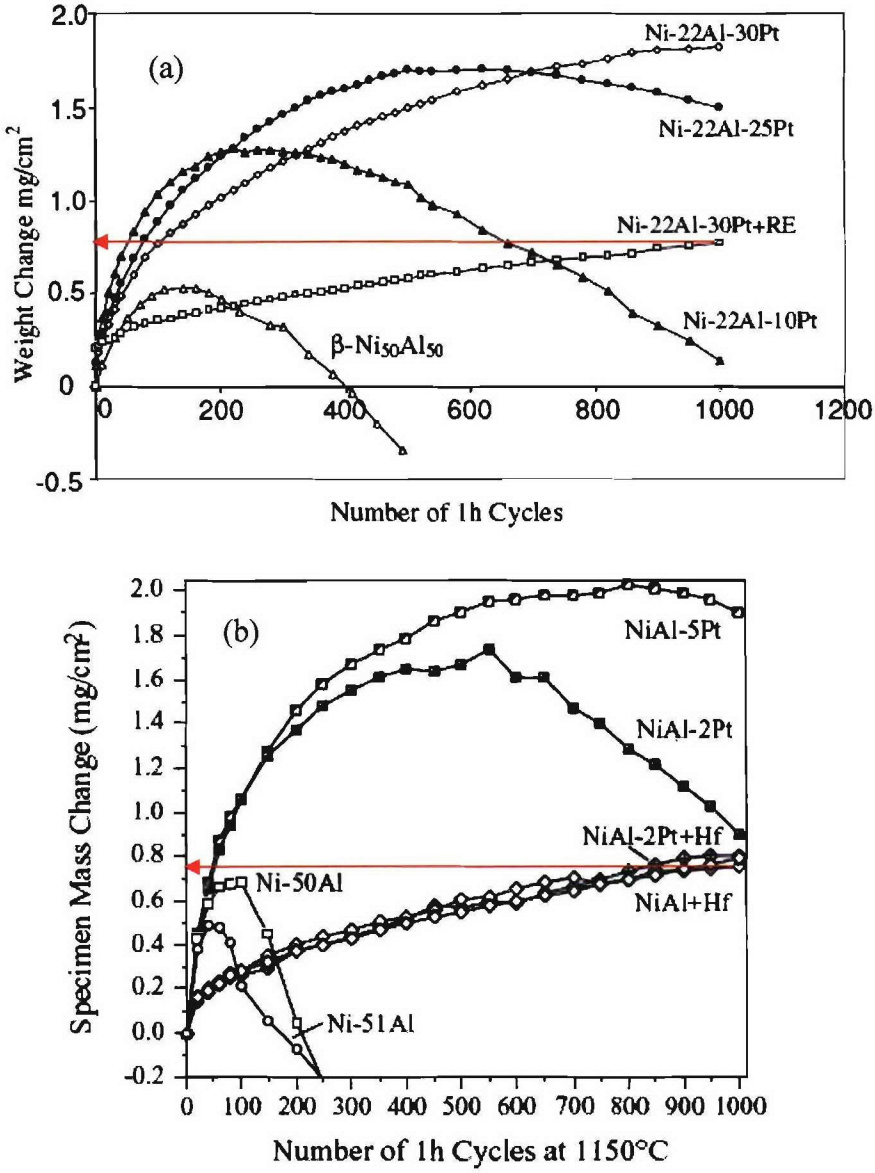

Figure 21. Comparison of cyclic oxidation behavior of (a) modified γ'-Ni_3Al+γ-Ni [1] (carried out in air) and (b) modified β-NiAl [102] (carried out in flowing O_2) both at 1150°C.

Zhang *et al.* [104] studied and compared oxidation behavior of Pt-modified γ'+γ coating with the Pt-modified β-NiAl coating and found slightly better performance within the β-NiAl(Pt) coatings; however, it was inferred that minor element variations (*e.g.* sulfur and refractory metals) exacerbated the poorer performance of the γ'+γ coatings. Hot corrosion resistance of Pt(+Hf)-modified γ'+γ coatings will be evaluated in this thesis.

2.5 Aims of Proposed Research

The primary goal of this research was to gain fundamental understanding of the hot corrosion behavior of γ'+γ coating compositions. The specific goals of the proposed research are summarized as follows:

1. To assess the hot corrosion behavior of commercially available Pt-modified β-NiAl aluminides and MCrAlY coatings on a case-by-case basis and rank their performance against both types of hot corrosion.
2. To confirm the reliability of Dean rig testing by comparing the results with the burner rig hot corrosion testing, which is often purported to better simulate the actual operating conditions in gas turbine engines.
3. The proposed study seeks to determine and even improve the hot corrosion (Type I and Type II) resistance of novel γ'+γ coating compositions that are also highly resistant to oxidation. It involves effect of alloying additions of Pt, Cr and Si on the hot corrosion and oxidation behavior γ'+γ-based alloys.
4. Finally, hot corrosion resistance of diffusion based Pt+Hf-modified γ+γ′ coating developed at ISU using pack-cementation CVD process would be tested and compared with commercially available diffusion based Pt-modified β-NiAl coating and MCrAlY coatings.

3. EXPERIMENTAL APPROACH

Hot corrosion tests were conducted on commercially used coatings and modified γ+γ′ bulk alloys and coatings. The alloys were drop-casted using Ar-arc melting. The laboratory-scale testing rig referred to as a "Dean rig" was used for hot corrosion testing. It consists of two temperature zones: a hot end where the Na_2SO_4 salt is heated above its

melting temperature and evaporates into atmosphere and a cool end where the salt condenses on the test specimens. The kinetics and extent of the salt-induced attack were monitored by measuring weight change, surface loss or extents of attack, and maximum depth of penetration as a function of time. In a separate set of oxidation tests, alloys were exposed to air under thermal-cycling conditions at 1150°C for up to 500 h. Each cycle consists of one-hour exposure at high temperature, rapid cooling to room temperature and then raising to the oxidation temperature again. Cyclic oxidation kinetics will be determined on the basis of weight change. More specific details of the tests are provided in the following section. The hot corrosion and oxidation results would be combined to down-select and guide the establishment of modified $\gamma+\gamma'$coating compositions and structures having optimum resistance to high-temperature degradation.

3.1 Materials: Alloys and Coatings

The baseline overlay CoCrAlY and diffusion aluminide coatings were applied on substrates of the MAR-M 247 (superalloy 247) and IN 792 (superalloy 792). The nominal compositions of these alloys (in wt %) are given in Table 2.

Table 2. Nominal composition (wt %) of superalloy substrates used in this study.

Alloy	Ni	Cr	Co	Ti	W	Al	Nb	Mo	C	Zr	B	Ta	Hf
Superalloy 792	60	13	9	4.2	4	3.2	2	2	0.2	0.1	0.02	-	-
Superalloy 246	59	8	10	1	10	5.5	-	0.7	0.15	-	-	3	1.5

The CoCrAlY coating was deposited via physical vapor deposition (PVD) to an actual vane airfoil made of superalloy 792. The composition of this coating was fairly uniform; however, the coating thickness varied along the length of the airfoil. Specifically, the coating on the upper portion of the airfoil was much thinner than the bottom (*i.e.*, 15 μm compared to 56 μm). The bottom-thick and upper-thin portions shall be identified CoCrAlY 1 and CoCrAlY 2, respectively.

In the case of the aluminide coatings, the superalloy 247 and 792 substrates were in the form of pins, 3.1 mm in diameter, 80 mm long and domed at one end. The Ni-rich

aluminide 1 and Ni-rich aluminide 2 coatings were standard Pt-modified β-NiAl diffusion coatings. Al-Pt-rich aluminide and Ni-rich aluminide 3 were also Pt-modified β-NiAl coatings, but deposited using a proprietary commercial process. The Ni-rich aluminide coatings 1 and 2 on superalloys 247 and 792 were both quite smoother (*i.e.*, similar in appearance to a ~ 6 μm finish) while the Al-Pt-rich aluminide and Ni-rich aluminide 3 coatings were comparatively rough (*i.e.*, similar in appearance to a 400 grit finish). The average chemical composition of each as-received coating was measured via energy dispersive spectroscopy (EDS) analysis and the results are summarized in Table 2. The measured thickness of each coating is also given in this table. The domed end of each pin was coated while 5-10 mm of the other end was uncoated. The coated portions of the pins were sectioned into ~ 12 mm pieces for hot corrosion testing. The CoCrAlY-coated vane airfoils were 30 mm long and were sectioned into 5 mm wide samples. To avoid direct exposure to the corrosive environment, uncoated ends of the pin test samples were covered with alumina cement. For the same reason, the uncoated cut sides of the CoCrAlY-coated samples were covered with alumina cement prior to testing.

Table 3. Coating composition of the tested coupons.

Alloy	**Coating**	**Measured Average Composition (at %)**
superalloy 792	Al-Pt-rich aluminide (60-65μm)	44Al-10Pt-4Cr-4Co-Bal Ni
superalloy 247	Ni-rich aluminide 1 (60-65μm)	36Al-7Pt-4Cr-6Co-Bal Ni
superalloy 792	Ni-rich aluminide 2 (60-65μm)	35Al-9Pt-6Cr-5Co-Bal Ni
superalloy 247	Ni-rich aluminide 3 (60-65μm)	37Al-7Pt-4Cr-5Co-Bal Ni
superalloy 792	CoCrAlY 1(Thick ~ 56 μm)	Co-27Cr-18Al-7Ni-0.1Y
superalloy 792	CoCrAlY 2 (Thin ~ 15 μm)	Co-27Cr-18Al-7Ni-0.1Y

In order to study hot corrosion and oxidation behaviour of γ-Ni+γ′-Ni_3Al alloys, a set of Ni-Al-Pt alloys were prepared by Ar-arc melting with appropriate proportions of high purity constituent elements. The compositions selected are indicated in the Ni-Al-Pt phase diagram [1] in figure 21. The alloys comprised a γ-Ni+γ′-Ni_3Al phase constitution

and it is seen that the aluminum content was kept constant at 22 at.%, while platinum content was varied from 0-20 at %. (Note that all compositions will be reported in atomic percent unless stated otherwise.) To improve the high temperature hot corrosion (HTHC) resistance of theses alloys, 5-20% of Cr was added. Silicon was also added in some alloys to understand its effect on hot corrosion resistance. All of the alloys contained 1wt% Hf, which helps in the formation of planar and adherent thermally grown oxide (TGO) scale. The alloys were cast into the form of rods, 50 mm long and 8 mm in diameter. The as-cast rods were heat treated in flowing argon gas at 1200°C for 6 hours followed by 48 hours at 1150°C to ensure homogenization and equilibration. The heat-treated rods were then sectioned into ~ 1.5 mm thin coupon samples and polished to a 1200-grit finish. Test samples were ultrasonically cleaned in acetone before hot corrosion and oxidation testing.

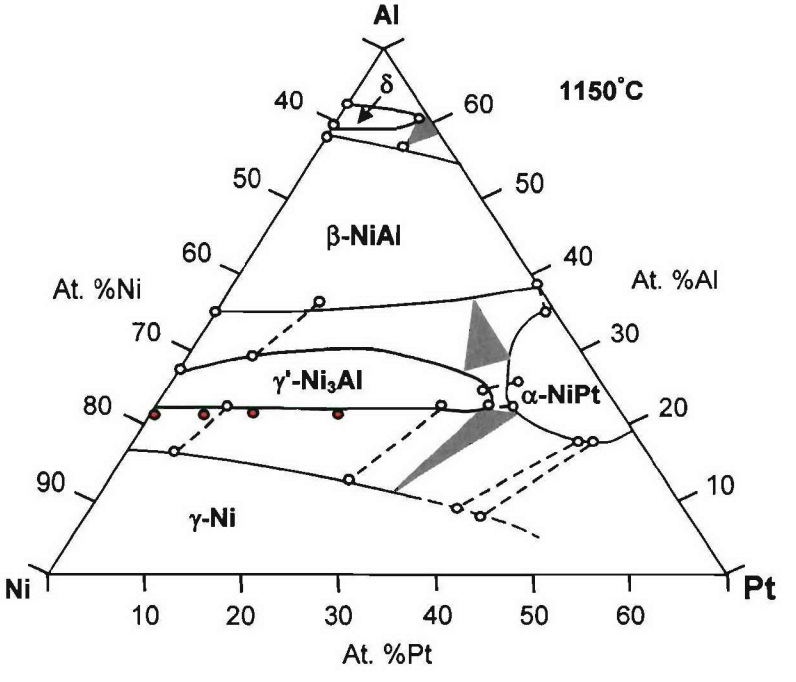

Figure 21. Ni-Al-Pt phase diagram at 1150°C and base compositions studied [1].

The hot corrosion and oxidation behaviour of Pt+Hf-modified γ'-Ni_3Al + γ-Ni coating developed at ISU was compared with commercially used γ+β-CoCrAlY and Pt-modified β-NiAl coatings. The overlay CoCrAlY and diffusion aluminide coatings were applied on

Ni-based superalloy substrates that will be designated A and B (figure 12). The nominal compositions of these alloys (in at %) are as follows:

Superalloy A: 59.6Ni-14.6Cr-8.9Co-6.9Al-5.1Ti-1.3W-1.3Nb-1.2Mo-1C-0.1B-0.06Zr

Superalloy B: 63.5Ni-13.9Al-8.2Co-8.1Cr-2.3Ta-1.6W-1.3Mo-1Re-0.07Hf

The average chemical composition (in at %) of each coating was measured via energy dispersive spectroscopy (EDS), and the results for selected constituents are summarized below:

- γ+β-CoCrAlY (65-75 μm) on superalloy A: Co-26Cr-18Al-7Ni-0.7Y-others;
- Pt-modified β-NiAl (60-65 μm) on superalloy B: Ni-45Al-7Pt-3Co-2Cr-others;
- Pt+Hf-modified γ′-Ni_3Al + γ-Ni (20-25 μm) on superalloy B: Ni-20Al-22Pt-7Co-7Cr-0.7Hf-others.

The γ+β-CoCrAlY coating was deposited via physical vapor deposition (PVD) to an actual vane airfoil made of superalloy A. The Pt-modified β-NiAl was a standard commercial diffusion aluminide coating and it was deposited on coupons of superalloy B by a process involving Pt electroplating followed by chemical vapor deposition (CVD). Similarly, the Pt+Hf-modified γ′-Ni_3Al + γ-Ni coating, with γ′-Ni_3Al being primary phase, was deposited on superalloy B by Pt electroplating followed by a proprietary Al+Hf co-deposition pack cementation CVD process. The hot corrosion experiments were carried out for 100 hours exposure on coated samples that were given a pre-oxidation treatment. The pre-oxidization treatment involved exposing the samples for 24 h at 1100°C in 3% H_2+Ar atmosphere to pre-form an Al_2O_3-rich scale.

3.2 Cyclic High Temperature (Type I) Hot Corrosion Dean-rig Testing

An alumina tray (5 x 4 cm) was used for holding the test samples. Just prior to hot-corrosion testing, the samples were placed on a hot plate or in furnace at 200°C and a saturated solution of sodium sulfate was dropped on the samples using an eyedropper. The target salt deposition was 2-3 mg/cm^2. A comparable salt deposit level has been used in many previous studies [67, 70, 76].

The Dean rig [112] for hot-corrosion testing consists of a hot zone where a salt reservoir is heated above its melting point and a cooler zone downstream where the evaporated salt condenses onto the test specimens. A carrier gas of O_2-0.1% SO_2 is passed through a platinized honeycomb catalyst to form an equilibrium amount of SO_3 which, in turn, stabilizes the salt activity. The controlled atmosphere provides conditions that are close to those found in a gas turbine. The experimental aspects of the Dean rig for HTHC testing are summarized in figure 22.

A horizontal, three-zone laboratory furnace with 4.5 cm ID alumina tube was specifically used for the Dean rig at ISU. The three temperature zones were set at 1070, 890 and 910°C to establish the hotter and cooler zones. The furnace conditions were such that the cooler and hotter zones were each about 10 cm in length. A measured thermal profile along the length of the furnace is also shown in figure 23. An alumina sample tray was kept in the cooler zone at 900°C and a 10 cm long alumina boat containing pure Na_2SO_4 was kept in the hotter zone at ~ 1040°C. The equilibrium melting temperature of sodium sulfate is 884°C, so that the salt is indeed liquid in the hotter zone. Samples were then cooled to room temperature after every 20 hours of exposure and then re-sprayed with salt at 125°C. Samples were weighed after each 20 hour cycle before salt spraying. The weight gain after corrosion also includes salt replenishment after each cycle. No attempts were made to retain any corrosion product that may have spalled during cooling to room temperature or handling. The weight of the salt crucible was measured after each 20 hour cycle and it was found that ~ 0.025 g of salt vaporized during each 20 hour cycle. Experiments were also carried out to determine the amount of salt that condensed on the samples in the 900°C zone, but the weight change was too small to be of any significance, *i.e.*, <0.1 mg/cm^2 after five 20-hour cycles. The HTHC experiments were carried out for 100 hours of total exposure. An additional set of HTHC tests were conducted in which all the specimens were pre-oxidized in a box furnace at 1100°C for 80 hours and then furnace cooled to room temperature. These pre-oxidized specimens were also tested for HTHC resistance.

3.3 Cyclic Low Temperature (Type II) Hot Corrosion Dean-rig Testing

The same experimental procedures were followed for LTHC testing, with the settings of the three furnace zones now giving a 10 cm long hotter zone and a 5 cm long cooler zone. The hotter zone was above 900°C (so that the sodium sulfate was molten) and the cooler zone was at 705°C. The 5 cm cooler zone for LTHC testing could only accommodate one alumina sample tray. The sample positions were also changed for LTHC in comparison to the positions for HTHC. The measured thermal profile along the furnace length for LTHC was similar in shape to the one shown for HTHC testing (figure 36). An additional set of LTHC tests were conducted in which the coated specimens were pre-oxidized in air at 1050°C for 1 hour. Thus, LTHC experiments were carried out for 100 and 200 hours exposure on specimens that were with and without a pre-oxidation treatment.

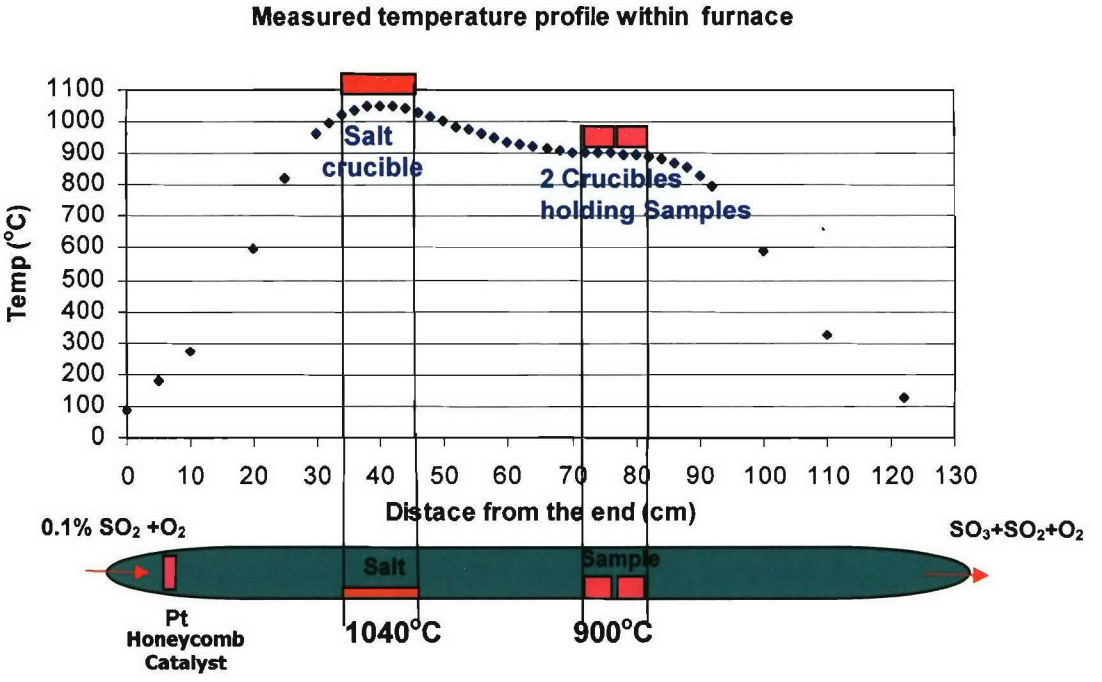

Figure 22. Temperature profile and positions of salt and sample crucibles for HTHC in the three-zone furnace. The three zones were set at 1070, 890 and 910°C.

3.4 Isothermal and Cyclic Oxidation Testing

Isothermal oxidation tests were carried out at 1100°C in still air for 80 hours using a horizontal furnace. Some other alloys were isothermally oxidized at 1150°C for 100 hours. All test samples were air-cooled to room temperature at the completion of testing. Cyclic oxidation tests were carried out at 1150°C in still air using vertical furnace. Each cycle consisted of one hour at 1150°C followed by 30 minutes at ~75°C. Sample weight change was measured using an analytical balance after every 2 cycles for the first 20 cycles and then intermittently thereafter. No attempt was made to retain any scale that may have spalled during cooling to room temperature or handling. As a consequence, weight loss kinetics were observed in some cases.

3.5 Characterization and Analysis

Digital macro images of the test samples were taken after each 20-hour cycle of hot corrosion and oxidation. After the completion of a requisite number of 20-hour cycles, the corroded and oxidized specimens were sectioned, mounted, and prepared for microscopic examination using standard metallographic techniques. Use of water or water-based products was avoided for the hot-corroded test specimens during sectioning and sample preparation procedures in order to avoid affecting the corrosion product or the salt build-up on the surface. XRD, SEM and EDS were used for characterizing the corroded and oxidized samples. An electron probe micro-analyzer (EPMA) with wavelength dispersive spectrometry (WDS) was also used for analyzing alloy and corrosion/oxidation product phases.

Each corroded pin sample was sectioned at two positions for characterization of the hot corrosion attack. One section was taken 4-5 mm from the bottom and the other 3-4 mm from the top of a given sample. A Hitachi S-2460N VP SEM/EDS was used in the back-scattered electron (BSE) imaging mode for the characterization and analysis. All images were taken at 20 keV. Both the extent of attack and the maximum depth of penetration were measured from SEM images. The extents of attack were categorized as follows: if depth of penetration over a given length (*i.e.*, arc) of the coating/substrate was between 0-25 μm it was designated as low corrosion; if it was between 25-60 μm it was medium corrosion; and if it was more than 60 μm it was high corrosion. The three

different extents of attack are summarized schematically in figure 23. After defining arc lengths for the different extents of attack, the arc angles from the centre of the image were determined. These angles were then added for low, medium and high extents of corrosion. The same procedure was conducted for both cross-sections and an average was taken for each extent of attack to arrive at a percentage. The maximum depth of penetration into the coating/substrate was also recorded from any of the two cross-sections using SEM images taken at magnifications of 100 and 1000.Cross-sectional X-ray dot maps were collected from corroded areas of the specimens to gain insights on the elemental distribution and the phases present in the corrosion products. X-ray point counts were also obtained from corroded areas to confirm the dot map results. In this report only X-ray dot maps results are presented.

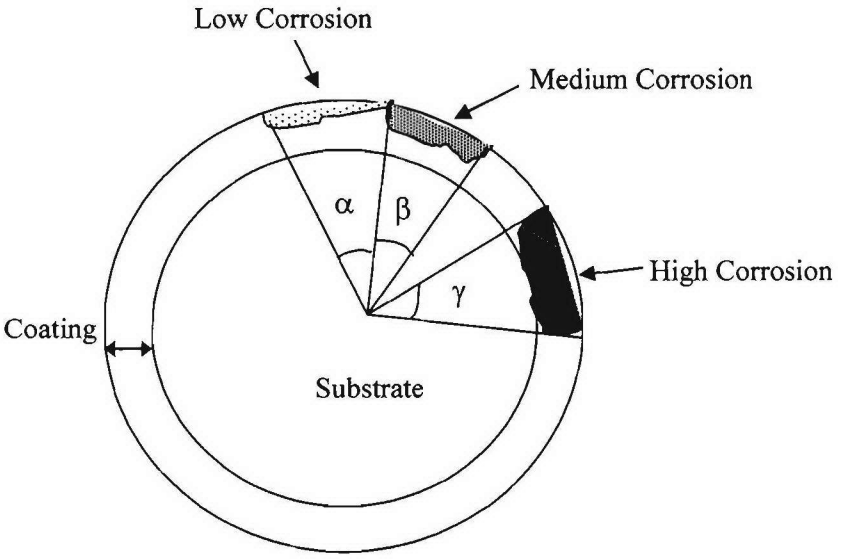

Figure 23. A schematic cross-section of corroded specimen showing extents of different extents of attack, which subtend an angle for measurement.

4. RESULTS AND DISCUSSION

4.1 Hot Corrosion Behavior of Various Aluminide Coatings

4.1.1 High Temperature Hot Corrosion Results (900 °C)

The various coated samples were tested at 900°C (HTHC) for 100, 200 and 500 hours, with a cool-down and salt application after every 20 hours. Digital macro and SEM images of Al-Pt-rich aluminide, Ni-rich aluminides 1 and 2 and CoCrAlY coatings 1 and 2 after 500 hours of total exposure are shown in figures 24-27. The test specimens exposed for shorter times (100h, 200h) were also attacked in similar manners, but to a lesser extent. For the sake of clarity whilst maintaining representative analysis, only the 500 h SEM images are shown and only semi-quantitative results of the extents of attack after 200 h HTHC will be compared. In general, a considerable amount of corrosion product was found in each coating type. The results of the semi-quantitative analyses of the extents of corrosion are summarized in the form of histograms in figures 28 and 29 for 200 and 500 hours of exposure, respectively. Ni-rich aluminide 1 was better after 100h, but more attack was noted after longer times (200 and 500 hours) when compared to Ni-rich aluminide 2.

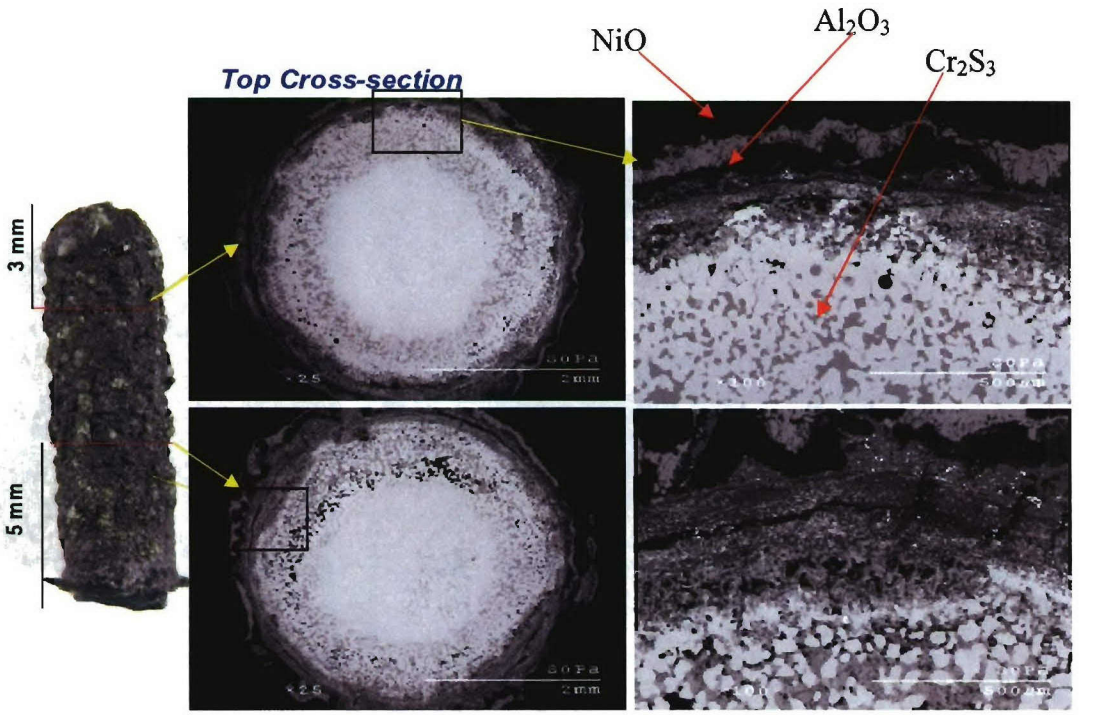

Figure 24. Cross-sectional SEM images of Ni-rich aluminide 1 after 500 hours of HTHC testing at 900°C.

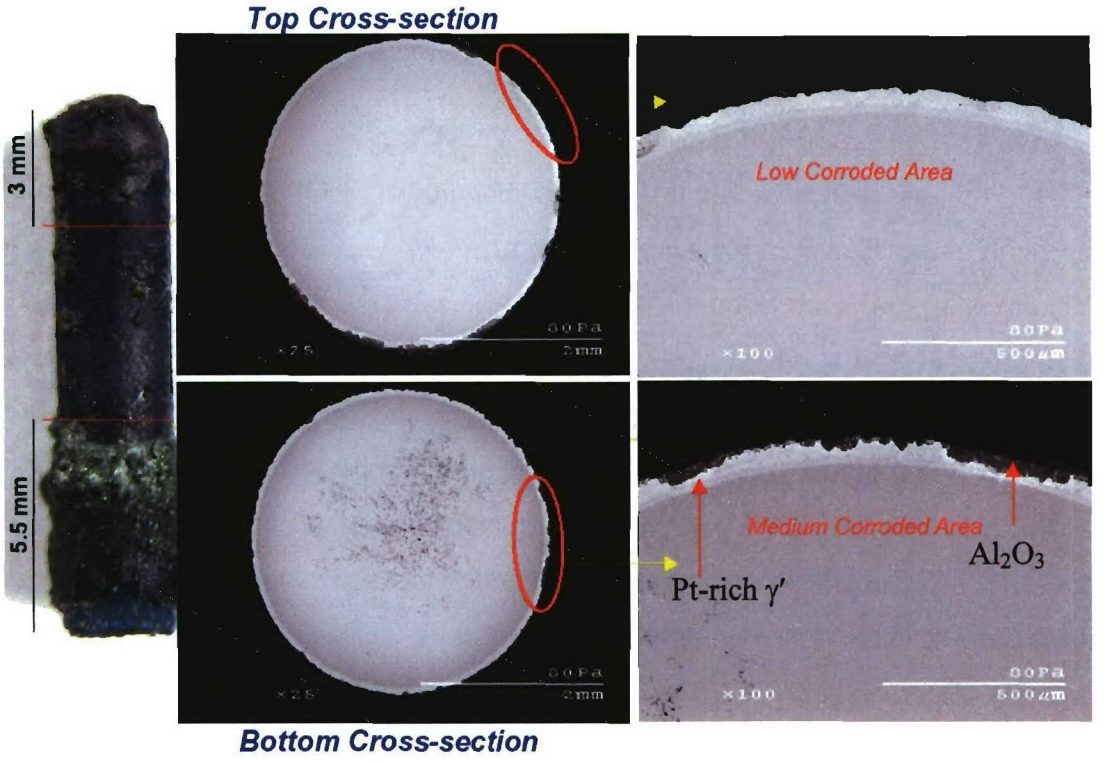

Figure 25. Cross-sectional SEM images of Al-Pt-rich aluminide after 500 hours of HTHC testing at 900°C.

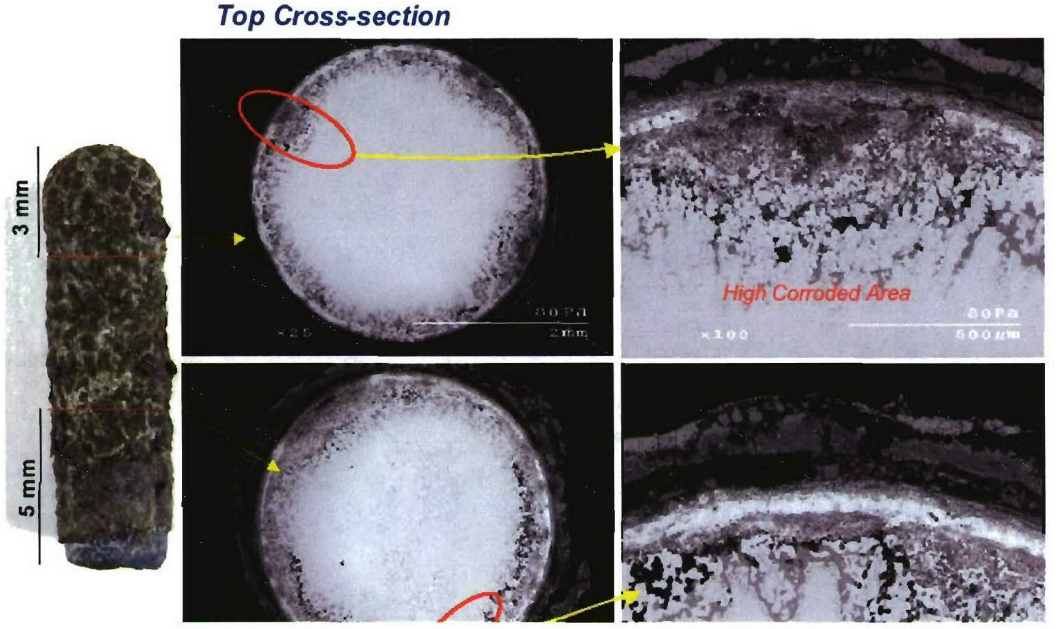

Figure 26. Cross-sectional SEM images of Ni-rich aluminide 2 after 500 hours of HTHC testing at 900°C.

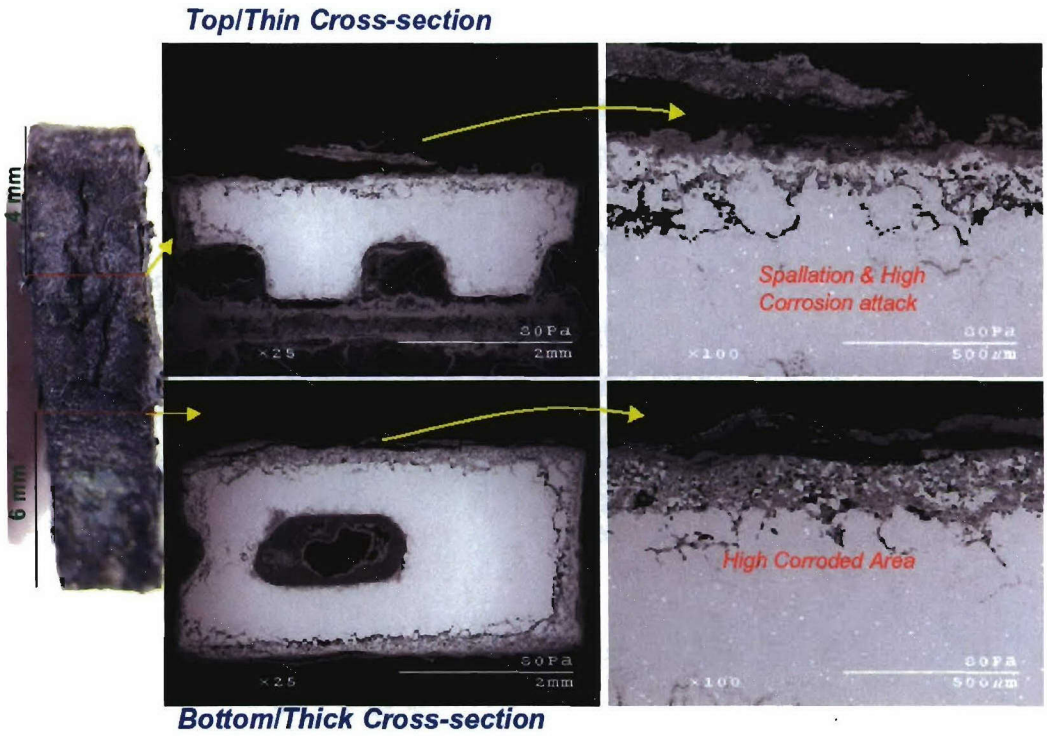

Figure 27. Cross-sectional SEM images of CoCrAlY's 1 and 2 after 500 hours of HTHC testing at 900°C.

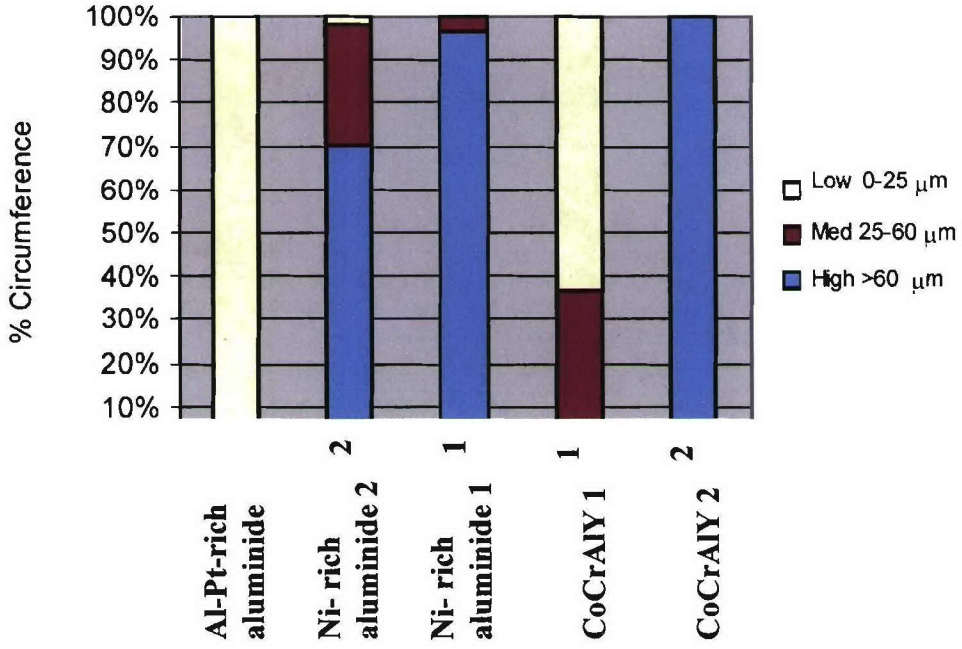

Figure 28. Extents of attack at 900°C (HTHC) along specimen circumference of untreated samples after 200 hours of exposure.

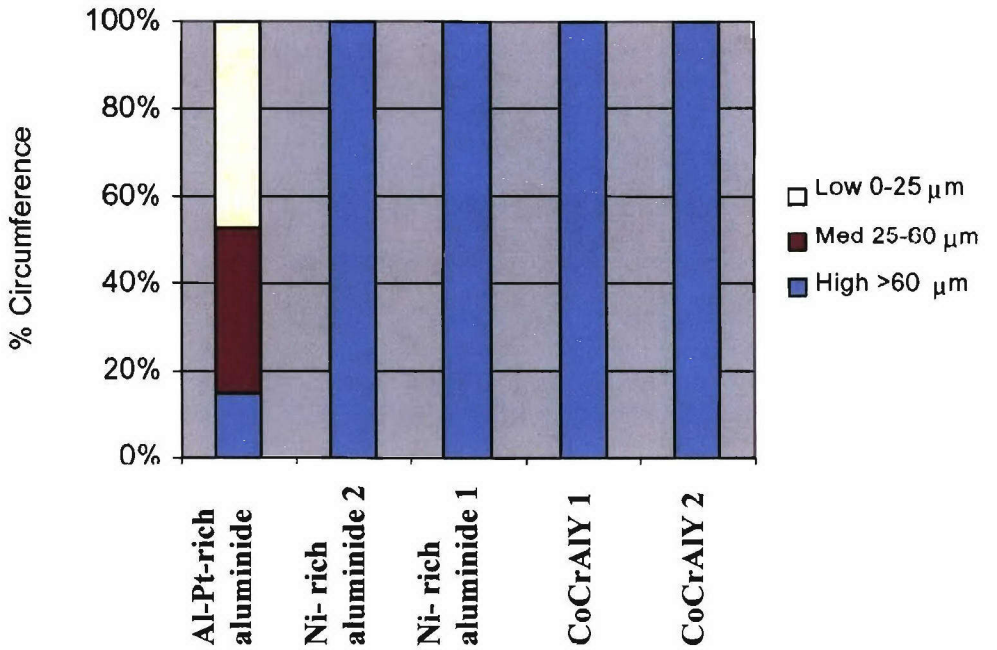

Figure 29. Extents of attack at 900°C (HTHC) along specimen circumference of untreated samples after 500 hours of exposure.

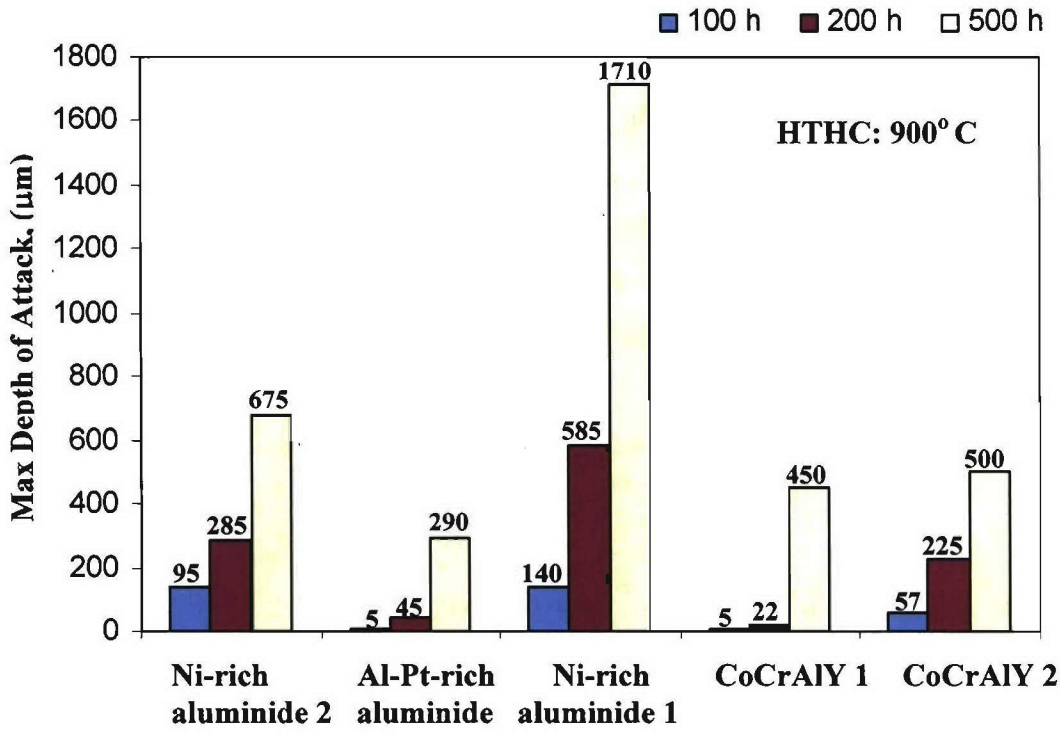

Figure 30. Maximum depth of attack on coating and substrate during HTHC (900°C) testing.

The Al-Pt-rich aluminide and CoCrAlY 1 coated samples showed superior resistance after 100 hours of testing; whereas the CoCrAlY 2 coating was extensively attacked and the Ni-rich aluminides 1 and 2 showed varying levels of all three extents of attack (low, medium and high). With regard to Ni-rich aluminides 1 and 2, the 100 and 200 h results, together with maximum depth of attack measurements (figure 30), suggest that the superalloy 792 substrate confers greater corrosion resistance to this coating than the superalloy 247 substrate. This is at least partly attributable to compositions being different on the different substrates. Specifically, it is believed that the higher HTHC resistance of the Ni-rich aluminide 2 on superalloy 792 substrate for longer times can be partly ascribed to the higher chromium content (13 wt.%) in superalloy 792 compared to superalloy 247 (8 wt.%). Also superalloy 247 has a higher content of the refractory elements W and Ta, which promote topologically closed packed (TCP) phase formation. Such phase formation is detrimental to the oxidation and hot corrosion resistance of the

alloy [113]. It is further noted that superalloy 792 would be intrinsically more resistant to HTHC due to its higher Cr content compared to 247. After 500 hours of exposure Ni-rich aluminides 1 and 2 and CoCrAlY's 1 and 2 were heavily attacked. Only the Al-Pt-rich aluminide exhibited regions of remaining coating, with approximately 50% of the cross-sectional circumference undergoing low (0-25 μm) attack. The present results clearly show that the Al-Pt-rich aluminide coating (on superalloy 792) was the best amongst the coatings tested. The CoCrAlY 1 coating (on superalloy 792) was susceptible to HTHC attack after longer hours of exposure. The results in figure 30 compare maximum depth of penetration into the coatings after 100, 200 and 500 hours of exposure. These results clearly indicate that Ni-rich aluminide 1 shows deeper penetration into the alloy compared to the Ni-rich aluminide 2 coating; although, both systems were heavily attacked after 500 hours of exposure. These results further confirm that Al-Pt-rich aluminide was the best coating to resist HTHC amongst the coatings tested. To summarize, the order of performance from best to worst coating after 500 hours of testing is as follows: Al-Pt-rich aluminide > CoCrAlY 1 > Ni-rich aluminide 2 > Ni-rich aluminide 1 > CoCrAlY 2.

Ni-rich aluminides 1 and 2 had a lower initial Al content compared to Al-Pt-rich aluminide. Aluminide coatings also deplete in Al during HTHC testing due to formation of an Al_2O_3 scale and coating/substrate interdiffusion. The Al depletion eventually causes the β coating to transform into γ'-Ni_3Al. Al-Pt-rich aluminide has a comparatively high Pt (10 at %) content. Higher Pt content helps to form a more planar, adherent and protective Al_2O_3 scale. Pint *et al.* [102] indicated that higher Al content within β-NiAl shows better scale adhesion and oxidation resistance. In order to study the effect of Al content in β-NiAl, an additional set of HTHC experiments was carried out on Ni-47Al (at%)-10Pt (at %) and Ni-37Al (at %)-10Pt (at %) bulk alloys. Ni-47Al-10Pt and Ni-37Al-10Pt are similar in composition to the Al-Pt-rich aluminide and the Ni-rich aluminides 1 and 2, respectively.

Mass loss due to HTHC was more from the Ni-37Al-10Pt alloy compared to the Ni-47Al-10Pt. Cross-sectional SEM images of the alloys shown in figure 31 confirm that Ni-47Al-10Pt formed more protective Al_2O_3 scale. The coated samples were highly corroded after 500 hours of testing and hence the samples exposed for 100 hours were

selected for more detailed elemental analysis (X-ray dot maps and point counts). X-ray dot map of the hot-corroded coating of Al-Pt-rich aluminide after 100 h exposures at 900°C are shown in figure 33. The dot maps indicate the formation of a relatively thick, non-planar and internally oxidized zone containing oxides rich in Al and Cr, presumably Al_2O_3 and Cr_2O_3. Cr- and Ni-rich sulfide precipitates inferred to be Cr_2S_3 and Ni_3S_2 formed beneath this oxide-containing zone. Pt-rich γ'-Ni_3Al was observed within the inner zone of the coating layer below the corroded area. The transformation from β-NiAl to Pt-enriched γ'-Ni_3Al was more in the Ni-rich aluminide coatings 1 and 2 compared to the Al-Pt-rich aluminide coating. Also, higher percentages of spinel ($NiAl_2O_4$) and NiO oxides were observed within the oxide layer found on the Ni-rich aluminides 1 and 2 than on the Al-Pt-rich aluminide. These results were supported by the EDS point counts.

4.1.2 Comparison between Dean Rig and Burner Rig testing

Burner rig tests are often purported to better simulate the actual operating conditions in gas turbine engines; however, such a test requires a long running time and tend to be quite costly. The HTHC resistance of test pins was compared between Dean rig results obtained in this study and burner rig test results obtained by Shifler [114]. Cross-sectional SEM images after 100 hours of Dean rig testing and 1000 hours of burner rig testing are compared in figure 33. HTHC attack seems to be similar in both types of tests, showing formation of a scale consisting of NiO and spinel ($NiAl_2O_4$) oxides at the outside and Al_2O_3 at the inside. Sulfide precipitates rich in Cr and Ni were also observed in the subsurface regions of the coatings. Cross-sectional SEM images of Al-Pt-rich aluminide after burner rig testing showed comparable results and better performance than Ni-rich aluminide 2. The best to worst performance after 100 hours of Dean rig testing was Al-Pt-rich aluminide> Ni-rich aluminide 1 > Ni-rich aluminide 2. Similar performance was observed for 1000 hours of burner rig testing. Equally as noteworthy is the fact that 100 hours of Dean rig testing and 1000 hours of burner rig testing were insufficient to accurately rank the long-term performance of the coatings. HTHC testing after 200 and 500 hours of exposure in the Dean rig provided the necessary information to rank such performance.

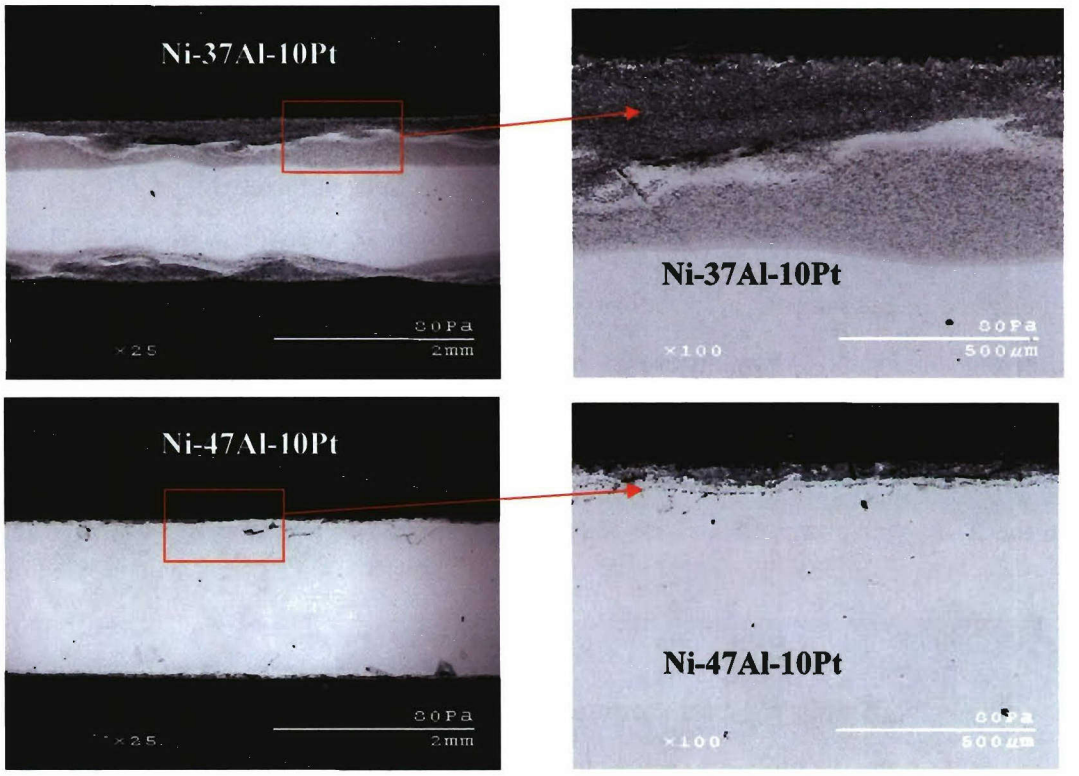

Figure 31. SEM images of Ni-37Al (at%)-10Pt (at %) and Ni-47Al (at%)-10Pt (at %) bulk alloys showing effect Al addition on HTHC resistance in β-NiAl coatings.

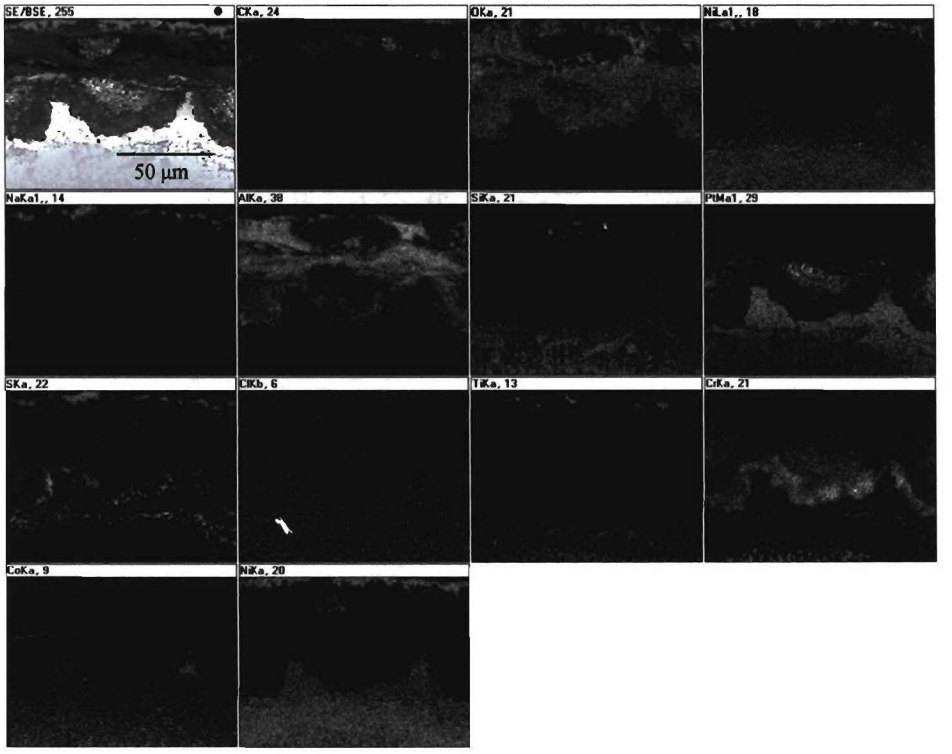

Figure 32. X-ray dot maps for Al-Pt-rich aluminide after 200 hours of exposure at 900°C for HTHC testing showing elemental distribution in coating at 1000x.

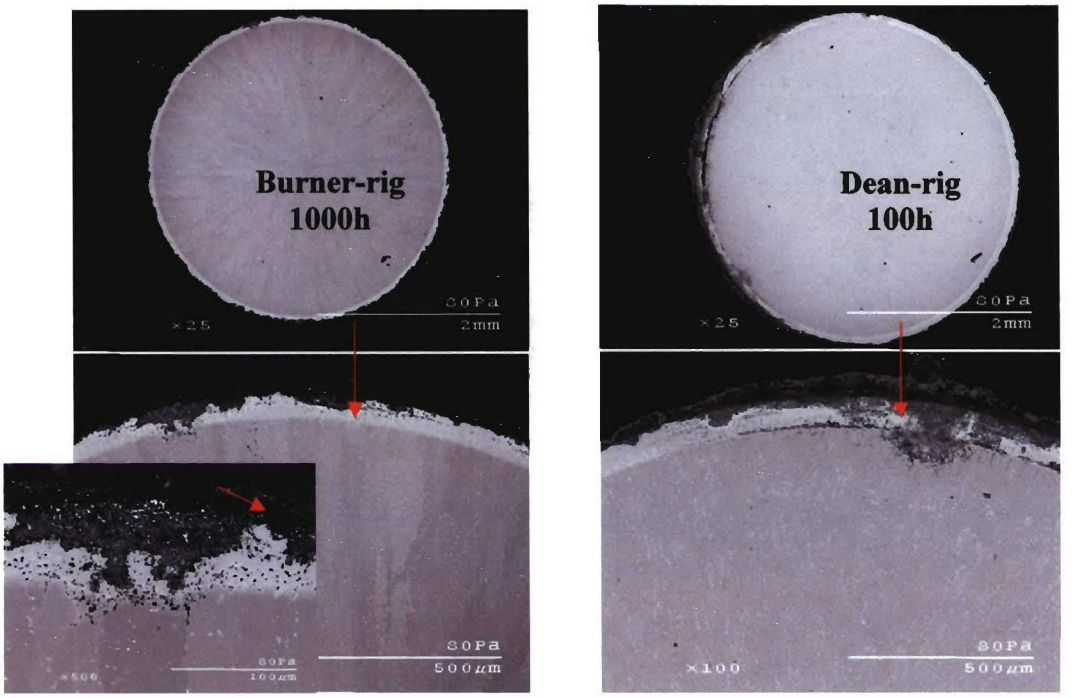

Figure 33. Comparison between hot corroded (900°C) Ni-rich aluminide1 after burner rig (1000h) and Dean rig (100h) testing.

4.1.3 Low Temperature Hot Corrosion Results (705 °C and 750 °C)

Samples with and without pre-oxidation were tested for 100 and 200 hours at 705 and 750°C in 20 hour cycles, as described in the experimental section. Since the melting point of Na_2SO_4 is 884°C, the samples were covered primarily with solid salt deposit during LTHC testing, as indicated by the digital images in figures 35-38. All of the coatings showed localized hot corrosion attack just after 100 hours of exposure. SEM images of the pre-oxidized samples after 200 hours of LTHC exposure are shown in figures 34-38. LTHC attack was highly localized compared to that observed after HTHC testing. Accordingly, the variable of where the sample cross-section is taken becomes very critical for analysis. Semi-quantitative analysis performed on the untreated and pre-oxidized samples are shown in figures 39, 40. The LTHC resistance increased when the samples were pre-oxidized, as observed from the 100 and 200 hours test results. Coatings on the superalloy 792 substrate showed excellent LTHC resistance when pre-oxidized as compared to coatings on the superalloy 247 substrate. This is believed to be due to the fact that superalloy 792 contains higher Cr content and lower TCP forming elements, *i.e.*, W and Ta.

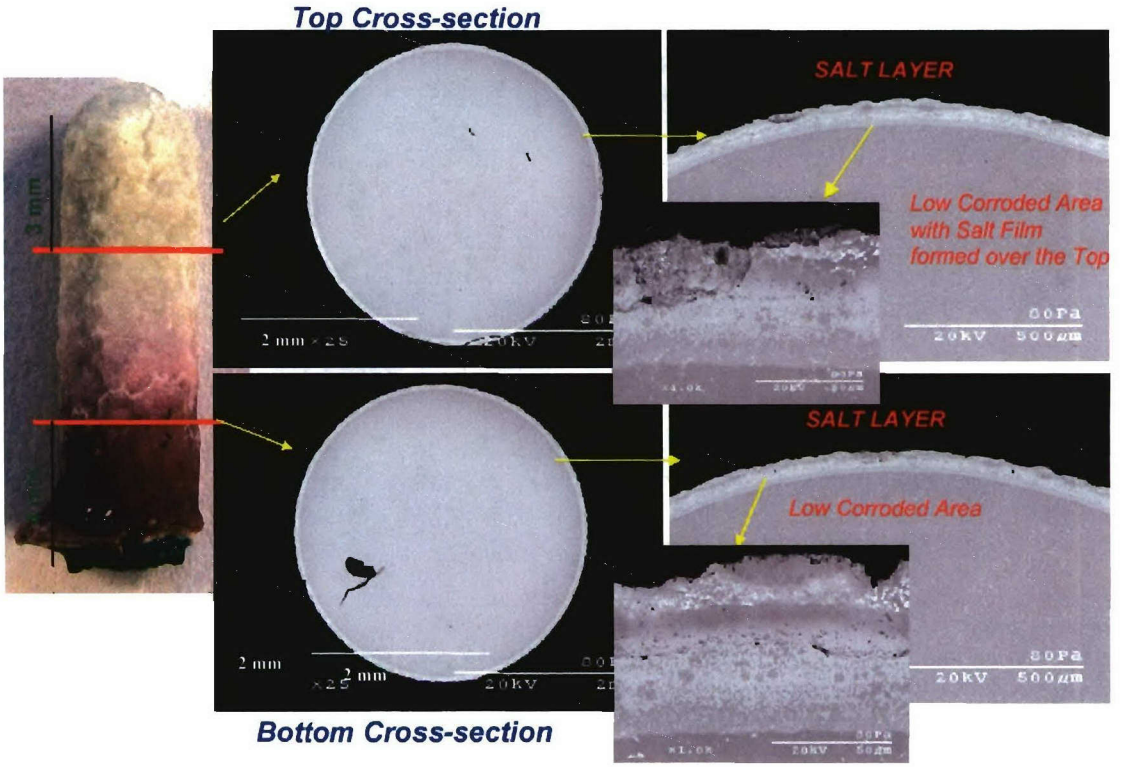

Figure 34. SEM images of pre-oxidized Al-Pt-rich aluminide after 200 hours at 705°C.

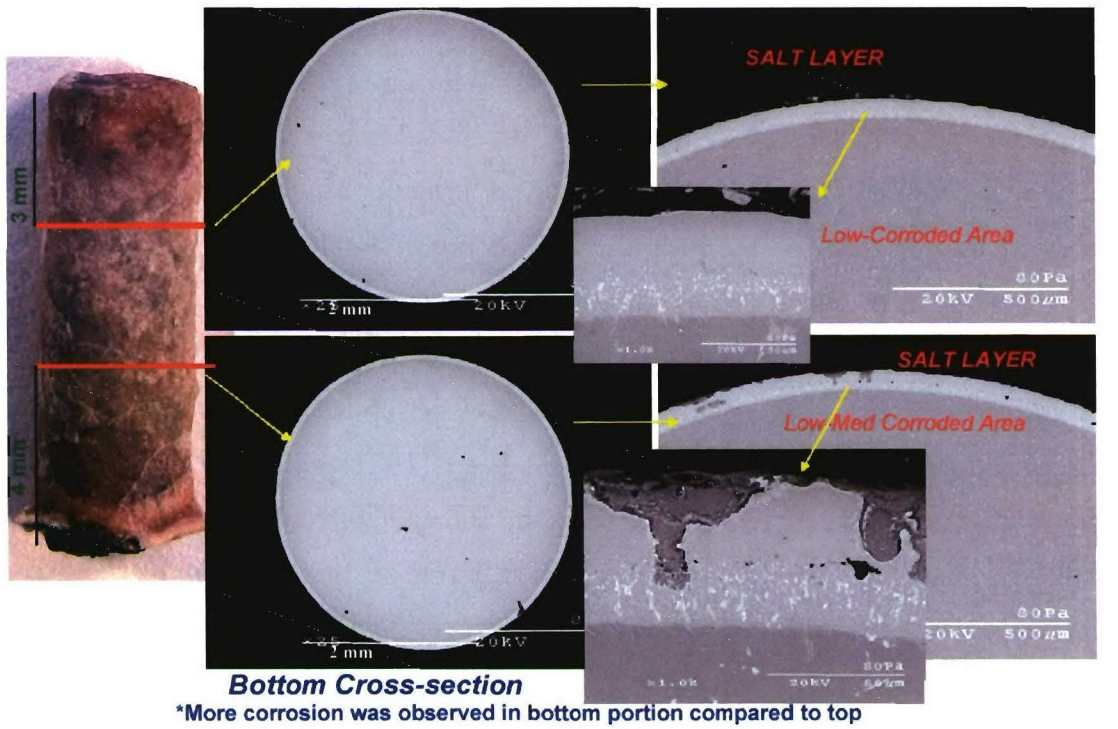

Figure 35. SEM images of pre-oxidized Ni-rich aluminide 2 after 200 hours at 705°C.

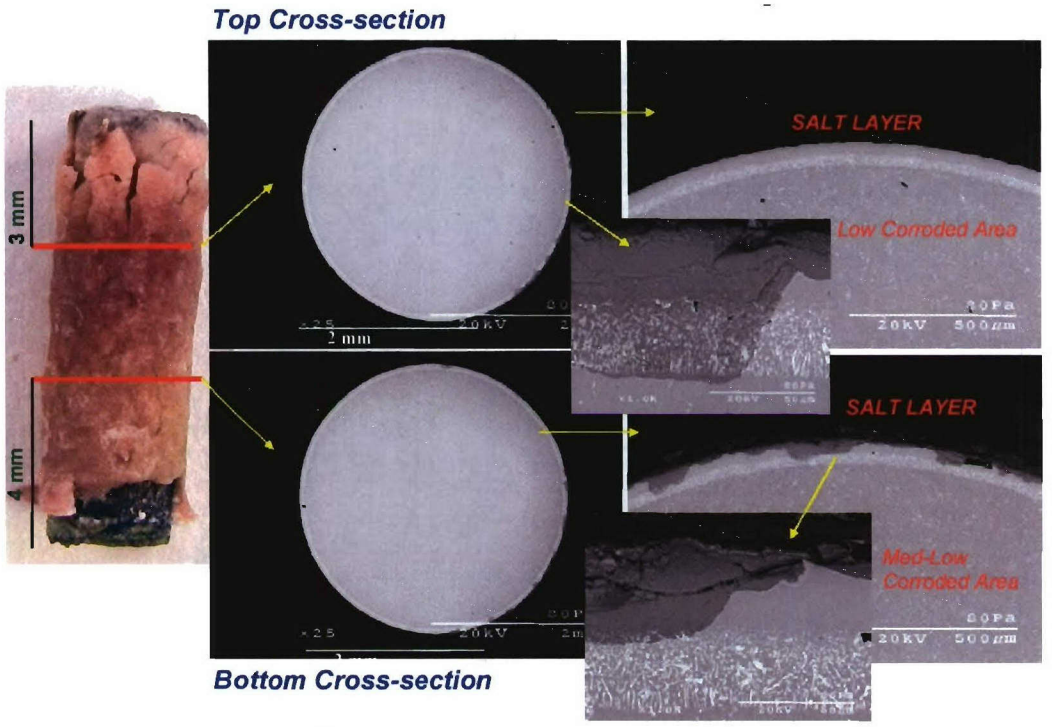

Figure 36. SEM images of pre-oxidized Ni-rich aluminide 1 after 200 hours at 705°C.

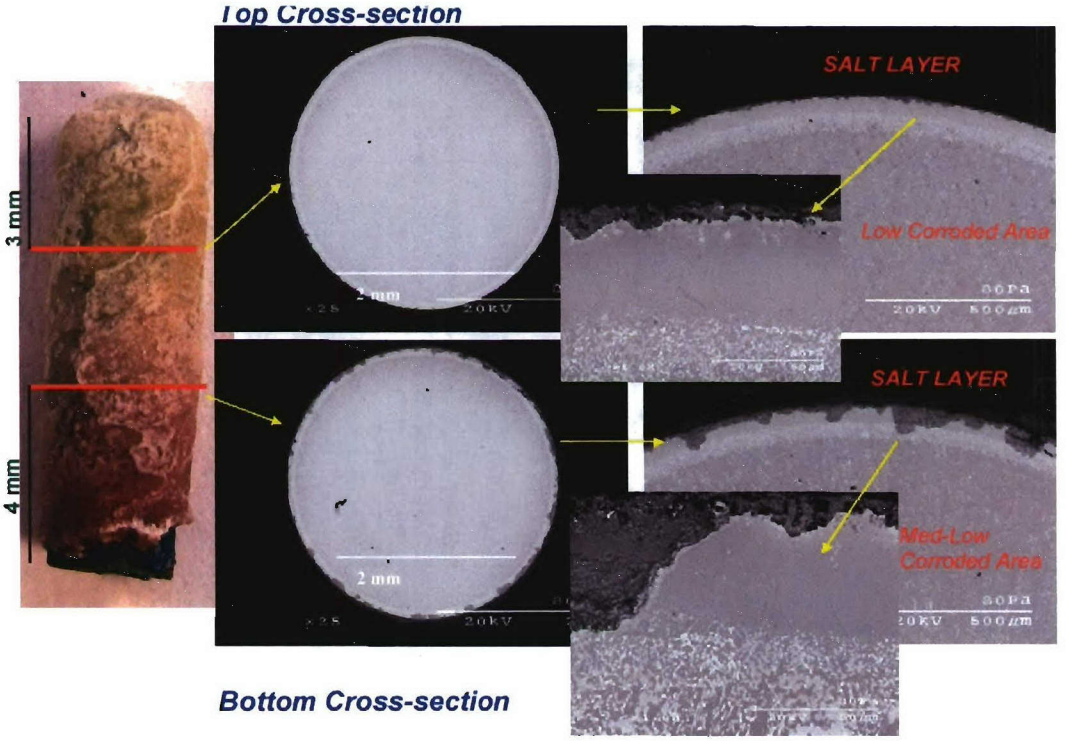

Figure 37. SEM images of pre-oxidized Ni-rich aluminide 3 after 200 hours at 705°C.

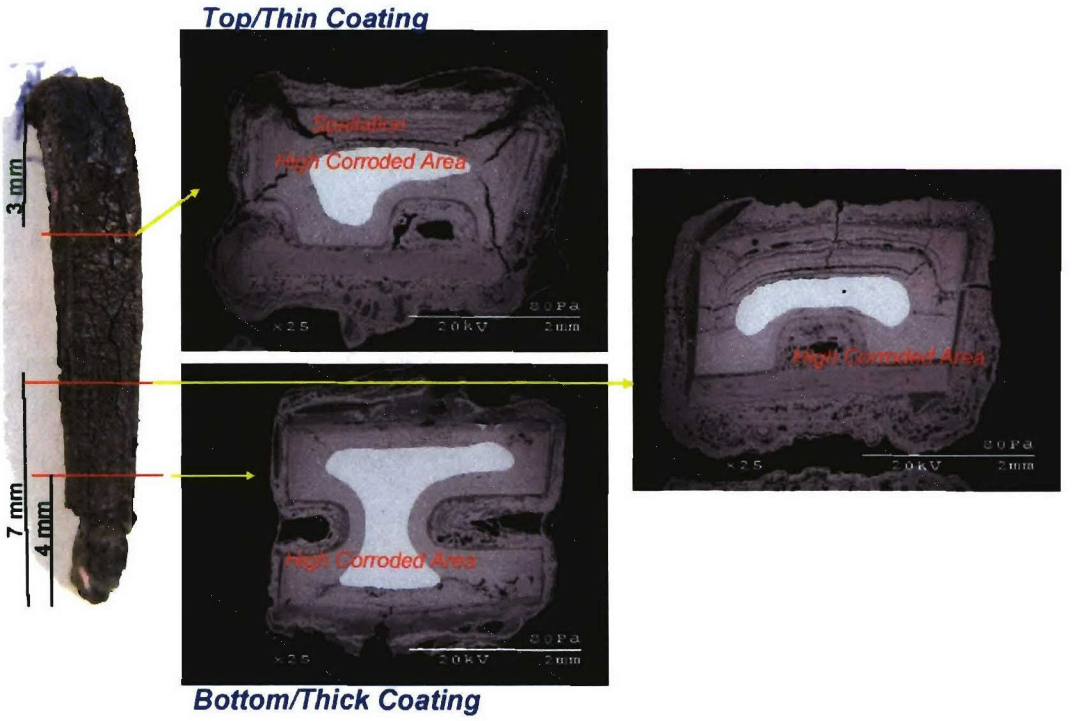

Figure 38. SEM images of untreated CoCrAlY's 1 and 2 after 200 hours at 705°C.

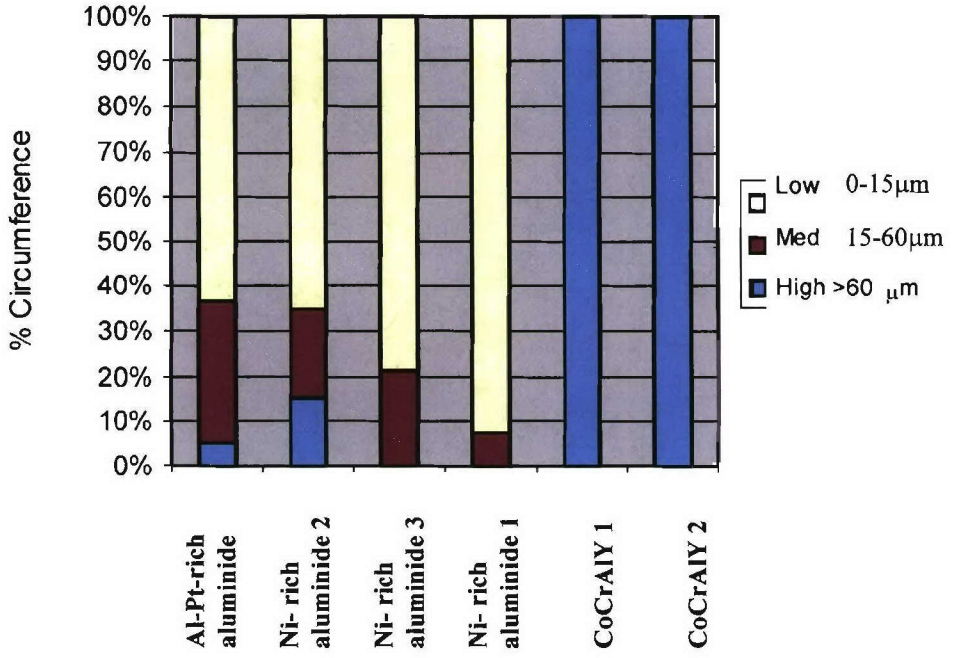

Figure 39. Extents of attack at 705°C (LTHC) of untreated samples after 200 h of exposure

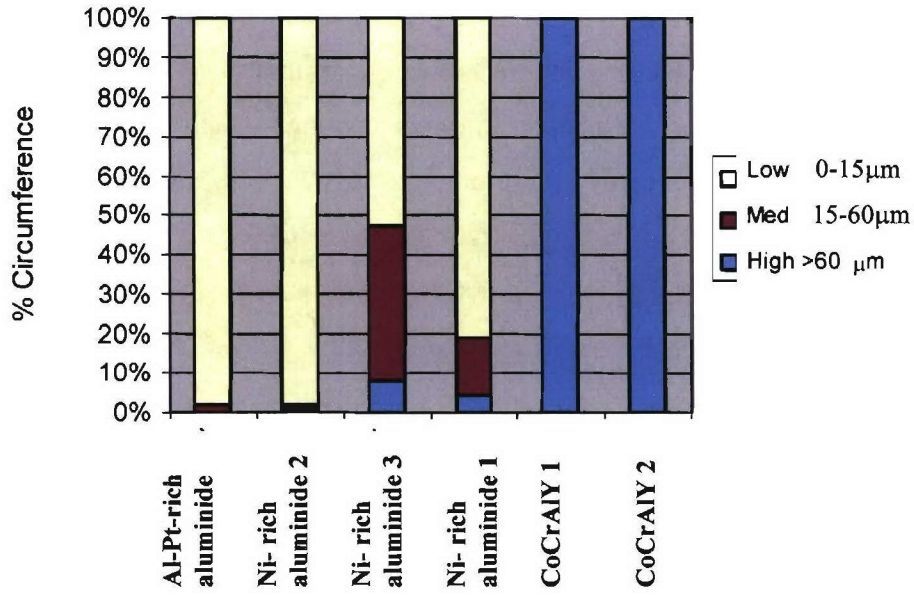

Figure 40. Extents of attack at 705°C (LTHC) of pre-oxidized samples after 200 hours of exposure.

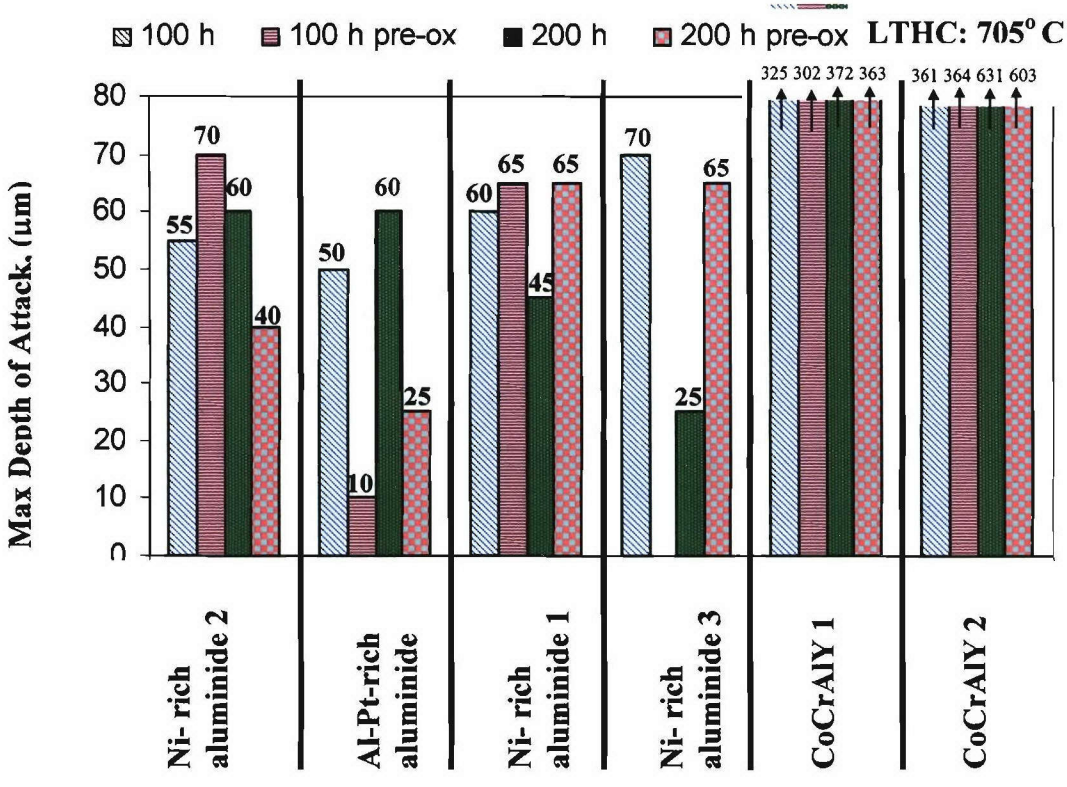

Figure 41. Maximum depth of attack on coating and substrate during LTHC (705°C) testing.

Histograms showing maximum depths of attack (figure 41) indicate that all of the coatings tested were comparable. However, these histograms further show that there is less attack of the pre-oxidized Al-Pt-rich aluminide, which was the most resistant coating to HTHC testing. Pre-oxidation of the Al-Pt-rich aluminide was most beneficial due to the relatively high Al and Pt contents in this coating, which in turn, promoted the formation of a planar, adherent and protective Al_2O_3. The CoCrAlY coatings were completely attacked (*i.e.*, corrosion penetration through the coatings) just after 100 hours of testing, thus showing the worst corrosion resistance. The poor performance of CoCrAlY coatings in Type II conditions is often attributed to the formation of eutectic Na_2SO_4-$CoSO_4$ liquid (T_{melt} = 565°C) liquid resulting from the sulfidation of cobalt oxides present on the surface of the coating [50-53]. $CoSO_4$ (s) could form on Co-based coatings under Type II hot corrosion conditions by the reaction (4).

The Gibbs free energy of formation (ΔG_f) for this reaction was used to calculate the P_{SO_3} versus temperature stability diagram for the Co-S-O system, figure 42. The stability diagram demarcates the regions of solid CoO and solid $CoSO_4$ stability. The equilibrium partial pressures of SO_3 gas for the experimental conditions were also calculated and the results are also plotted on the stability diagram in figure 42. As indicated in this diagram, solid $CoSO_4$ should be the stable phase at the P_{SO_3} and temperature used in this study. Na_2SO_4 (s) in conjunction with sufficient P_{SO_3} can stabilize and form eutectic Na_2SO_4-$CoSO_4$ liquid at a reaction temperature of 705°C. Indeed, Luthra [50] found that cobalt-based alloys undergo Type II attack at low SO_3 pressures in O_2 + 0.15% (SO_2 + SO_3) mixtures. The conditions used by Luthra were very close to those used in the current experiments. In contrast to the Co-based coatings, salt was generally in a solid state on the Pt-modified β-NiAl even after 200h of exposure, but there could have been localized liquid formation resulting in Type II hot corrosion attack. There are at least two possible mechanisms by which Pt-modified β-NiAl undergoes Type II hot corrosion attack, which are described here. According to Rapp and Goto [46], a negative solubility gradient is required for metal oxide fluxing in the melt. Therefore, one of the more likely mechanism for LTHC of Ni based alloys is sulfidation [50, 115, 116]. Experiments carried out to investigate the role of SO_3 and SO_2 on LTHC showed

that a binary Ni-47Al (at %) alloy was heavily attacked only when salt was present in the atmosphere (figure 43). EDS analysis performed on the extensively corroded aluminide-coated samples showed regions of voluminous Al_2O_3 formation. Reaction to form such a product suggests the presence of a liquid salt. Sodium pyrosulfate melts at 365°C, and this pyrosulfate could have formed from the reaction between solid Na_2SO_4 and gaseous SO_3 as shown in reaction (13).

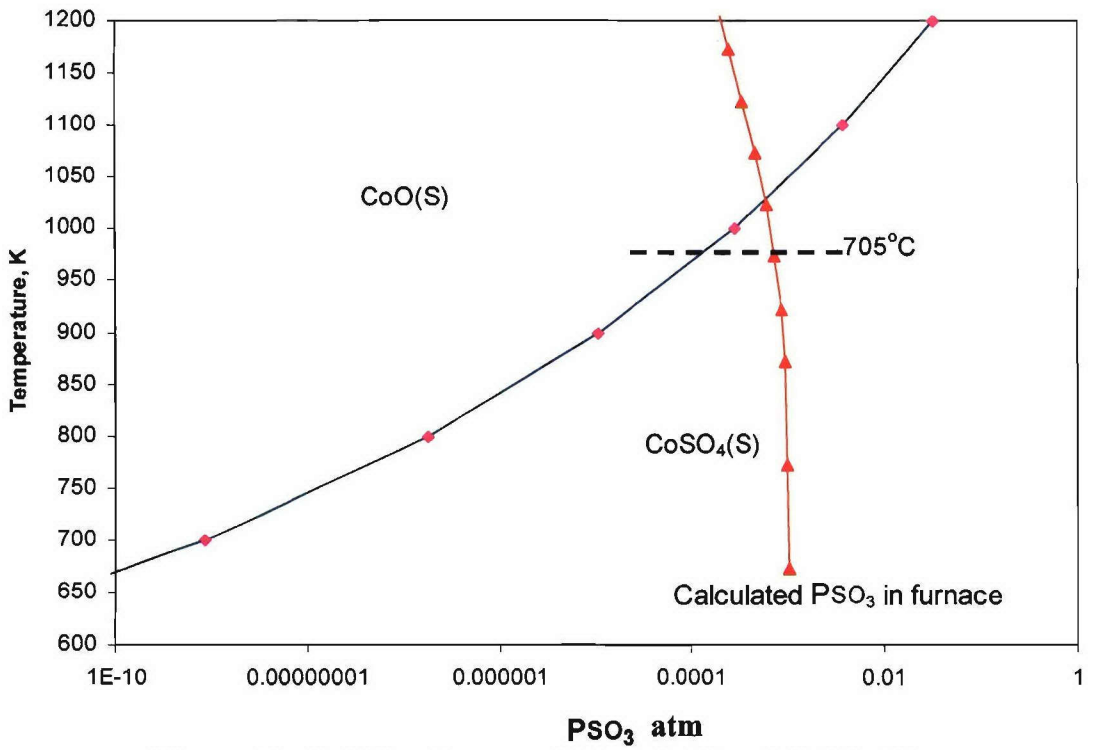

Figure 42. Stability diagram of (a) CoO (S) and $CoSO_4$ (S).

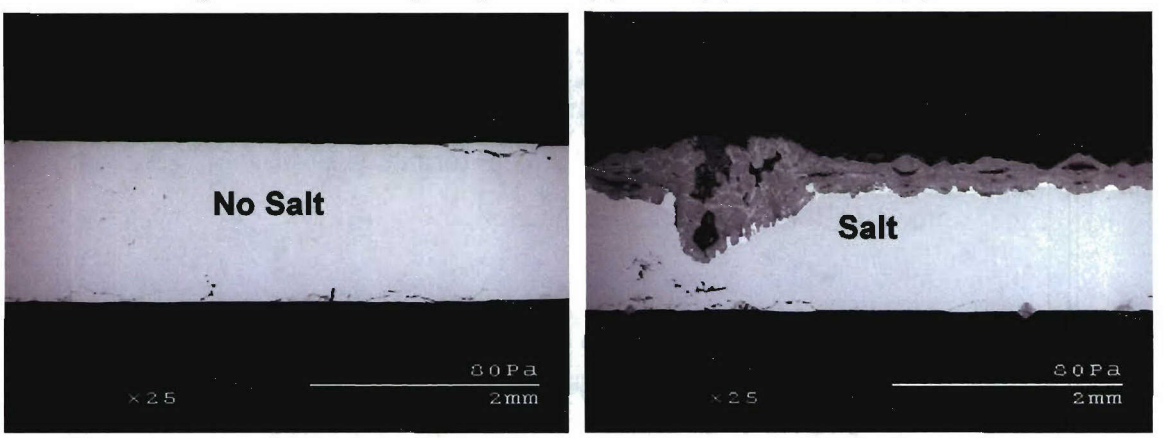

Figure 43. Cross-sectional SEM images of Ni-47Al bulk alloy with and without salt addition at 705°C.

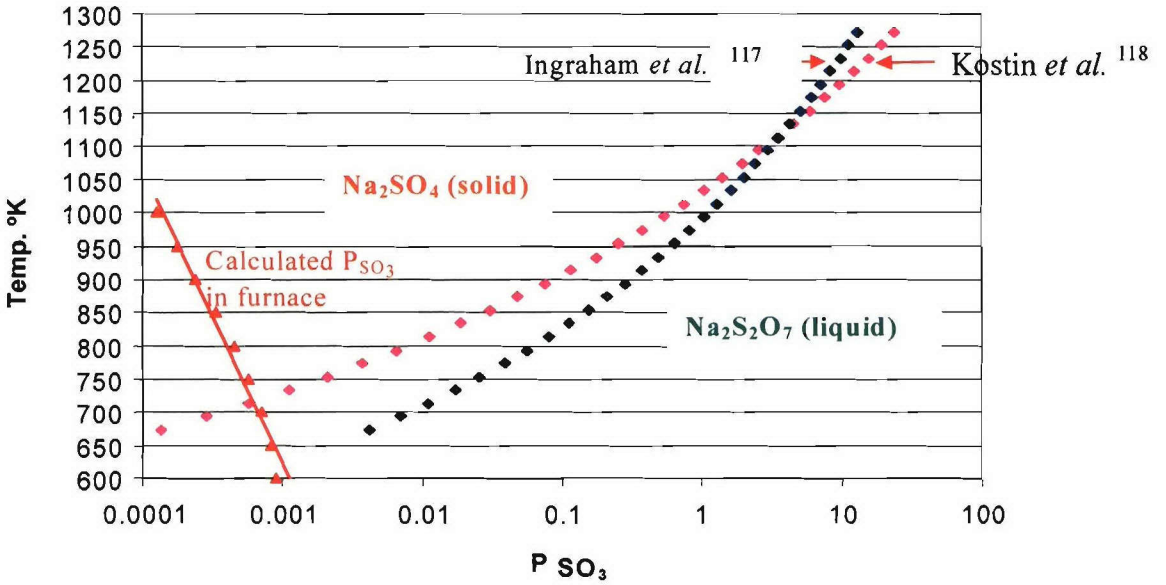

Figure 44. Stability diagram of solid Na_2SO_4 and liquid $Na_2S_2O_7$. The temperature dependence of the equilibrium P_{SO_3} for the test conditions used is also given. This shows that the Na_2SO_4 in contact with the test environment should be solid at the test temperatures of 750°C and 705°C.

Kostin *et al.* [117] and Ingraham *et al.* [118] determined the Gibbs free energy of formation (ΔG_f) for the above reaction. Their ΔG_f values were used to calculate the stability diagram for the Na-S-O system as a function of P_{SO_3} and temperature, figure 64. The stability diagram demarcates the regions of solid Na_2SO_4 and liquid $Na_2S_2O_7$ stability. The equilibrium partial pressures of SO_3 gas for the experimental conditions used were also calculated and the results are also plotted on the stability diagram in figure 44.

In agreement with the SEM images, the stability diagram in figure 45 suggests that the Na_2SO_4 in contact with the test atmosphere should be solid at 750°C (1023 K) and 705°C (978 K). However, there could be local formation of liquid pyrosulfate if the P_{SO_3} at the salt/coating interface increased above the P_{SO_3} in the test atmosphere. This could occur by the following reaction:

$$2\underline{Al} + Na_2SO_4(s) + 3/2\ O_2 \rightarrow Al_2O_3 + SO_3\,(g) + Na_2O\,(s) \quad (19)$$

where $\underline{Al}$ is the aluminum from the coating and/or the Al-containing oxide scale on the coating. While the above reaction is thermodynamically possible, the main drawback to such a mode of local liquid pyrosulfate formation is that the P_{SO_3} would have to increase

to almost 1 atm (see figure 44), which is significant. Sufficient data are not available to further analyze the possibilities and modes for liquid salt formation.

The other possible mechanism involves the formation of eutectic Na_2SO_4-$NiSO_4$ liquid (T_{melt} = 671°C). The oxide scale in Pt-modified β-NiAl may not solely consist of Al_2O_3, as other oxides such as NiO and/or $NiAl_2O_4$ can be at the surface as a consequence of the initial stages of oxidation. $NiSO_4$ (s) could form from NiO under Type II conditions by the following reaction (5).

The ΔG_f value of this reaction was used to calculate the P_{SO_3} versus temperature stability diagram for the Ni-S-O system, figure 45. This diagram suggests that solid NiO should have been stable under Type II conditions used in this study; however, solid $NiSO_4$ could form if the P_{SO_3} at the salt/oxide interface is increased by only ~ 2.5 x 10^{-4} atm above the PSO_3 in the test atmosphere. Such an increase may be possible at the salt/oxide interface owing to an initial oxidation stage and the development of a PSO_3 gradient across the salt deposit. It should be noted, however, that the above assessment does not consider the effect of Na_2SO_4 on the phase stabilities. A study by Lillerud and Kofstad [54] suggests that the chemical activity of $NiSO_4$ is increased in the presence of Na_2SO_4, thus allowing for $NiSO_4$ + Na_2SO_4 liquid formation at lower PSO_3 values than what are indicated in the Ni-S-O stability diagram.

Experiments were also carried out on bulk β-NiAl alloys to investigate the Na_2SO_4 + $NiSO_4$ formation in the Type II conditions. XRD analysis showed that Na_2SO_4, $NiSO_4$ and NiO were indeed formed on the surface of Ni-36Al (at %) and Ni-36Al (at%)-15Pt (at%) alloys after 50 h exposure to the Type II conditions (figure 46). In addition, XRD also showed the presence of $Na_2Ni(SO_4)_2$ (*i.e.*, Na_2SO_4 + $NiSO_4$) on the surface of a Ni-36Al-15Pt alloy .

Type II hot corrosion of Pt-modified β-NiAl was highly localized and was in the form of pits. This is possibly due to localized breakdown of Al_2O_3-rich scale. Al_2O_3 is an acidic oxide in nature and quite a high P_{SO_3} is required for formation of $Al_2(SO_4)_3$. Luthra [50] constructed an Al-S-O stability diagram and suggested that in O_2 + 2% (SO_2 +SO_3) mixtures Al_2O_3 (s) would be stable at 750°C. Hence under the less severe Type II conditions (*i.e.* O_2 + 0.1% (SO_2 +SO_3)) used in this study Al_2O_3 should be stable and it is

only during localized scale breakdown by some thermo-mechanical mechanism that more aggressive hot corrosion attack can occur. It should also be noted that the alumina formed in the temperature range conducive to Type II attack tends not to consist of highly protective α-Al_2O_3, but rather of less protective γ-Al_2O_3 or θ-Al_2O_3. EDS analysis performed in the corroded area showed that the reaction products in the pits are comprised of a sulfate mixture and voluminous Al_2O_3. The external regions of the corrosion products mainly consist of NiO.

The LTHC experiments were also carried out at 750°C. Similar to 705°C testing, a solid salt film apparently formed at 750°C. LTHC attack at 750°C was also localized, similar to that observed at 705°C. Ni-rich aluminide 3 showed more LTHC attack at 750°C compared to the other coatings. It is recalled that Ni-rich aluminide 3 has low Al and Pt contents compared to Al-Pt-rich aluminide; hence, the former may not have as good HTHC resistance.

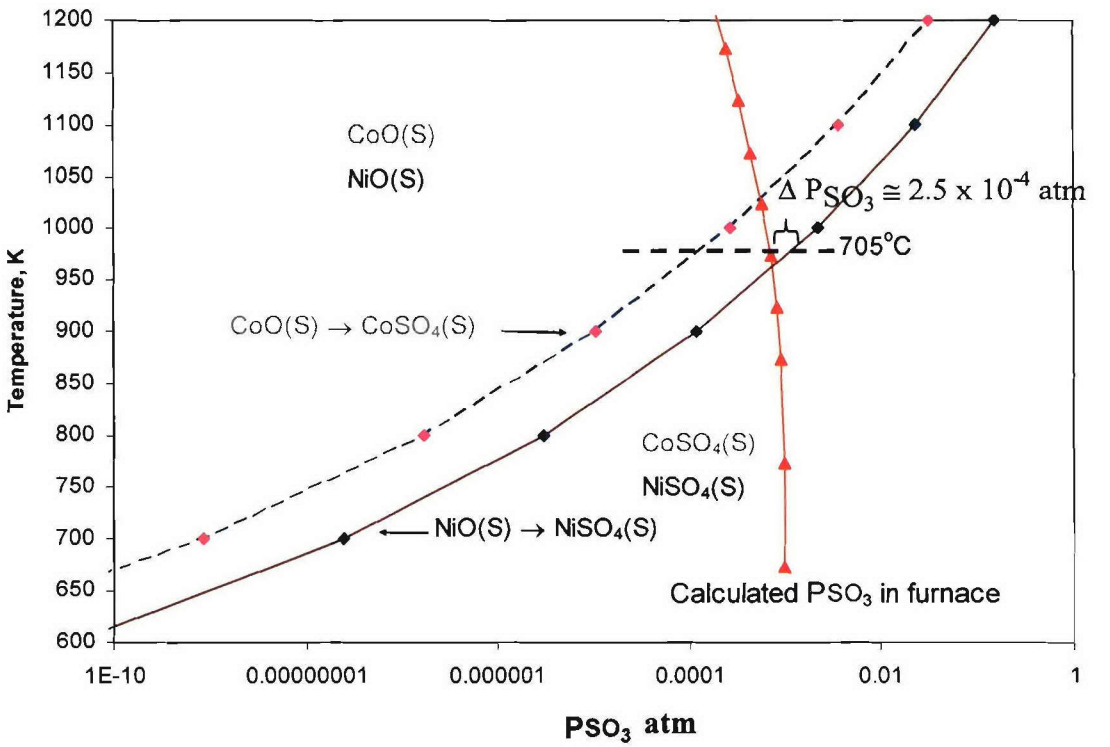

Figure 45. Stability diagram of (a) CoO (S) and $CoSO_4$ (S) and NiO (S) and $NiSO_4$ (S). The temperature dependence of the equilibrium P_{SO_3} for the test conditions used is also given.

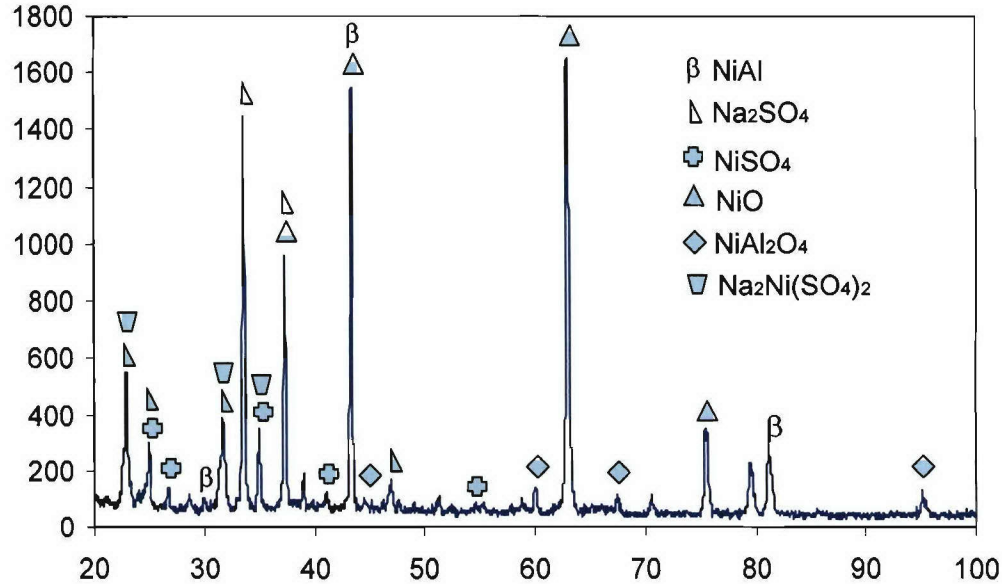

Figure 46. XRD pattern of Ni-36Al (at%)-15Pt (at%) after 50 h of Type II hot corrosion at 705°C.

The HTHC behavior of the Ni-rich aluminide 3 is currently being further assessed by microstructural analyses. The Ni-rich aluminide coatings 1 and 2 were smoother than the Al-Pt-rich aluminide and Ni-rich aluminide 3 coatings, and the former coatings showed very good LTHC resistance when compared to its HTHC resistance. Extents of attack are similar to those at 705°C, except for Ni-rich aluminide 3, which showed much poorer resistance at 750°C. The overall performance of coatings considering both HTHC and LTHC resistance from best to worst is as follows: Al-Pt-rich aluminide> Ni-rich aluminide 2> Ni-rich aluminide 1> Ni-rich aluminide 3> CoCrAlY 1> CoCrAlY 2.

4.1.4 Summary of Hot Corrosion Results

<u>High temperature hot corrosion (HTHC)</u>

- Under HTHC testing conditions it was found that Al-Pt-rich aluminide was the best coating, with overall ranking of coatings in the following order (from best to worst): Al-Pt-rich aluminide > CoCrAlY 1 > Ni-rich aluminide 2 > Ni-rich aluminide 1 > CoCrAlY 2.

- Ni-rich aluminide 1 was good for shorter times (< 100 h) against HTHC – possibly due to the high smoothness of this coating – but underwent deep attack through to the substrate after longer exposures.
- The diffusion aluminides (Ni-rich aluminides 1 and 2) exhibited better HTHC resistance when on the superalloy 792 substrate than on the superalloy 247 substrate after longer exposures (200 and 500 h).
- The CoCrAlY coating was good for HTHC when it was thick.
- More sulfidation was observed in the bottom portion of the pin test samples compared to the top.

Low temperature hot corrosion (LTHC)

- Under LTHC testing conditions (705 and 750°C) the corrosion resistance of the Al-Pt-rich aluminide coating was comparable to the other coatings, but the former does exhibit very good resistance to LTHC compared to the others when it is pre-oxidized.
- Pre-oxidation of the coatings on the superalloy 792 substrate improved LTHC resistance considerably; however, this was apparently not the case for the coatings on the superalloy 247 substrate.
- Thick solid salt films developed on the samples in LTHC, which could have limited general attack of the coupons. However, there was localized attack and this may have been due to the local formation of liquid pyrosulfate.
- The overall ranking of the coatings against LTHC from best to worst is as follows:

Al-Pt-rich aluminide> Ni-rich aluminide 2> Ni-rich aluminide 1> Ni-rich aluminide 3> CoCrAlY 1> CoCrAlY 2.

4.2 Comparative Type II Hot Corrosion study of Co-and Ni-Based Coatings

The benefits of Pt addition to β-NiAl coatings are well known, but there is very limited literature showing effect of Pt addition on Co-based aluminides. The primary purpose of this study was to compare and rank the resistance of the selected Co-based aluminide coatings (CoCrAlY and Pt-modified CoAl) and Pt-modified β-NiAl coating to Type II hot corrosion. The nominal compositions of these alloys are as follows (in wt %):

Superalloy 509: 56.7Co-21.5Cr-10Ni-7W-3.5Ta-0.6C-0.5Zr-0.2Ta.

Superalloy 247: 59Ni-10Co-10W-8Cr-5.5Al-3Ta-1Ti-1.5Hf-0.7Mo

The average chemical composition of each coating was measured via energy dispersive spectroscopy (EDS) analysis and the results are summarized in Table 4.

Table 4. Coating composition and thicknesses of the tested coupons

Alloy	Coating Type and Thickness	Measured Average Composition (at%)
Superalloy 509	CoCrAlY-Convex (65-75 μm)	51Co-25Cr-21Al-2Si-0.7Y
Superalloy 509	Pt-modified CoAl (65-75 μm)	50Al-23Co-9Pt-8Cr-5Ni-2Si-2W-1Fe
Superalloy 792	Pt-modified β-NiAl (60-65 μm)	35Al-9Pt-6Cr-5Co-Bal Ni

SEM images of pre-oxidized Pt-modified CoAl, CoCrAlY (mid-chord section) and Pt-modified β-NiAl coatings after 200 hours Type II hot corrosion are shown in figures 47, 48, and 49, respectively. In general, the Co-based coatings underwent a considerable amount of corrosion. The specimens exposed for shorter times (40h, 100h) were attacked in similar manners, but to a lesser extent. The Pt-modified CoAl coating was extensively attacked, with the coating being completely penetrated by 200 hours of exposure at all three cross-sections. The CoCrAlY coating was also heavily attacked, but it was also only partially attacked in some regions, indicating slightly better resistance compared to Pt-modified CoAl. The Pt-modified β-NiAl coating exhibited the greatest resistance to Type II hot corrosion. Hot corrosion attack of the Pt-modified β-NiAl was highly localized compared to the Co-based aluminide coatings. As a consequence, the variable of where the sample cross-section is taken becomes very critical for analysis of the Pt-modified β-NiAl coating cross-sections. From 100 h test results it was also found that the Pt-modified CoAl coating was attacked to a greater extent than the CoCrAlY

coating. A similar trend of the CoCrAlY coating showing better resistance than the Pt-modified CoAl was observed for the bottom-chord sections. The two types of Co-based coatings were completely attacked in the vicinity of the leading top edge of the airfoil after just 100h of exposure. The Pt-modified β-NiAl exhibited a very small fraction of localized attack after 100 hours of exposure.

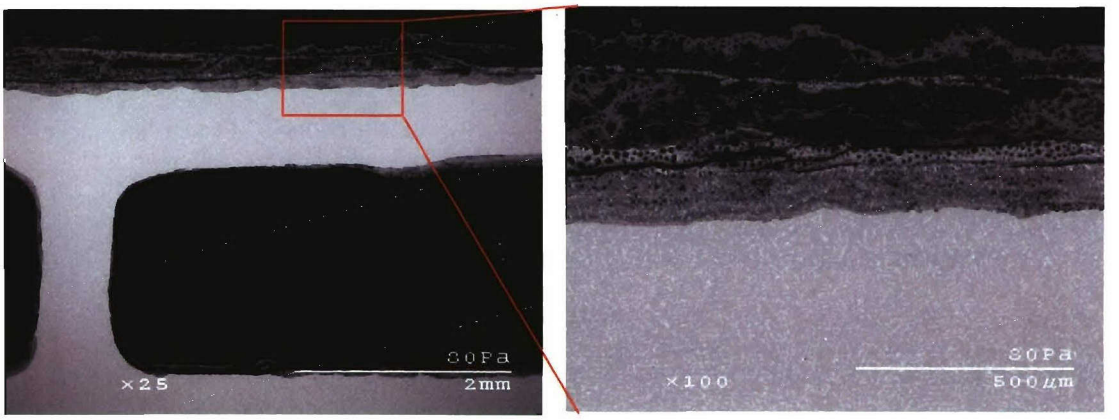

Figure 47. SEM images of Pt-modified CoAl (mid-chord) after 200 hours of Type II HC testing at 705°C.

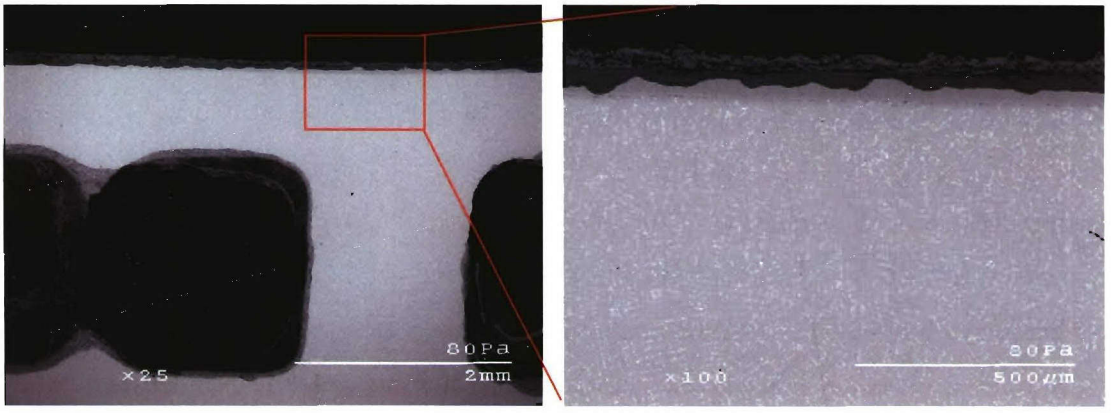

Figure 48. SEM images of CoCrAlY (mid-chord) after 200 hours of Type II HC testing at 705°C.

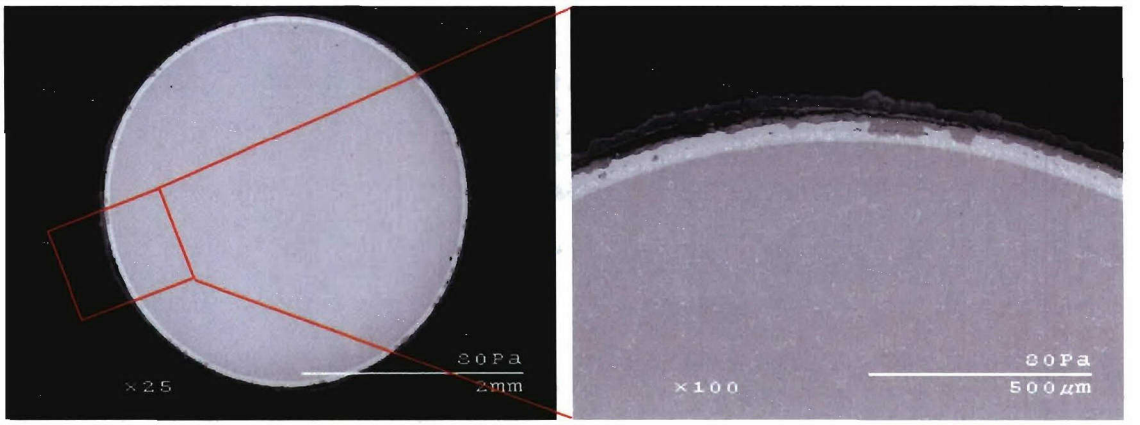

Figure 49. SEM images of Pt-modified β-NiAl after 200 hours of Type II HC testing at 705°C.

Shorter-term Type II hot corrosion experiments were also carried out on the Co-based coatings that were not given any pre-oxidation treatment. These experiments showed a similar trend in performance, with the CoCrAlY coating being generally better than the Pt-modified CoAl coating. The overall ranking of coating performance from best to worst was as follows: Pt-modified β-NiAl > CoCrAlY > Pt-modified CoAl.

EDS analysis of the coating cross-sections was used to deduce the phases present in the corroded areas. Pt-rich phases were intermittently distributed in Pt-modified CoAl coating. The oxide scale that formed on the CoCrAlY coating was primarily CoO with a small fraction of Cr_2O_3; while mixed non-protective scale of CoO + Al_2O_3 + Cr_2O_3 formed on the Pt-modified CoAl coating. It is believed the inferior performance of the Pt-modified CoAl coating compared to the CoCrAlY coating can be partly ascribed to the more heterogeneous phase constitution of the TGO scale formed on the former. This is in accordance with Luthra [51] who found that the simultaneous presence of various oxides can drastically reduce Type II hot corrosion resistance. It should also be noted that Pt-modified CoAl was more brittle than the CoCrAlY coating, which may have also contributed to the inferior performance of the former. Interestingly, examination of the macro-images taken after each 20 hour cycle indicated that the salt deposit on the Pt-modified CoAl coating was completely molten just after 40 hours of exposure; while the salt on the CoCrAlY coating was apparently only semi-molten up to 60 hours. Grisik *et al.* [118] demonstrated that the presence of excess platinum on the

surface of a CoCrAlY coating can increase corrosion rates relative to a platinum free CoCrAlY coating. These results suggest that a relatively high amount of platinum is not beneficial in improving Type II hot corrosion resistance in Co-based coatings.

CoCrAlY is found to be more susceptible to Type II hot corrosion than Pt-modified β-NiAl. The main reasons for this behavior are described here. $CoSO_4$ is more stable than $NiSO_4$ with respect to CoO and NiO, respectively (figure 46). As a consequence, $CoSO_4$ can form at a lower $^{P}SO_3$ than $NiSO_4$. In addition, the eutectic mixture of Na_2SO_4 + $CoSO_4$ has much lower melting temperature (565°C) than that of Na_2SO_4 + $NiSO_4$ (T_{melt} = 671°C); hence CoCrAlY coating is likely to be more susceptible to Type II attack than Pt-modified β-NiAl at lower temperatures. Luthra and Shores [49] also showed that CoO is a better catalyst for the $SO_2 + ½ O_2 \rightarrow SO_3$ reaction than NiO and this will further increase $^{P}SO_3$ at the CoO surface than at the NiO surface.

The effect of platinum in improving Type I and oxidation resistance of β-NiAl is quite well known [67, 68, 72, 73]. In order to study the effect of Pt in β-NiAl for the Type II hot corrosion resistance, an additional set of experiments were carried out using cast β-NiAl bulk alloys Ni-47Al (at%) and Ni-47Al (at%)-15Pt (at%) at 705°C. SEM images of these alloys are shown in figure 50, which show voluminous attack on the binary Ni-47Al alloy, presumably due to liquid salt formation. By contrast, platinum addition up to 15 at% proved quite beneficial in β-NiAl, with the results indicating that only solid salt was on the surface. The Ni-47Al-15Pt alloy exhibited excellent Type II hot corrosion resistance.

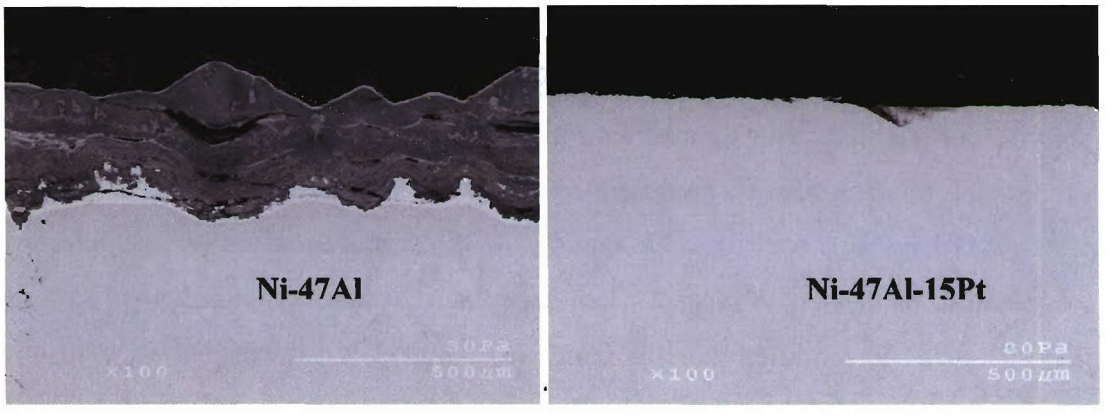

Figure 50. SEM images of Ni-47(at%)Al and Ni-47(at%)Al-15(at%)Pt after 100 hours of Type II Hot Corrosion testing at 705°C.

Summary

Under Type II hot corrosion testing conditions it was found that Co-based coatings underwent extensive attack. The overall ranking was in the following order (from best to worst):

Pt-modified β-NiAl > CoCrAlY > Pt-modified CoAl.

- A highly mixed ($CoO + Al_2O_3 + Cr_2O_3$) TGO scale formed on Pt-modified CoAl, while primarily CoO formed on CoCrAlY during exposure to the Type II conditions. The tendency for the latter to form a simpler scale is believed to contribute to its better corrosion resistance.
- Pt-modified CoAl was more brittle than the CoCrAlY coating, which may have contributed to the inferior performance of the former.
- The Type II hot corrosion attack in Co-based aluminide coatings is attributed to the formation of eutectic Na_2SO_4-$CoSO_4$ ($T_{melt} = 565^{\circ}C$) liquid. The localized attack in Pt-modified β-NiAl was possibly due to the eutectic Na_2SO_4-$NiSO_4$ ($T_{melt} = 671^{\circ}C$).

Platinum addition to Al-rich β-NiAl alloys improves Type II hot corrosion resistance.

4.3 Hot Corrosion and Oxidation Behavior of Pt+Hf-Modified γ-Ni + γ′-Ni_3Al Alloys

4.3.1. Type I Hot Corrosion (900°C)

Various β-based alloys were hot-corrosion tested at 900°C for 100 hours, with cool-down and salt application after every 20 hours. The observed decrease in weight gain with increasing Pt content confirms the generally accepted fact that Pt addition improves HTHC resistance of β-based alloys and coatings [67, 68, 72, 73]. Pre-oxidation of these alloys was not beneficial in further improving HTHC resistance. β-NiAl alloys with low Al (37 %) content, showed extensive attack even with higher Pt additions (30%).

The focus of current research was to optimize hot corrosion resistance of Pt-modified γ + γ′ alloys that have excellent oxidation resistance. A set of such alloys having a fixed Al content of 22% were tested for HTHC resistance and the weight gain after 100 hours of exposure is shown in figure 51. Addition of up to 10% of Pt to the binary alloy (Ni-22Al-1wt%Hf) decreased weight gain, but further Pt addition caused the weight gain to increas. Cross-sectional SEM images of binary and Pt-modified γ and γ′ alloys are shown in figure 52. These images confirm that up to 10% Pt addition helped considerably to improve hot corrosion resistance of the alloys, but higher amounts of Pt addition (20 and 30 at %) showed extensive HTHC attack. As will be discussed, this is attributed to higher Ni_3S_2 formation with higher Pt content (above 10 at %). Pre-oxidation of the alloys was beneficial only in binary and low Pt (5 at %) containing alloys. EPMA was used to analyze the phases formed during the testing duration. During the early stages of degradation, the outermost region of the scale product consisted of NiO, and this was followed by layers or zones rich in $NiAl_2O_4$ and α-Al_2O_3. There was also the internal formation of Al_2O_3 precipitates. A Pt-rich γ′ layer typically formed in the alloy subsurface in contact with the scale. Internal precipitates of Ni_3S_2 were commonly detected within a given alloy, beneath the Pt-rich γ′ layer. Figure 53 schematically summarizes the early stages of HTHC of the PT-modified γ+ γ′ alloys.

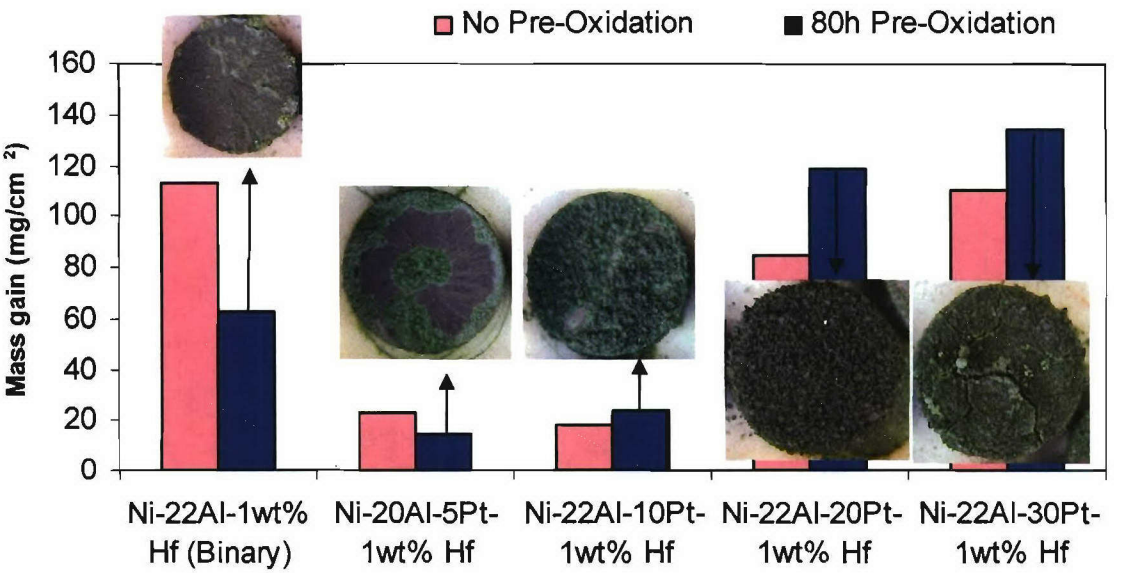

Figure 51. Weight gain and corresponding macro-images of Pt-modified γ+ γ′ alloys with and without pre-oxidation.

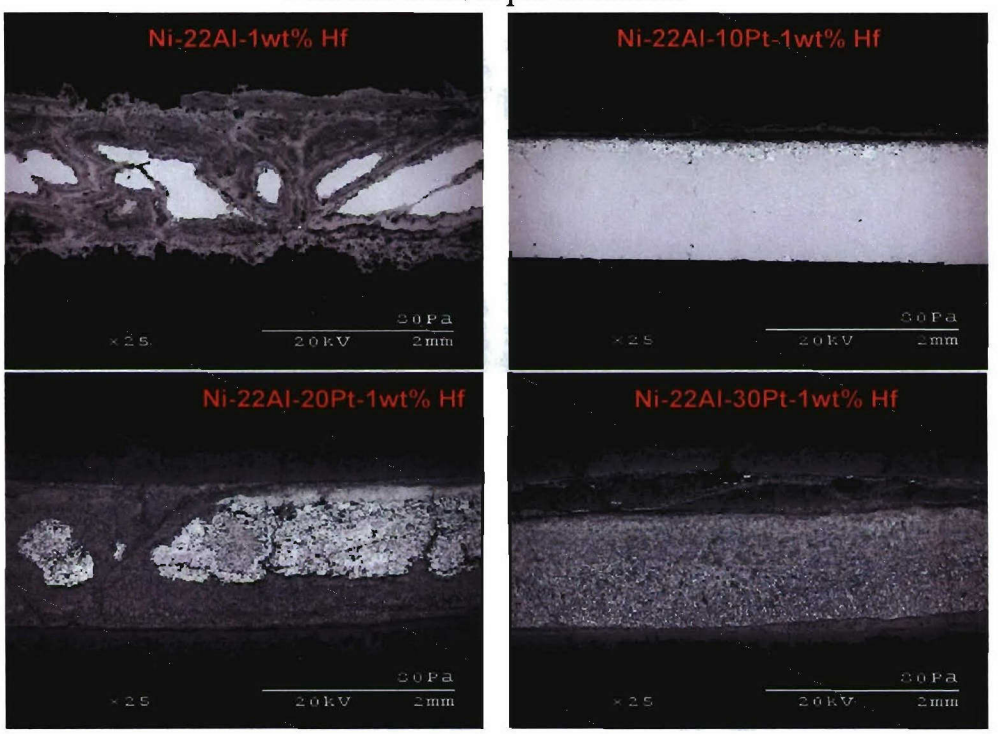

Figure 52. Cross-sectional SEM images of Pt modified (*Ni-22Al-XPt-1wt%Hf*) γ+γ′ alloys after HTHC testing for 100 hours. The alloys were not pre-oxidized.

An Ellingham diagram comparing the stabilities of Ni_3S_2 and Al_2S_3 is shown in figure 54 [120]. This diagram suggests that Al_2S_3 is more stable than Ni_3S_2 at

900°C but the difference in the Gibbs free energy of formation (ΔG_f) between them is not very large.The displacement reaction between Al_2S_3 and Ni_3S_2 transformation is given by reaction (20).

$$3Ni\ (s) + 2/3\ Al_2S_3\ (s) \rightarrow 4/3\ Al\ (s) + Ni_3S_2\ (L) \qquad (20)$$

Although Al_2S_3 is more stable at 900°C, it should be noted that we have found in a different study that Pt addition decreases the chemical activity of Al (a_{Al}), but increases the activity of nickel (a_{Ni}). Thus, increasing Pt eventually favors the formation Ni_3S_2 in preference to Al_2S_3. This results in accelerated attack at 900°C because Ni_3S_2 melts at 787°C. Gulvanitskaya *et al.* [121] studied the Pt-Ni-S system and proposed that a eutectic mixture of Ni_3S_2 and Ni-Pt solid solution have the lowest melting region at 734-775°C. Hot corrosion testing of Ni-22Al-(5, 10 and 15 %) Pt also show that a higher amount of Ni_3S_2 forms with increasing Pt addition. Ni_3S_2 formation in Ni-22Al-30Pt-1wt%Hf alloy was observed only after 20 hours of exposure (figure 55). Representative X-ray dot map of this latter confirmed the Ni_3S_2 formation. Pre-oxidation of high Pt (20 and 30%) alloys apparently further decreased a_{Al}, due to the formation of Al_2O_3 scale thereby favoring higher % Ni_3S_2 formation. Hence pre-oxidation of these alloys did not improve their HTHC resistance.

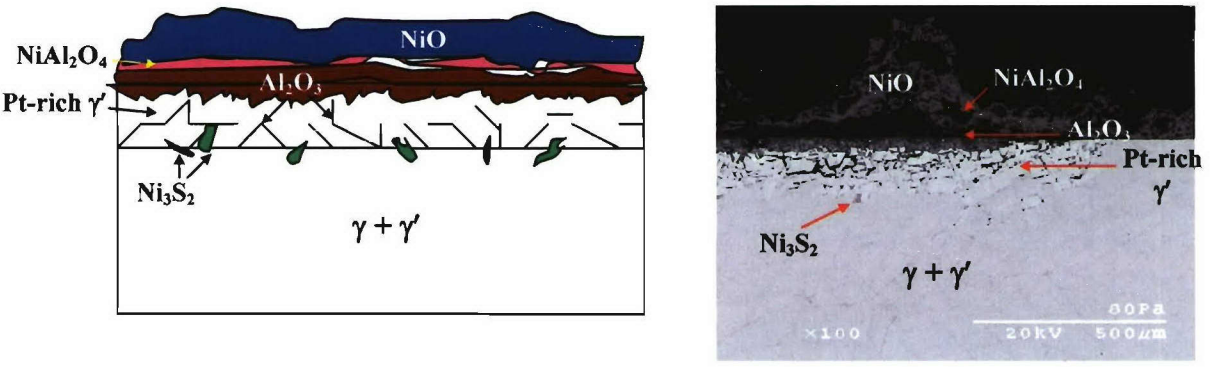

Figure 53. Schematic and cross-sectional SEM of a typical Pt-modified γ+γ′ alloy during the early stages of hot corrosion at 900°C.

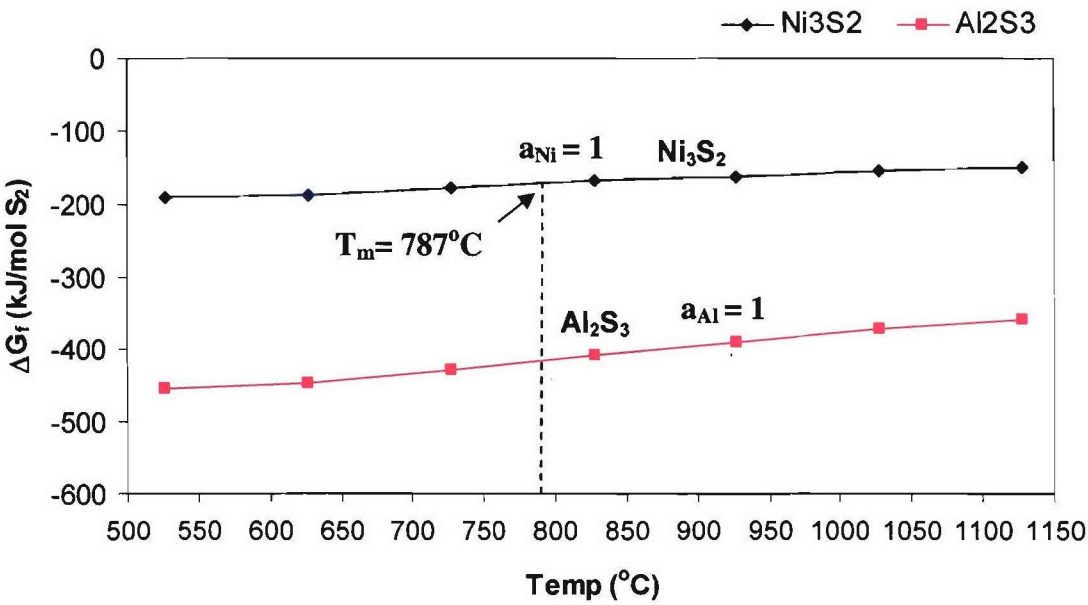

Figure 54. Ellingham diagram of Ni and Al sulfides per mole of S_2 [120].

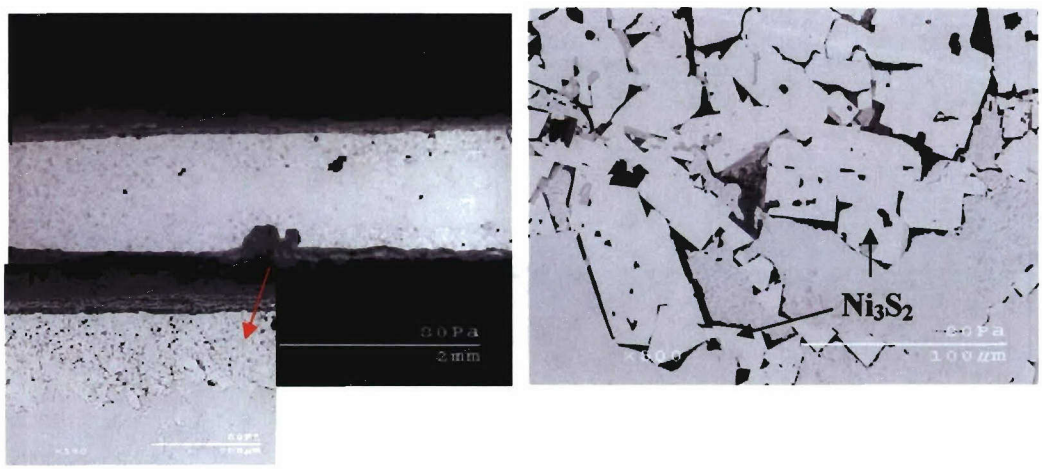

Figure 55. Formation of Ni_3S_2 in the Ni-22Al-30Pt-0.35Hf alloy after 20 hours HTHC.

It is known that chromium addition improves hot corrosion resistance of a superalloy [36]. Malush [76] and Dust [78] reported that Cr+Pt modified β-NiAl coatings have excellent resistance to hot corrosion at 900 and 700°C, respectively. During the past two decades, a reasonable amount of research focused on Cr- and Pt-modified β-NiAl coatings for improved hot corrosion resistance [69, 72, 73]. Since Cr and Si additions improve hot corrosion resistance in aluminide coatings and superalloys, Cr and Si were added to low-Pt γ+γ′ alloys to improve their high-temperature hot-corrosion (HTHC) resistance. The weight gains of Ni-22Al-20Pt-1wt%Hf alloys with and without Cr addition are shown in

figure 56. Addition of 20at% Cr significantly improves HTHC resistance of Ni-22Al-20Pt-1wt%Hf containing alloy. Cross-sectional SEM images of the pre-oxidized Ni-22Al-20Pt-20Cr-Hf alloys are shown in figure 57. The addition of 20 at.% Cr also changed the microstructure of the 22 at.% Al + 20 at.% Pt alloy from $\gamma+\gamma'$ to $\gamma+\gamma'+\beta+\alpha$.

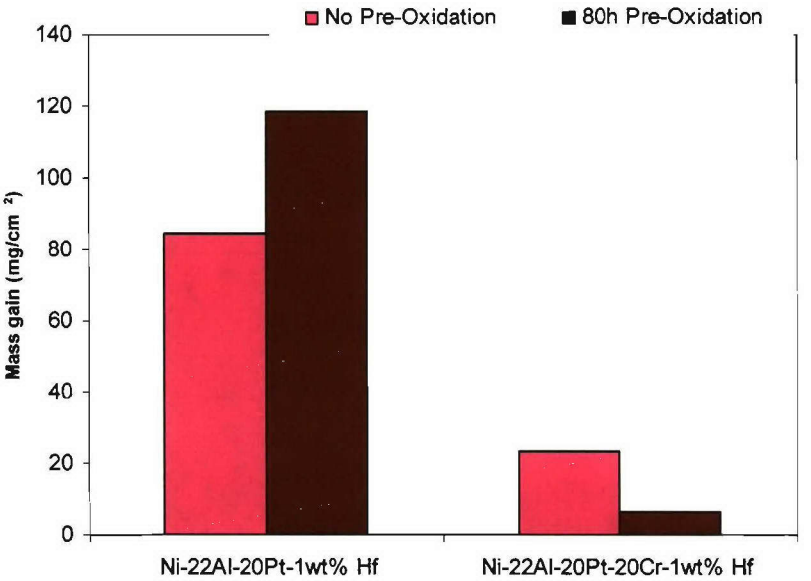

Figure 56. Effect of 20 at.% Cr addition on the 900°C hot-corrosion resistance of a Ni-22Al-20Pt-1wt.%Hf $\gamma+\gamma'$ alloy exposed for a total of 100 hours.

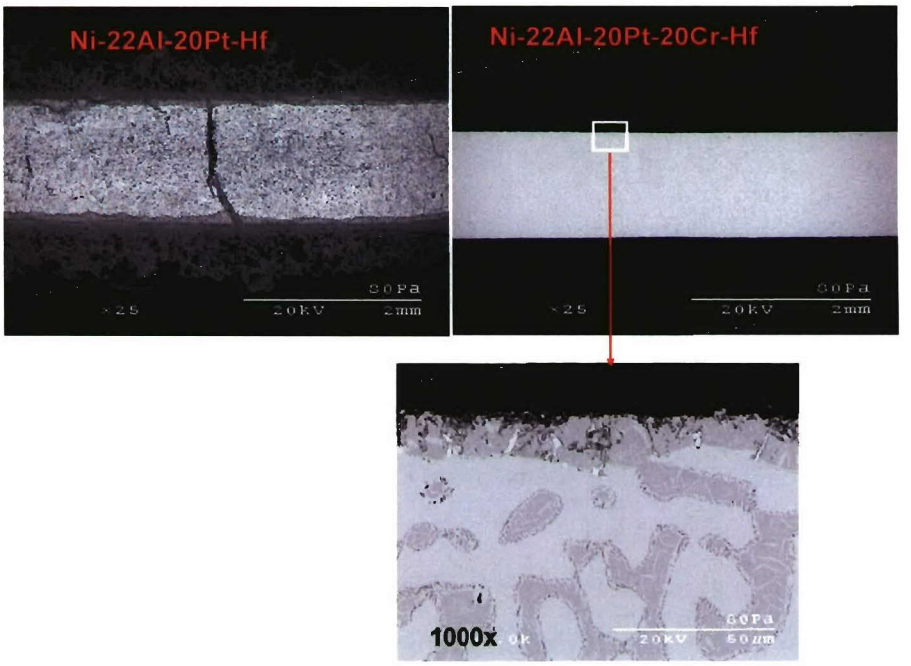

Figure 57. Corresponding (figure 56) cross-sectional SEM images.

The weight gains of Cr-modified, low-Pt (*i.e.*, 10 at.%) alloys after 100 h HTHC testing are shown figure 58. Alloys with as low as 10 at% of Cr are shown to have excellent HTHC resistance. Cross-sectional SEM images of pre-oxidized Ni-22Al-10Pt-Cr-1wt%Hf alloys after 100 h HTHC testing are shown in figure 59. It is seen that Ni-22Al-10Pt-10Cr-1wt%Hf and Ni-22Al-10Pt-20Cr-1wt%Hf are exceptionally resistant to HTHC. A lower amount of chromium was not beneficial to HTHC resistance; Ni-22Al-10Pt-5Cr-1wt% Hf showed a considerable amount of spallation even after pre-oxidation. The results for the low-Pt-modified (up to10at %) $\gamma+\gamma'$ alloys suggest that the Cr content should be either equal to or greater than Pt content for improved hot-corrosion resistance. It should be noted that the $\gamma+\gamma'$ phase constitution is retained for the Cr-modified, low-Pt containing alloys. Apart from Pt and Cr as well known additions to aluminides, silicon has also been found to improve hot corrosion resistance of aluminide coatings [25, 71, 88]. Hence, silicon was added (up to 10 at %) to Pt-modified $\gamma+\gamma'$ alloys and results are included in figures 58 and 59. It is seen that the addition of 5 at.% Si to the base $\gamma+\gamma'$ alloy is quite beneficial to hot-corrosion resistance. The addition of more than 5 at% Si was not beneficial since the alloy microstructure was quite porous due to the formation of a liquid phase during heat treatment above about 1165°C.

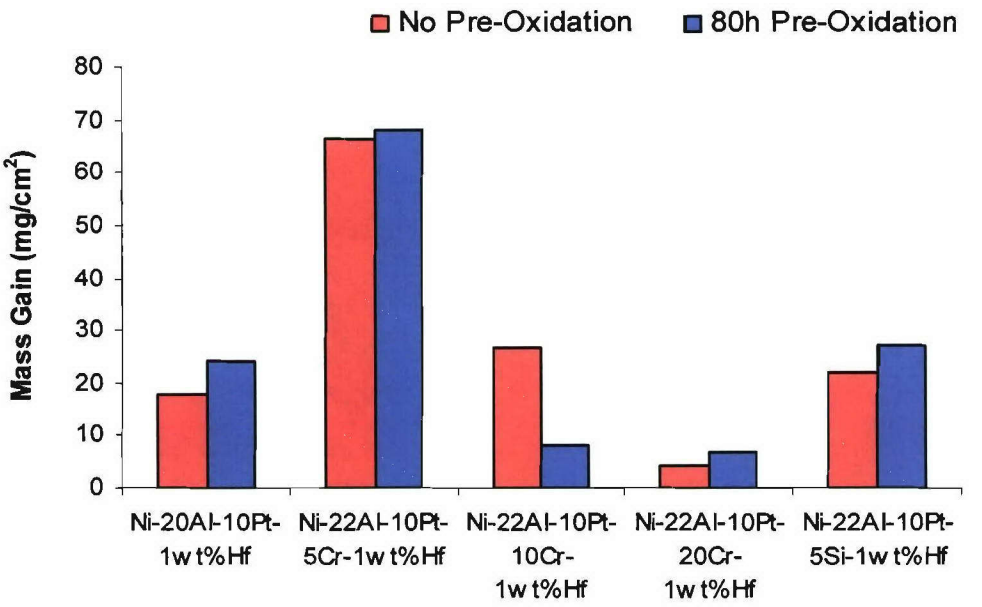

Figure 58. Effect of Cr or Si addition on the 900°C hot-corrosion resistance of $\gamma+\gamma'$ alloys containing 22 at.% Al and 10 at.% Pt.

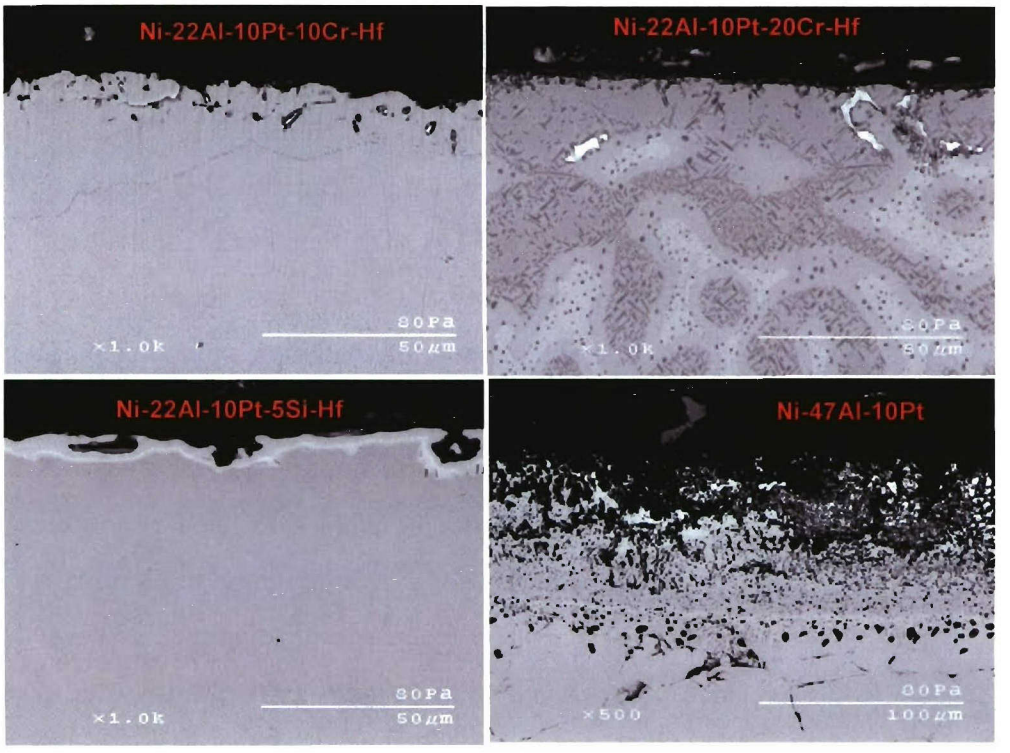

Figure 59. Cross-sectional images of various Ni-Al based alloys containing 10 at.% Pt and after a total of 100 h hot corrosion testing at 900°C.

The weight gains of Pt-modified β-NiAl and γ+β-NiCrAl alloys after HTHC testing are compared to the Pt+Cr modified γ+γ′ alloys in figure 60. Cross-sectional SEM images (*e.g.*, figure 59) revealed that the γ+γ′ alloys with Pt and/or Cr additions have comparable and even significantly better HTHC resistance than conventional β and NiCrAl alloys. The weight gains of the various Ni-22Al-5Pt-Cr-1wt%Hf (γ andγ′) alloys after 100 hours of hot-corrosion exposure at 900°C are shown in figure 61. Corresponding cross-sectional SEM images of the pre-oxidized Ni-22Al-5Pt-Cr-1wt%Hf alloys showed that various Cr-modified versions have excellent HTHC resistance. Since Cr addition was more beneficial in low-Pt containing alloys, Si + Cr were added in combination to improve HTHC resistance of Ni-22Al-5Pt-Hf containing alloy. Addition of Si was beneficial in improving HTHC resistance to a considerable amount for the non-preoxidized versions of the alloys (figure 61).

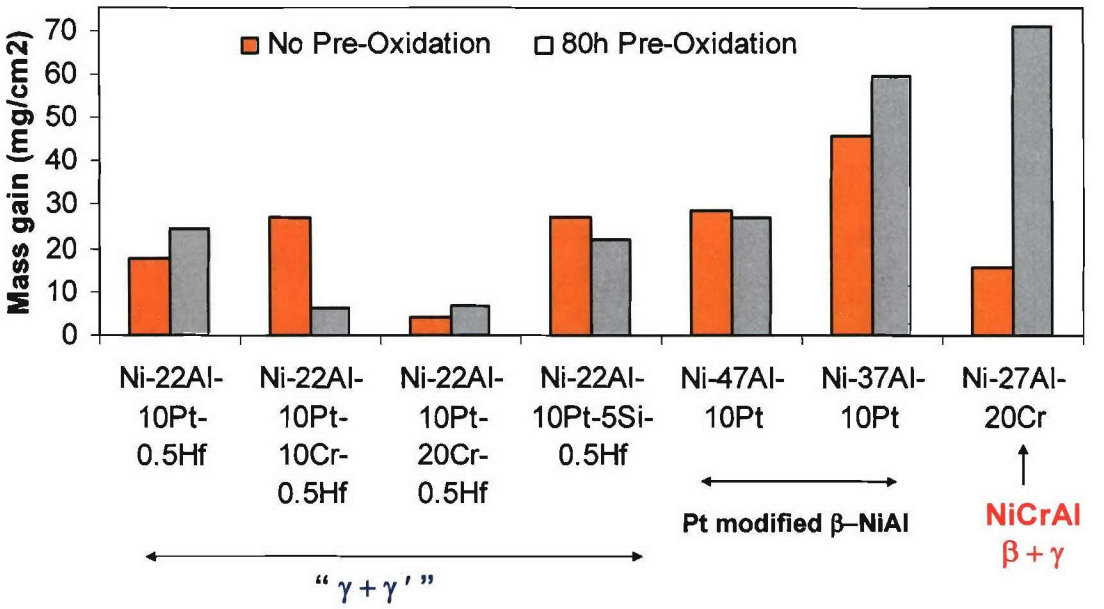

Figure 60. Comparison of weight gains of various different alloys after a total of 100 hours hot corrosion at 900°C.

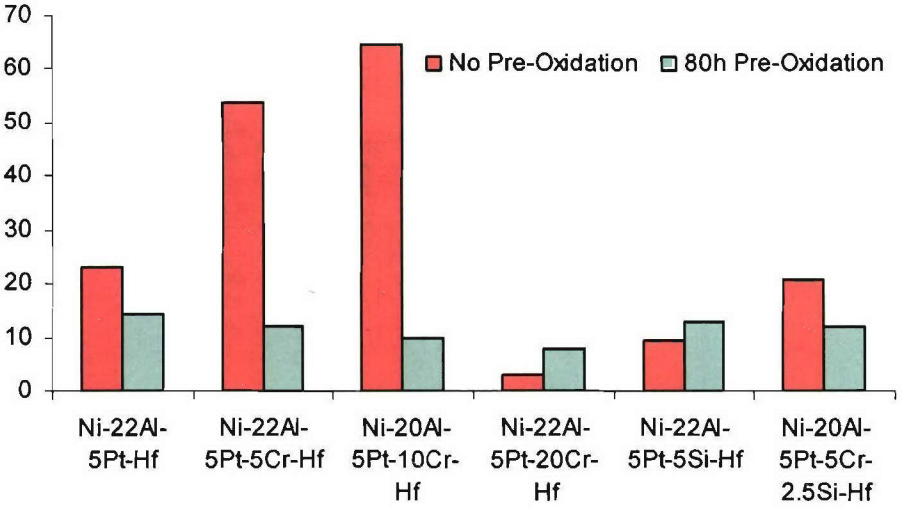

Figure 61. Effect of Cr, Si or Cr+Si addition on the 900°C hot-corrosion resistance of γ+γ′ alloys containing 22 at.% Al and 5 at.% Pt.

The weight-gain histograms of Cr modified low-Pt containing γ+γ′ alloys are compared in figure 62. It shows Cr additions are more beneficial in Ni-22Al-5Pt-Hf compared to the Ni-22Al-10Pt-Hf alloy. Weight gains and cross-sectional images confirmed that Ni-22Al-5Pt-5Cr-Hf alloy showed excellent HTHC resistance; while Ni-22Al-10Pt-5Cr-Hf alloy

underwent extensive attack (figure 63). Both the alloys formed α-Al_2O_3 after pre-oxidation but it was observed that Ni-22Al-10Pt-5Cr-Hf alloy underwent heavy spallation after 500 oxidation cycles at 1150°C while the Ni-22Al-5Pt-5Cr-Hf alloy showed excellent cyclic oxidation resistance.

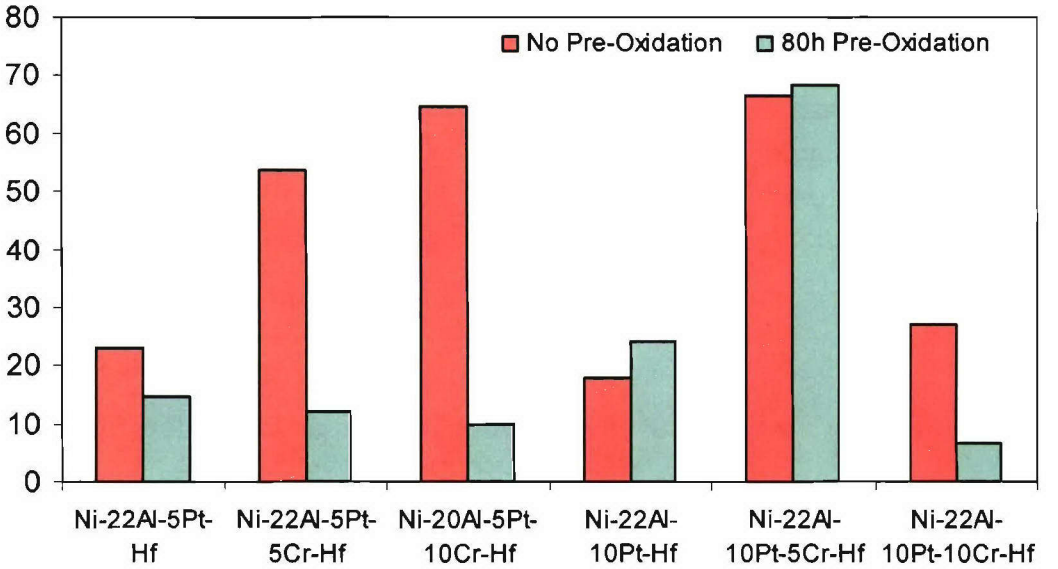

Figure 62. Comparison of the effect of Cr addition on the 900°C hot-corrosion resistance of γ+γ' alloys containing 22 at.% Al and either 5 or 10 at.% Pt.

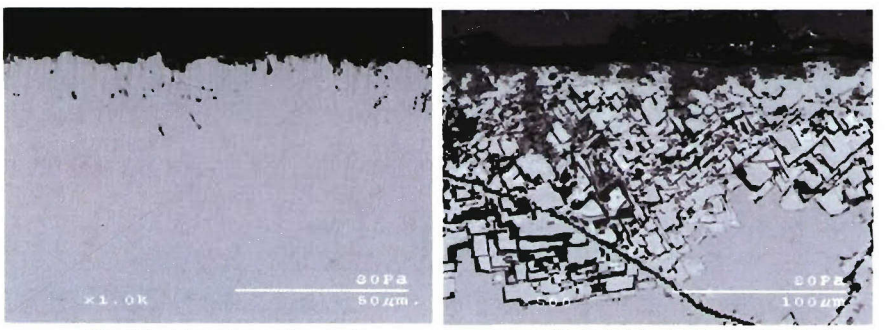

Figure 63. Cross-sectional comparison of the effect of 5 at.% Cr addition on the 900°C hot-corrosion resistance of γ+γ' alloys containing 22 at.% Al and either 5 or 10 at.% Pt.

The weight gains after 100 h of HTHC then used for calculating an attack parameter (K_{h-o}) for each alloy that was pre-oxidized. Barret [122] used a similar method to calculate cyclic-oxidation attack parameters for various alloys using the following equation:

$$\frac{\Delta W}{A} = k_1 t^{1/2} + k_2 t \pm S.E.E$$

Where k_1, and k_2 are constants analogous to the scale growth and scale spalling constants. If the data fits have $R^2>0.90$, then the attack parameter K_o is defined as:

$$K_o = (k_1 + 10|k_2|)$$

In the present case scale growth was more pronounced than spallation and hence the spalling constant (k_2) was not taken into consideration in the calculation of $K_{h\text{-}o}$. The equation used to calculate $K_{h\text{-}o}$ was therefore:

$$K_{h-o} = \left(\frac{\Delta W}{A}\right)^2 \Big/ t$$

The attack parameter results for hot corrosion are summarized in figure 64.

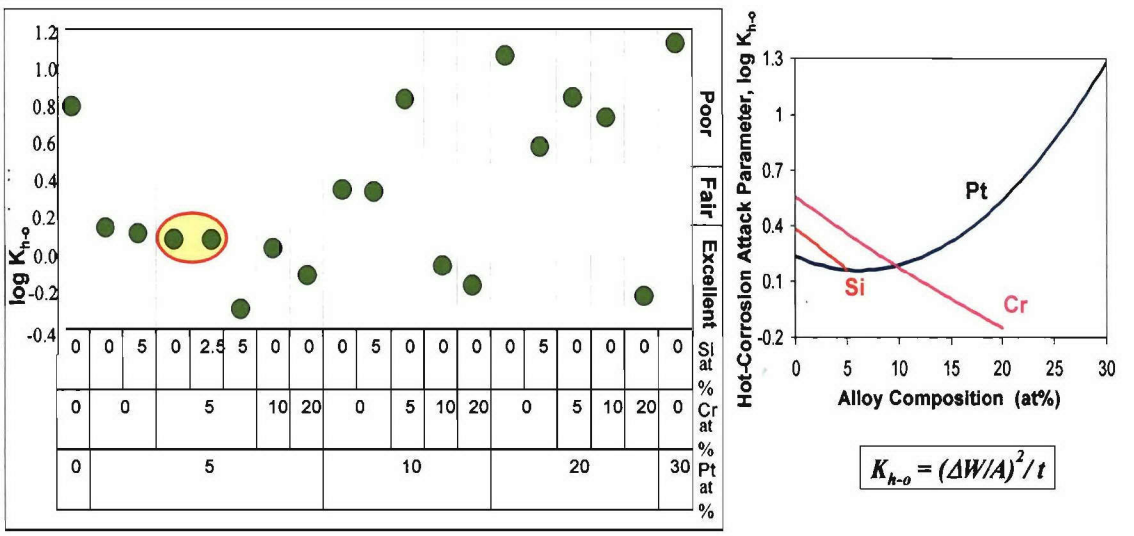

Figure 64. Calculated attack parameters for the 900°C hot-corrosion of γ+γ′ alloys containing 22 at.% Al.

4.3.2. High Temperature Oxidation (1150 °C)

Isothermal Oxidation

It has been established by our group that Pt+Hf-modified γ+γ′ alloys have extremely low oxidation rates for Al_2O_3–scale forming alloys, thereby offering viable superior alternative to the current state-of-art β-NiAl(Pt) coatings. The effect of Pt in improving oxidation resistance is compared to other alloying elements (Cr and Si) in figure 65. The Cr- or Si-modified γ+γ′ alloys underwent some scale spallation after 100 h of isothermal oxidation, while the scale on the Pt-modified was highly adherent. Cross-sectional SEM

images showed that Ni-22Al-30Pt-Hf alloy formed very thin, continuous and planar α-Al_2O_3.

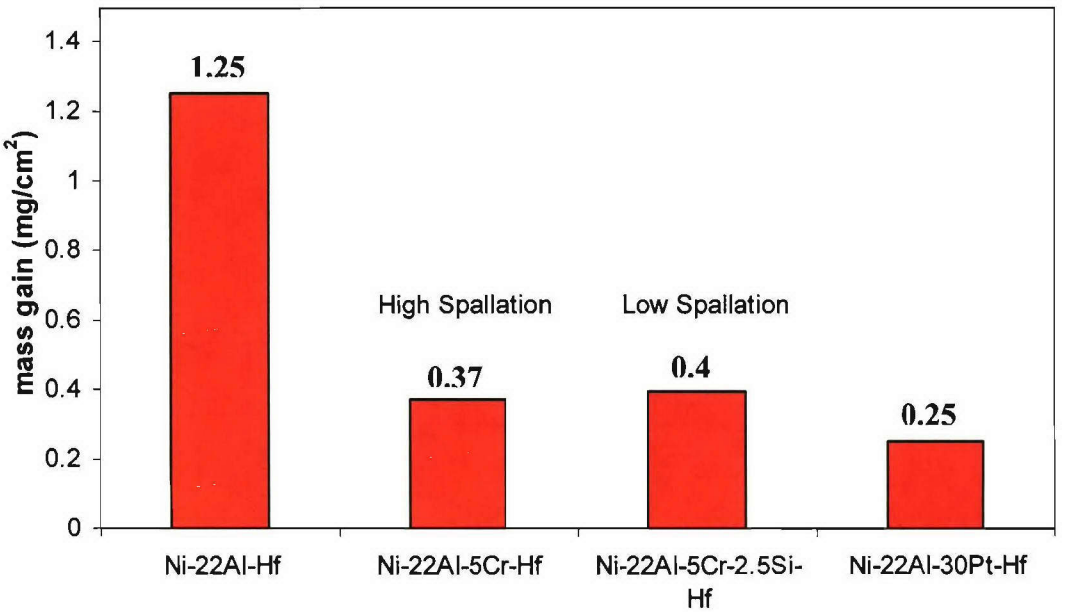

Figure 65. Comparison of the effect of Cr, Si and Pt addition on the 1150°C oxidation resistance of γ+γ′ alloys exposed to air for 100 hours and containing a fixed Al content of 22 at.% Al.

The focus of this research is to obtain alloy and coating compositions that exhibit excellent resistance to *both* HTHC and cyclic oxidation. HTHC results indicate that certain versions Cr+Si-modified Ni-22Al-5Pt-Hf alloys have excellent HTHC resistance; hence isothermal oxidation of these alloys was carried in air at 1150°C. Resulting weight gains and corresponding cross-sectional SEM images of selected alloys are shown in figures 66 and 67, respectively. Ni-22Al-5Pt-Hf alloy formed continuous scale layer consisting of an outermost layer of $NiAl_2O_4$; whereas, chromium addition to Ni-22Al-5Pt-Hf suppressed $NiAl_2O_4$ formation and promoted the exclusive formation of an α-Al_2O_3 scale layer. An Al-depletion zone of γ phase (>20 μm) was observed in the subsurface of the Ni-22Al-5Pt-Hf alloy directly beneath the scale. This zone was not observed in the Ni-22Al-5Pt-5Cr-Hf and Ni-22Al-5Pt-5Cr-2.5Si-Hf alloys, which exhibited excellent oxidation resistance (*i.e.*, the lowest weight gains). SEM images of these alloys indicated formation of thin, planar α-Al_2O_3 scale.

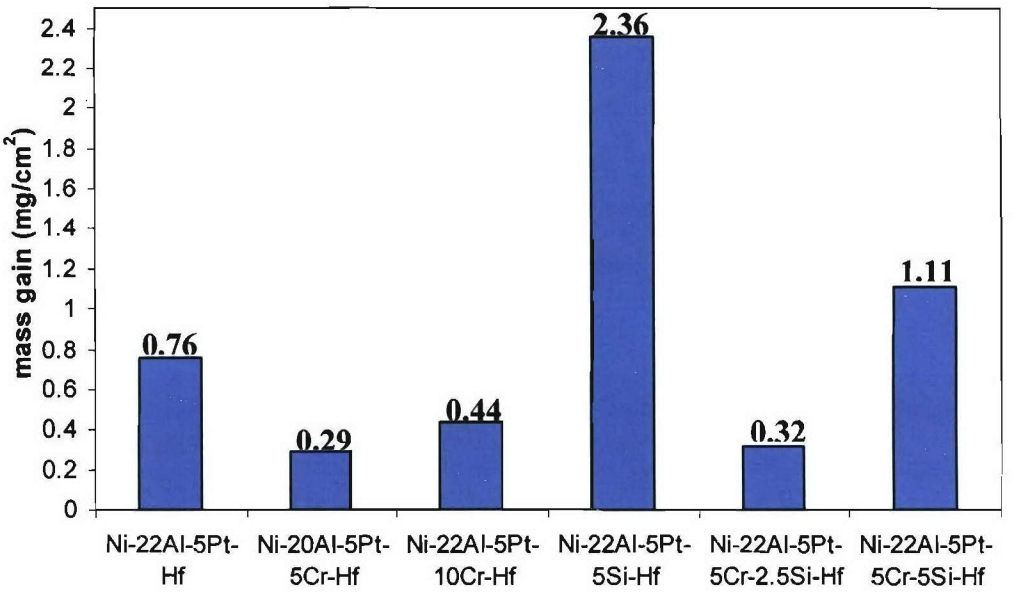

Figure 66. Comparison of the effect of Cr, Si and Cr+Si addition on the 1150°C oxidation resistance of γ+γ′ alloys exposed to air for 100 hours and containing a fixed Al content of 22 at.% Al and Pt content of 5 at.%.

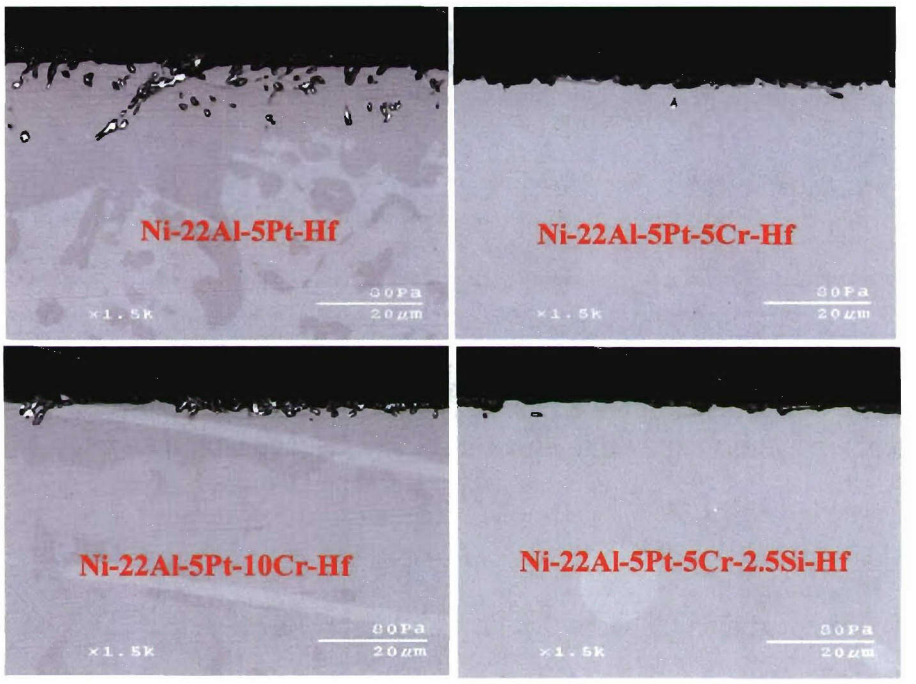

Figure 67. Corresponding (figure 66) cross-sectional SEM images.

It was found that Cr/Si addition was also beneficial in improving HTHC resistance of Ni-22Al-10Pt-Hf containing alloy. In fact, certain versions Cr/Si-modified Ni-22Al-10Pt-Hf

alloy had excellent HTHC resistance. The weight gains of the Ni-22Al-10Pt-Cr/Si-Hf alloys after 100 hours isothermal oxidation at 1150°C in air are shown in figure 68. Scale spallation was observed with 5at% Cr addition but not for 10at% Cr addition. Ni-22Al-10Pt-20Cr-Hf with higher Cr addition showed poor oxidation resistance. 5 at.% Si addition improved oxidation resistance considerably, resulting in the lowest apparent weight gain. SEM imaging of Ni-22Al-10Pt-Hf revealed a subsurface Al-depletion zone of γ below the scale. The thickness of this zone generally decreased with increasing Pt addition to the Ni-22Al-Pt-Hf alloys. Chromium addition (up to 10at %) considerably decreased the presence of this zone in Ni-22Al-10Pt-Cr-Hf alloys. And the zone was completely absent in the Si-containing alloy, which formed very thin Al_2O_3 scale.

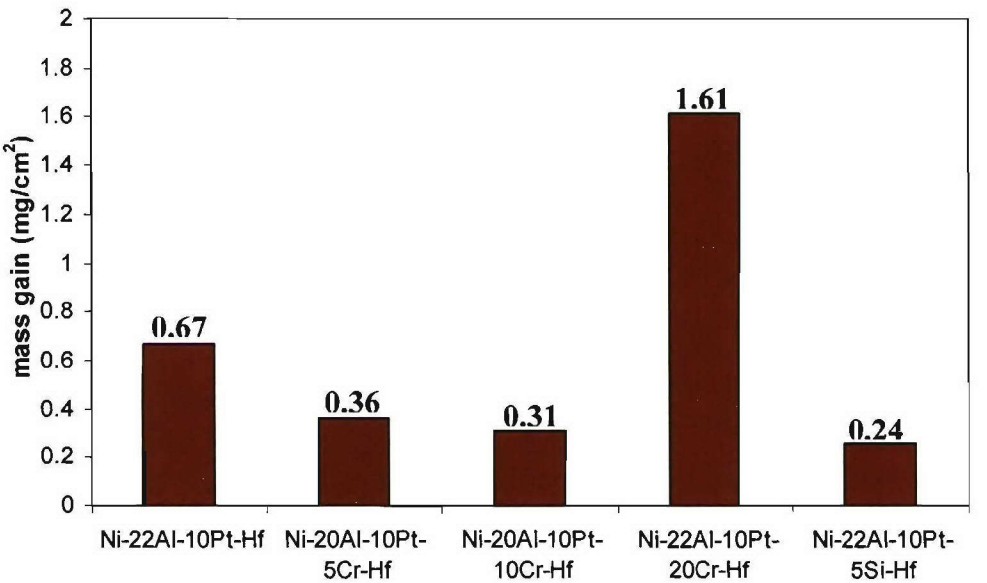

Figure 68. Comparison of the effect of Cr and Si addition on the 1150°C oxidation resistance of $\gamma+\gamma'$ alloys exposed to air for 100 hours and containing a fixed Al content of 22 at.% Al and Pt content of 10 at.%.

Cyclic Oxidation

The results presented thus far show that Cr addition to "low Pt" Ni-22Al-5/10Pt-Hf alloys have is highly beneficial to both HTHC and isothermal oxidation resistance. The cyclic oxidation kinetics of Pt+Cr-modified $\gamma+\gamma'$ alloys is shown in figure 69. The cyclic oxidation behavior of the established, oxidation-resistant Ni-22Al-30Pt-Hf and a Pt-modified β-NiAl (Ni-50Al-15Pt) alloys is included in this figure for comparison. It is seen that the Pt+Hf-modified $\gamma+\gamma'$ alloys showed positive weight gain kinetics with no

indication of spallation throughout the 500 one-hour thermal cycles. Further, the amount of weight gain decreased with increasing Pt content from 5 to 30at %. The Ni-22Al-5Pt-Hf alloy exhibited good oxidation resistance that was comparable to the Pt-modified β-NiAl. Addition of Cr without Pt in γ+γ′ alloys showed spallation just after 60 cycles, suggesting that Pt improves scale adhesion in the γ+γ′ alloys. Pt+Cr-modified γ+γ′ alloys (Ni-22Al-5Pt-5Cr-Hf and Ni-22Al-10Pt-10Cr-Hf) showed excellent oxidation resistance after 500 cycles. In fact, the Ni-22Al-5Pt-5Cr-Hf alloy showed the lowest weight gain of 0.39 mg/cm^2 after 500 cycles. Ni-22Al-10Pt-10Cr-Hf alloy showed a little spallation but overall had excellent oxidation resistance. Addition of higher Cr (10at%) to Ni-22Al-5Pt-Hf increased the weight gain, but it was still comparable to the Pt-modified β-NiAl. XRD analysis showed the presence of α-Al_2O_3 scale formation on all alloys except for Ni-22Al-5Pt-Hf. The latter showed $NiAl_2O_4$ along with α-Al_2O_3. Figure 70 shows corresponding cross-sectional SEM images of the set of Ni-22Al-Pt-Cr-Hf alloys. A subsurface γ-Ni Al-depletion zone was observed in the Ni-22Al-5Pt-Hf alloy, which had also formed a duplex scale structure comprised from outside-to-inside of $NiAl_2O_4$ and Al_2O_3. The Ni-22Al-5Pt-5Cr-Hf and Ni-22Al-10Pt-10Cr-Hf alloys formed very thin, continuous Al_2O_3 scale. A very thin subsurface γ-Ni was observed in Ni-22Al-10Pt-10Cr-Hf alloy. The Ni-22Al-5Pt-10Cr-Hf alloy formed thicker Al_2O_3 scale with higher percentage of HfO_2 formation. Higher Cr addition apparently increased the chemical activity of hafnium, $a_{Hf,}$ in the alloy, which in turn promoted a greater amount of HfO_2 formation in the alloy. The Ni-22Al-5Cr-Hf alloy formed a discontinuous Al_2O_3 scale.

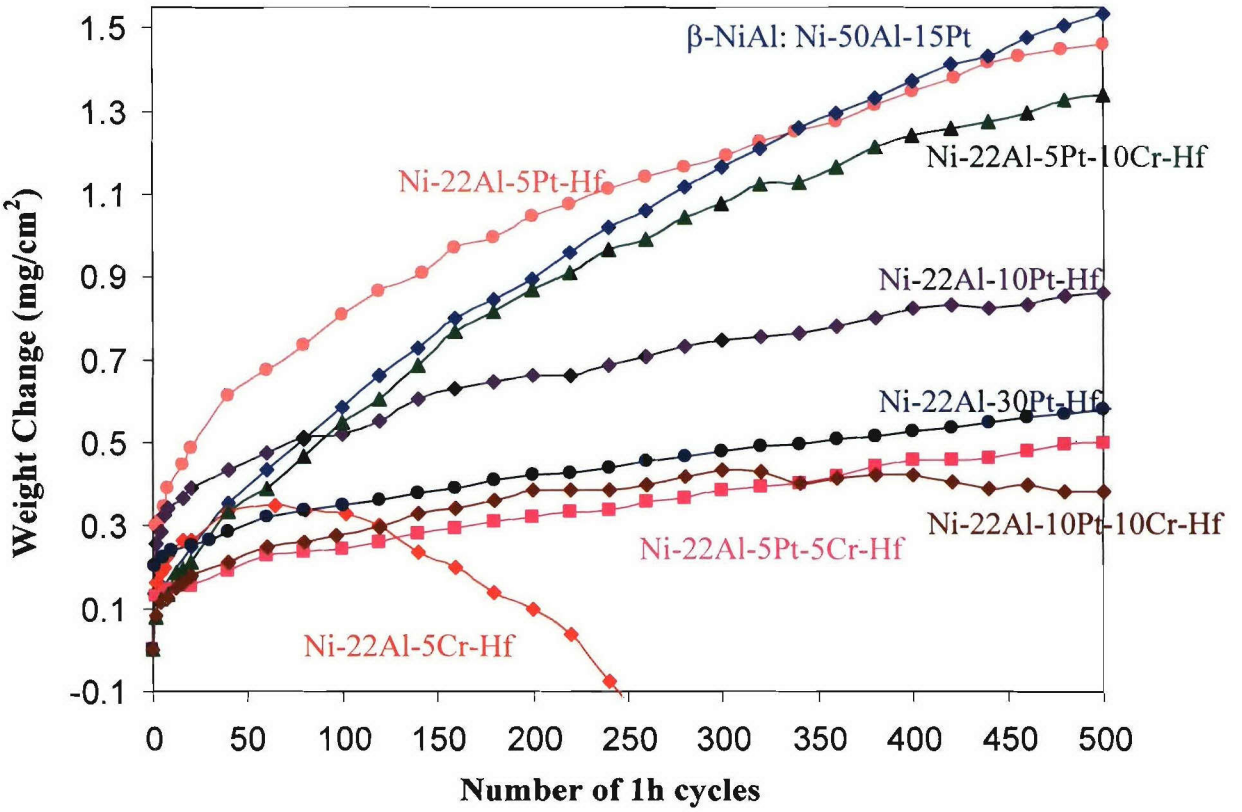

Figure 69. Cyclic oxidation kinitics at 1150°C in air.

Cyclic oxidation weight gain kinetics of Si+Pt-modified γ+γ′ alloys are shown in figure 71. Silicon addition to the Ni-22Al-10Pt-Hf alloy considerably reduced the initial-term oxidation kinetics and in turn reduced the overall weight gain. A similar trend was seen for Si addition to Ni-22Al-20Pt-Hf alloy. The lowest weight gain of 0.36mg/cm^2 was observed for Ni-22Al-20Pt-5Si-Hf in various modified γ+γ′ alloys tested under this project. The combined effect of Cr+Si was studied in low-Pt (5at%) γ+γ′ alloys. Si addition in the Ni-22Al-5Pt-5Cr-Hf alloy further improved its oxidation resistance (figure 72). It is recalled that the Ni-22Al-5Pt-5Cr-Hf and Ni-22Al-5Pt-5Cr-2.5Si-Hf alloys also exhibited excellent HTHC resistance. The effect of Cr+Si addition without Pt addition was also studied and spallation was observed in Ni-22Al-5Cr-2.5Si-Hf as shown in figure 72. Corresponding cross-sectional SEM images of the modified γ+γ′ alloys are shown in

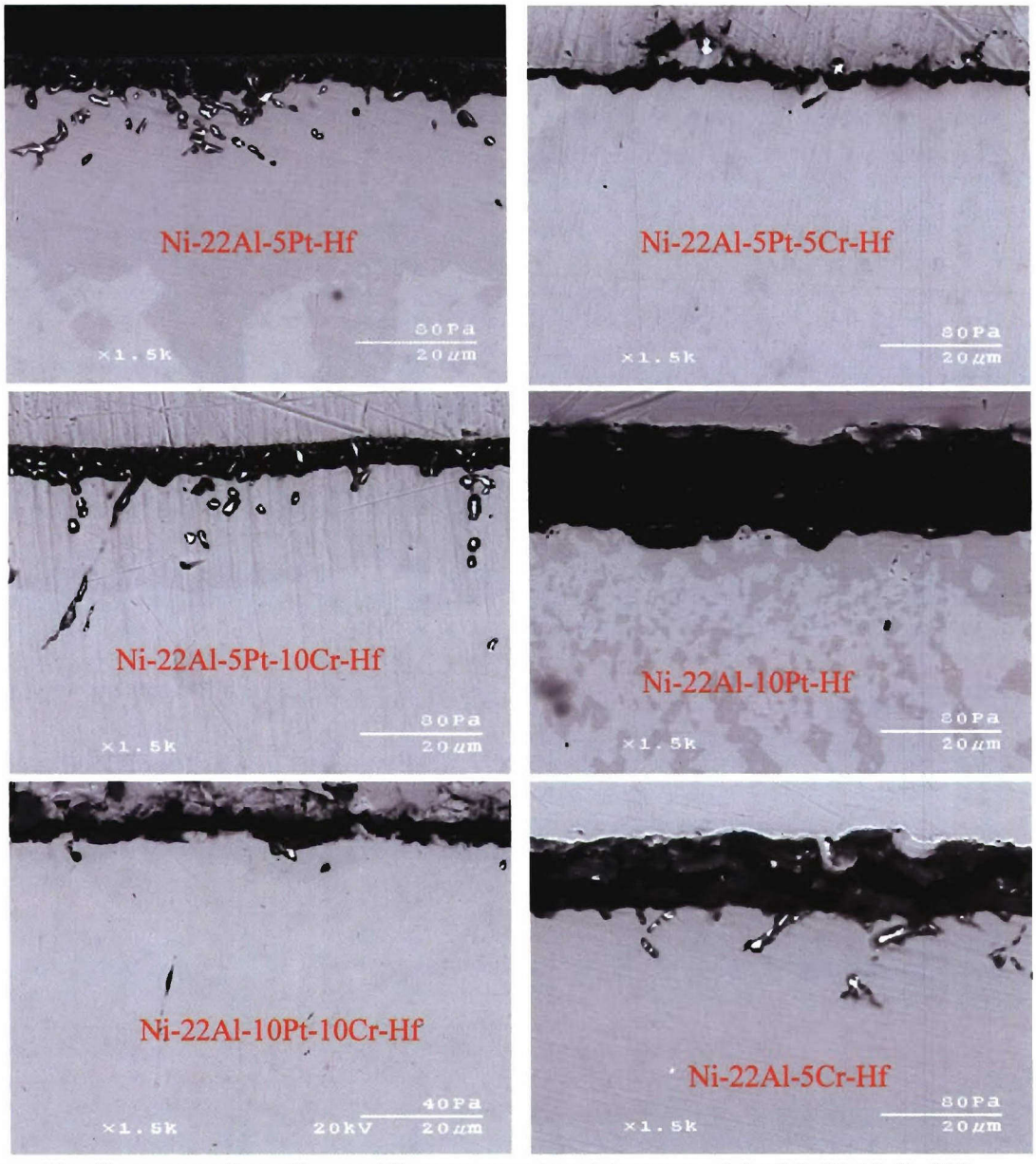

Figure 70. Corresponding (figure 69) cross-sectional images of the Ni-22Al-Cr-Hf alloys after 500 one-hour cycles at 1150°C in air.

figure 73. Si+Pt modified γ+γ′ alloys formed very thin continuous α-Al_2O_3 scale. The scales on these alloys did not did not show any evidence of HfO_2 formation, which may be related to the reduced initial-stage oxidation kinetics of these alloys. The Ni-22Al-5Pt-5Cr-2.5Si-Hf alloy also formed thin continuous α-Al_2O_3 scale.

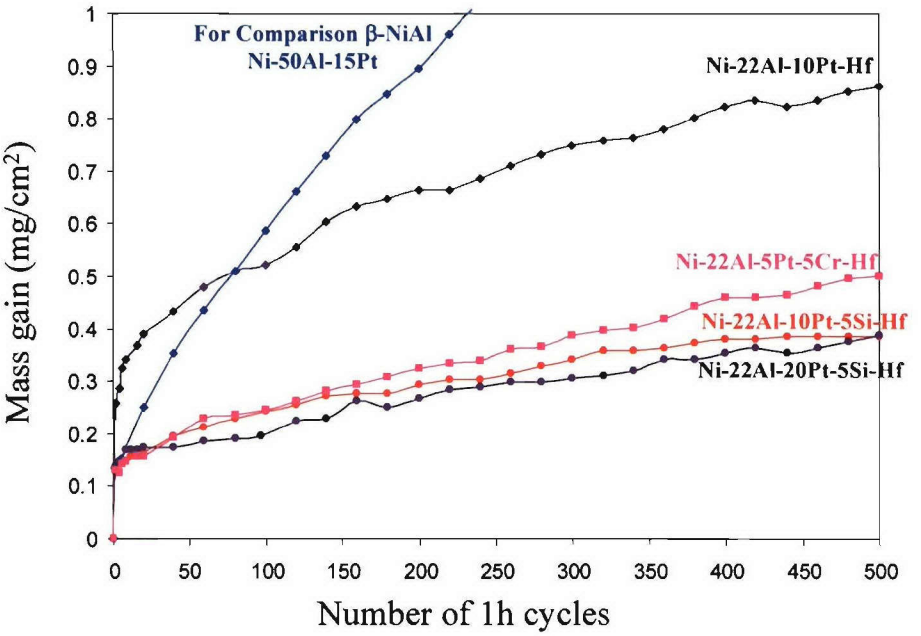

Figure 71. Effect of Cr and Si on cyclic oxidation kinitics at 1150°C in air.

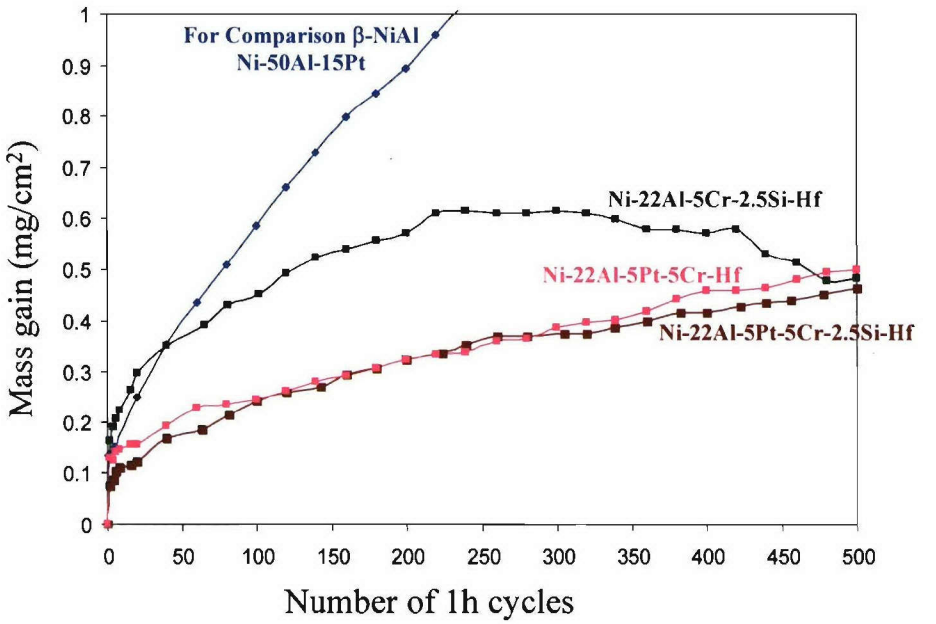

Figure 72. Effect of Cr and Cr+Si on cyclic oxidation kinitics at 1150°C in air.

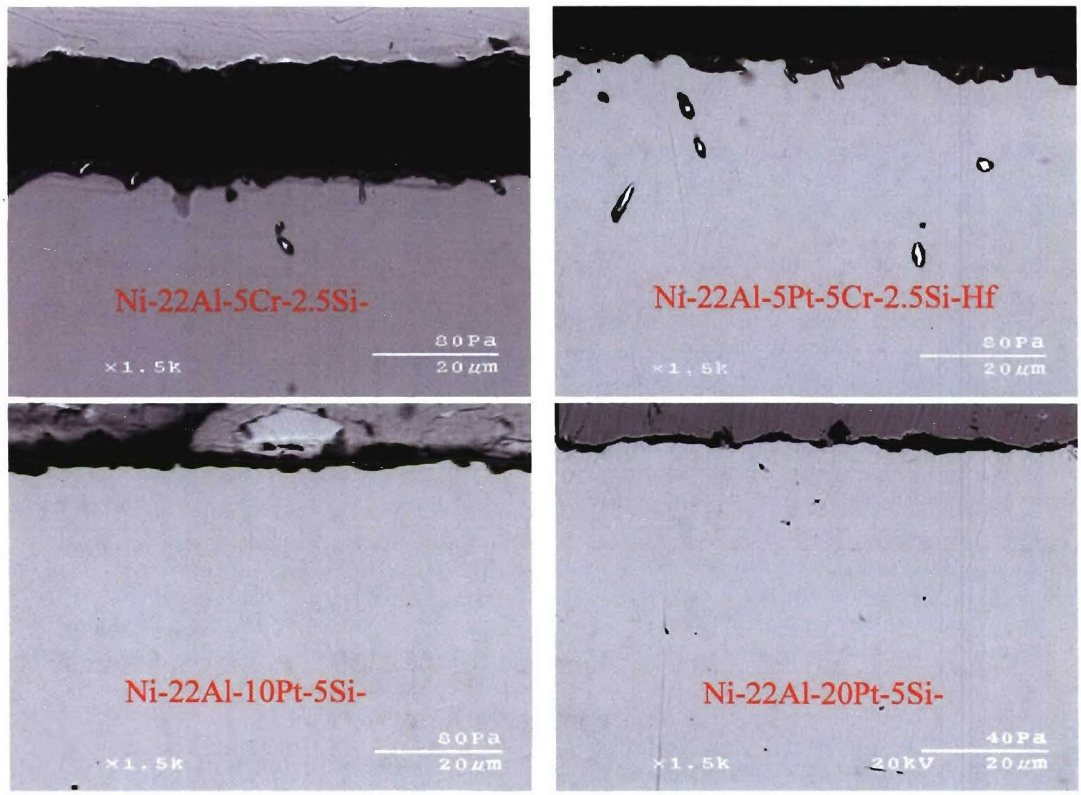

Figure 73. Corresponding cross-sectional SEM images of the modified γ+γ′ alloys after 500 one-hour oxidation cycles at 1150°C in air.

The cyclic oxidation weight gains obtained were used for calculating an oxidation attack parameter (K_o) for each alloy using following equation:

$$\frac{\Delta W}{A} = k_1 t^{1/2} + k_2 t \pm S.E.E$$

Where k_1, and k_2 are constants analogous to the scale growth and scale spalling constants. If the data fits have $R^2 > 0.90$, then the attack parameter K_o is defined as:

$$K_o = (k_1 + 10|k_2|)$$

The results from the K_o determinations are summarized in figure 74. Assessing the statistical analyses of hot corrosion (figure 64) and oxidation attack (figure 74) parameters it is inferred that the optimized coating composition is Ni-22Al-5Pt-5Cr-(0-2.5)Si-1 wt.%Hf.

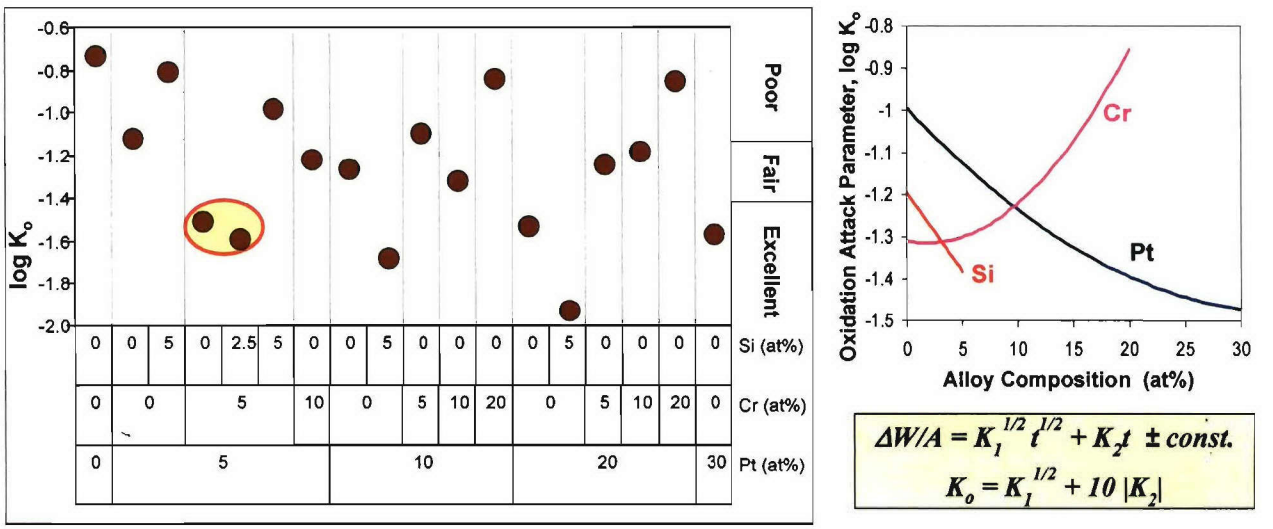

Figure 74. Calculated attack parameters for the 1150°C cyclic oxidation of γ+γ′ alloys containing 22 at.% Al.

4.3.3. Summary and Conclusions

1. Addition of low Pt (up to 10 at %) to γ + γ′ alloys improved HTHC resistance but did not help in higher Pt-containing alloys. This is because platinum decreases a_{Al} and increases a_{Ni} to the extent that Ni_3S_2, which is liquid above about 787°C, forms in preference to Al_2S_3 with increasing Pt content.

2. Chromium was beneficial in further improving HTHC resistance of Pt-modified γ + γ′ alloys. In low Pt (up to 10 at %) γ + γ′ alloys, the present results suggest that addition of Cr should be either equal to or greater than Pt content for optimum HTHC resistance. Alloys with lower Cr content, *e.g.*, Ni-22Al-10Pt-5Cr-Hf, Ni-22Al-20Pt-5Cr-Hf and Ni-22Al-20Pt-10Cr-Hf showed spallation even after pre-oxidation and did not exhibit good HTHC resistance.

3. Pre-oxidation of Ni-22Al-10Pt-10Cr-Hf, Ni-22Al-5Pt-10Cr-Hf, Ni-22Al-5Pt-5Cr, and Ni-22Al-10Pt-5Si γ + γ′ alloys resulted in the formation of a compact, planar and adherent Al_2O_3 scale, which prevented these alloys from HTHC attack. These alloys also possessed improved oxidation resistance than the Ni-22Al-10Pt-Hf alloy. Ni-

22Al-10Pt-10Cr-Hf and Ni-22Al-20Pt-5Si-Hf have the excellent cyclic oxidation resistance, comparable to the Ni-22Al-30Pt-Hf alloy.

4. Higher Cr-containing (20 at %) alloys with varying Pt content (5-20 at %), *e.g.*, Ni-22Al-5Pt-20Cr-Hf, Ni-22Al-10Pt-20Cr-Hf, Ni-22Al-20Pt-20Cr-Hf gave the best performance of the alloys not given a pre-oxidation treatment. These alloys showed excellent HTHC resistance, better than Pt-modified β and MCrAlY alloys, but oxidation resistance of these alloys is rather poor.
5. Silicon addition also improved the HTHC resistance of Pt-modified γ + γ′ alloys, but Si addition above 5 at% formed a brittle phase with a melting point of about 1165°C. Silicon-containing alloys also showed excellent oxidation resistance, even better than Cr+Pt modified γ + γ′ alloys.

4.4 Hot Corrosion and Oxidation Behavior of a Novel Pt+Hf-Modified γ-Ni+γ'-Ni_3Al-Based Coating

There has been considerable progress in studying the oxidation behavior of Pt-modified γ'+γ coatings [33, 104]; however, hot corrosion behavior of such coatings has never been reported. In this study, cyclic oxidation and hot corrosion resistance of a diffusion-based Pt+Hf-modified γ'+γ coating are reported and compared with commercially used Pt-modified β and γ+β-CoCrAlY coatings. The above as-deposited coatings are shown in figure 75.

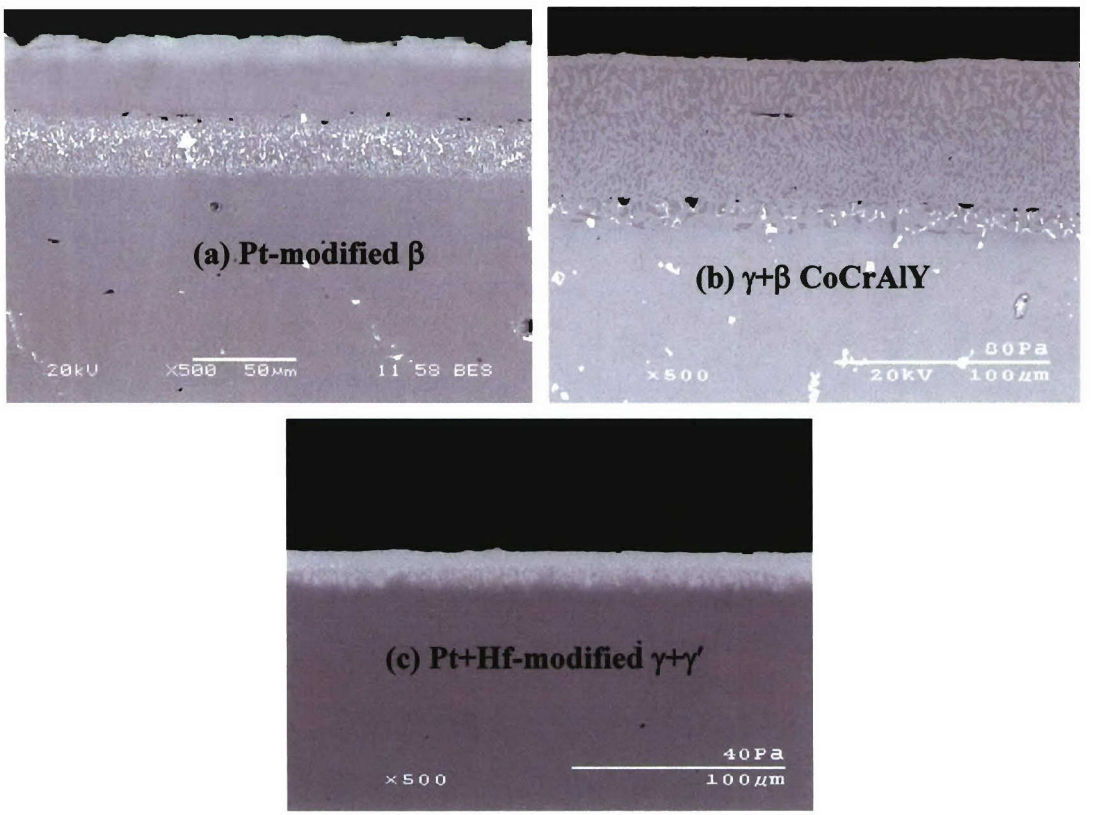

Figure 75. Cross-sectional SEM images of as-deposited (a) Pt-modified β (b) γ + β-CoCrAlY (c) Pt+Hf-modified γ'+γ coatings.

Figure 76 shows cross-sectional SEM micrographs of the Pt+Hf-modified γ'+γ and Pt-modified β coatings after a total of 1000h cyclic oxidation in air. Both coatings formed a continuous and adherent TGO scale, and there was no visual evidence of scale

spallation after thermal cycling. XRD analysis performed on these coatings confirmed that both coatings were indeed Al_2O_3-formers. The thickness of the TGO scale was also similar for the two coatings; however, the Pt-modified β coating, which was planar at the start of the testing, underwent unwanted significant surface undulations after thermal cycling.

A recent oxidation study on γ'+γ bulk alloys by Izumi and Gleeson [14] reported a much lower steady-state parabolic rate, k_p, for a Pt+Hf-modified γ'+γ alloy of composition (in at%) Ni-20Al-20Pt-0.35Hf ($k_p = 6.5\times10^{-14}$ $g^2/cm^4 s$) than a model Pt-modified β alloy of composition (in at%) Ni-50Al-15Pt ($k_p = 1.2\times10^{-12}$ $g^2/cm^4 s$). Cyclic and isothermal oxidation results suggest that the TGO scales formed on the Pt+Hf-modified γ'+γ coatings and bulk alloys are more protective than those formed on the Pt-modified β alloys and coatings. This may be attributable to the additions of Pt and Hf and the absence of rumpling in the case of the γ'+γ coating. XRD analysis was performed on the pre-oxidized coatings prepared for hot corrosion testing. All coatings indicated the formation of an α-Al_2O_3 scale after the pre-oxidation treatment. Although the CoCrAlY coating formed Al_2O_3 scale, it also developed localized regions of Ni-rich oxide after pre-oxidizing treatment, indicating its inferior oxidation resistance.

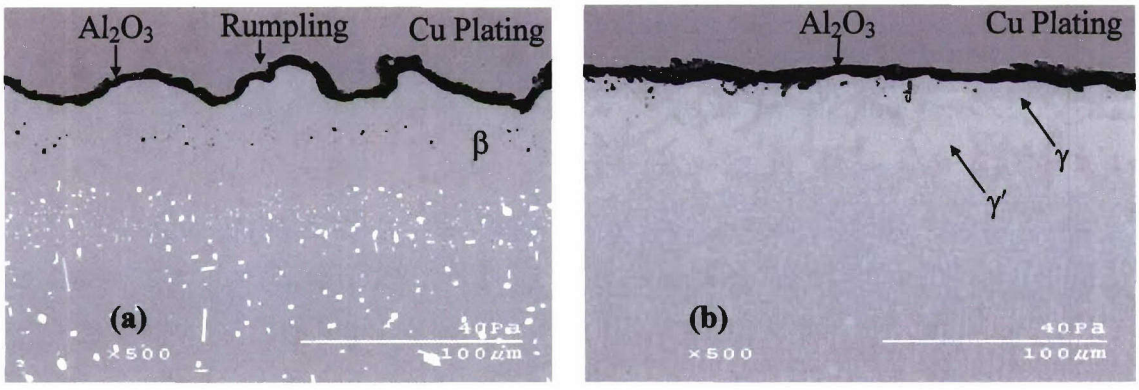

Figure 76. Cross-sectional SEM micrographs of (a) Pt-modified β (b) Pt+Hf-modified γ'+γ coatings after 1000h of cyclic oxidation testing at 1150°C.

SEM micrographs of pre-oxidized Pt-modified β, γ+β-CoCrAlY, and Pt+Hf-modified γ'+γ coatings, after 200 hours Type I hot corrosion, are shown in figure 77 (a-c). It was

found that Pt-modified β coating was completely attacked; while the CoCrAlY and Pt+Hf-modified γ′+γ coatings were only marginally attacked; although, some attack involving nickel sulfide formation (as determined by EDS) was initiated at the edges of this latter coating. Type I hot corrosion testing was further carried out to a total of 100h of exposure. The CoCrAlY and Pt+Hf-modified γ′+γ coatings exhibited excellent Type I hot corrosion resistance, while a considerable amount of attack was observed in the Pt-modified β coating. The Pt+Hf-modified γ′+γ coating in particular showed very little Type I hot corrosion attack. Hot corrosion attack of the Pt-modified β coating was initiated and then propagated from the specimen edges; approximately 50% of the exposed area was attacked after 100h of exposure (figure 78). EDS analysis indicated the formation of Ni, Cr, and Al sulfides in the attacked region, with a particularly high percentage of nickel sulfide formation at the corrosion front.

The excellent performance of the Pt+Hf-modified γ′+γ coating is attributable to the presence of a protective α-Al_2O_3 scale after the pre-oxidation treatment. The cyclic and isothermal oxidation results of Pt+Hf-modified γ′+γ and Pt-modified β indicated that the α-Al_2O_3 scale formed on the former is more protective. Further, chromium is known to be beneficial in improving the hot corrosion resistance of Ni-based alloys and coatings [70]. A higher percentage of Cr is contained in the starting composition of the Pt+Hf-modified γ′+γ coating (~ 7at%) compared to the Pt-modified β coating (~ 2at%).

To better understand Type I hot corrosion behavior of Pt+Hf-modified γ′+γ and Pt-modified β, an additional set of experiments were carried out using cast (in at%) Ni-47Al-10Pt and Ni-37Al-10Pt β alloys, and a Ni-22Al-20Pt-10Cr-0.35Hf γ′+γ alloy. Figure 79 shows SEM micrographs of these alloys after 100h of exposure under Type I conditions at 900°C. It is seen that the Ni-47Al-10Pt β alloy showed resistance comparable to the γ′+γ alloy; however, as the Al content in β decreased (Ni-37Al-10Pt), the hot corrosion resistance decreased as well. This suggests that hot corrosion resistance in Pt-modified β is highly sensitive to Al content. The practical relevance of this is that Al depletion from a Pt-modified β coating will indeed occur during service due to coating-substrate interdiffusion and, hence, the hot corrosion of the coating will

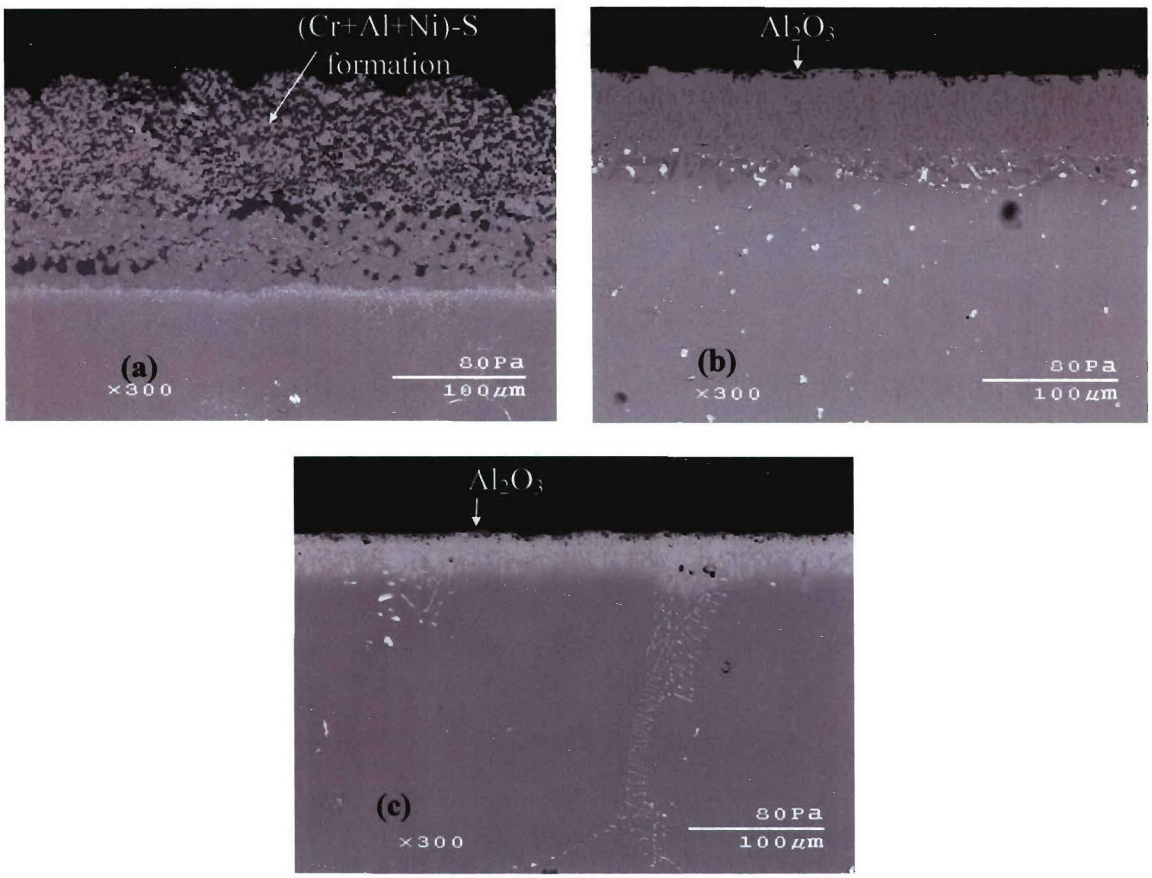

Figure 77. Cross-sectional SEM images of (a) Pt-modified β (b) γ + β-CoCrAlY (c) Pt+Hf-modified γ′+γ coatings after 200h of Type I hot corrosion testing at 900°C.

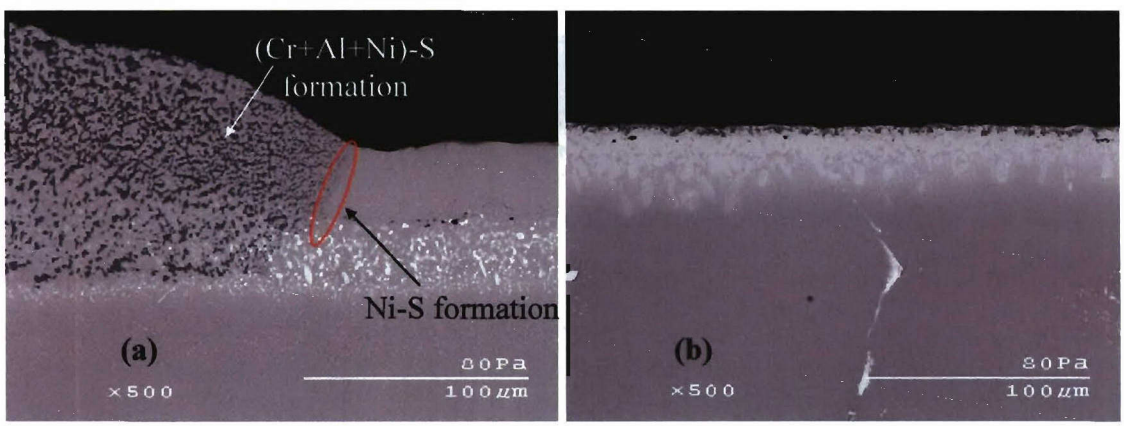

Figure 78. Cross-sectional SEM images of (a) Pt-modified β (b) Pt+Hf-modified γ′+γ coatings after 100h of Type I hot corrosion testing at 900°C.

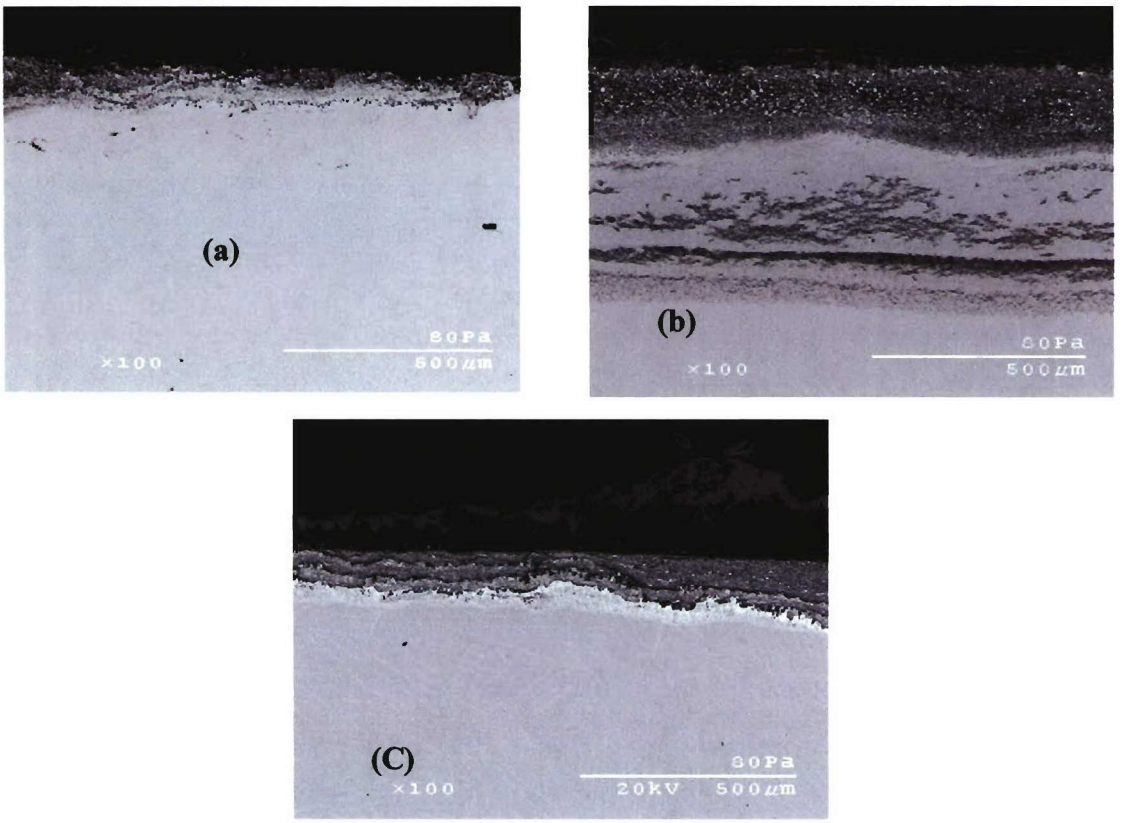

Figure 79. SEM images of (a) Ni-47Al-10Pt (b) Ni-37Al-10Pt (c) Ni-22Al-10Pt-10Cr-0.35Hf alloys (all in at%) after 100h of Type I hot corrosion testing at 900°C.

progressively decrease. By contrast, a similar Al depletion due to coating-substrate interdiffusion is not expected for the case of Pt+Hf-modified γ′+γ coatings. For instance, a diffusion study by Hayashi *et al.* [123] on Pt+Hf-modified γ′+γ alloys reported that Al uphill diffusion from substrate to the coating can occur for Pt+Hf-modified γ′+γ coatings.

Cross-sectional micrographs of the Pt-modified β, γ + β-CoCrAlY (mid-chord section), and Pt+Hf-modified γ′ + γ coatings after 100 hours of Type II hot corrosion are shown in figure 80(a-c). From these micrographs it is evident that the CoCrAlY coating was attacked while the Pt-modified β and Pt+Hf-modified γ′ + γ coatings showed excellent Type II hot corrosion resistance. The poor performance of CoCrAlY coatings in Type II conditions is attributed to the formation of Na_2SO_4-$CoSO_4$ eutectic (T_{melt} = 565°C) [49-52]. Co-based alloys and coatings are more susceptible to Type II hot corrosion attack than the Ni-based alloys and coatings because $CoSO_4$ is more stable than

$NiSO_4$. As a consequence, $CoSO_4$ can form at a lower P_{SO_3} than $NiSO_4$. Visual observations of these coatings confirmed that the salt was indeed in liquid state on the CoCrAlY coating just after 60h of testing, while it was in solid state on the Pt-modified β, and Pt+Hf-modified γ′ + γ coatings even after 100h of testing. A further contributing factor to the liquid formation on to CoCrAlY coating may be the fact that this coating formed less protective TGO scale than those formed on the Pt-modified β and Pt+H-modified γ′ + γ coatings.

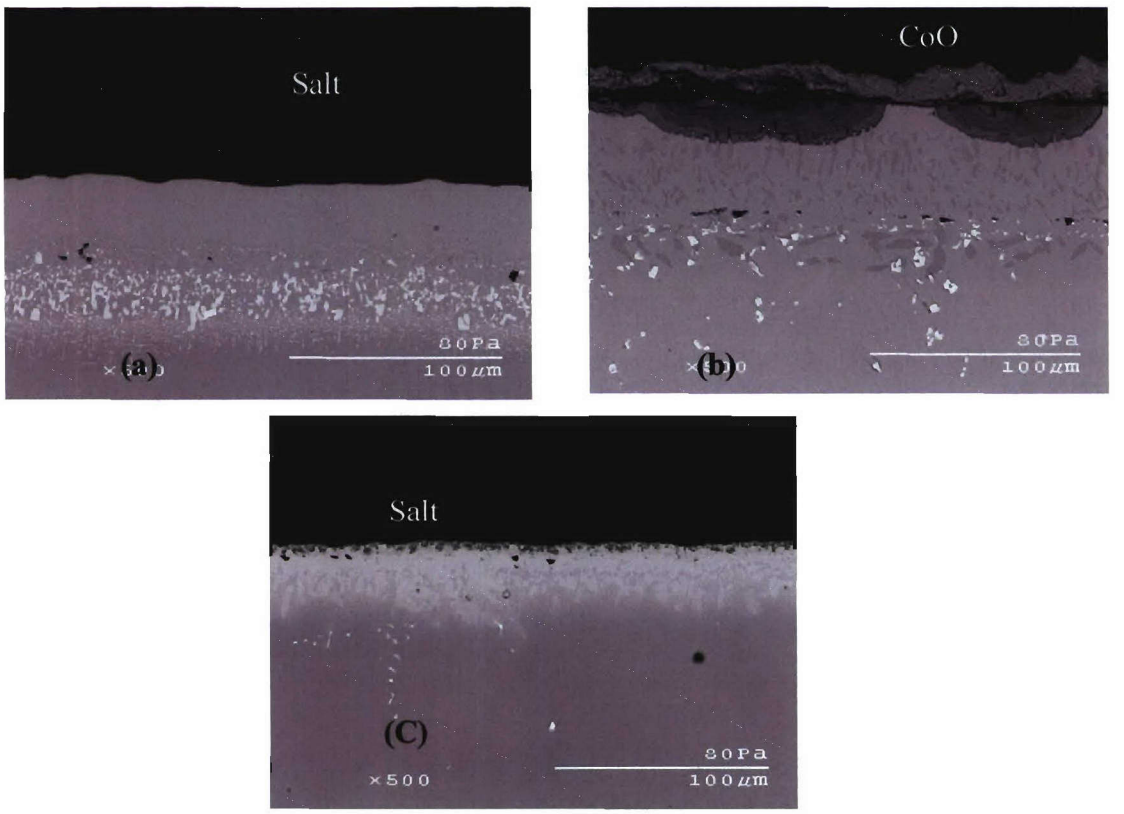

Figure 80. Cross-sectional SEM micrographs of (a) Pt-modified β (b) γ + β-CoCrAlY (c) Pt+Hf-modified γ′+γ coatings after 100h of Type II hot corrosion testing at 705°C.

Summary and Conclusions

The Pt+Hf-modified γ′-Ni_3Al + γ-Ni coatings developed here at ISU outperformed state-of-the-art commercial β-(Ni,Pt)Al and γ+β-CoCrAlY coatings from the standpoint of combined resistance to cyclic oxidation and both types of hot corrosion. The Pt+Hf-

modified $\gamma'+\gamma$ coatings formed a planar, adherent alumina scale; while rumpling was observed for Pt-modified β after thermal cycling. The Pt+Hf-modified $\gamma'+\gamma$ and the commercial $\gamma+\beta$-CoCrAlY coatings exhibited excellent Type I hot corrosion resistance; whereas, while under Type II conditions, the $\gamma'+\gamma$ and commercial β coatings showed excellent resistance. The hot corrosion performance of the Pt+Hf-modified $\gamma' + \gamma$ coating under Type I and II conditions is believed to be attributable to its ability to form a highly adherent and compositional uniform α-Al_2O_3 scale. The overall ranking of coating performance against oxidation and hot corrosion from the best to worst was as follows: Pt+Hf-modified γ'-Ni_3Al + γ-Ni > Pt-modified β-NiAl > $\gamma+\beta$-CoCrAlY. Even with the very encouraging results obtained to date, it is believed further improvements in the hot-corrosion resistance of the $\gamma+\gamma'$ coatings is both necessary and tractable. Moreover, present results have shown that much further optimization in the combined resistance of the $\gamma+\gamma'$ coatings to both hot corrosion and cyclic oxidation is achievable by depositing low-Pt (i.e., 5-10 at.%) compositions judiciously modified with Cr and Hf. A foundation for valuable future work has been established from the results and analyses of thy study.

5. REFERENCES

1. B. Gleeson, W. Wang, S. Hayashi, and D. Sordelet, Mater. Sci. Forum, 461-464, (2004), 213.
2. F.S. Pettit and G.H. Meier, Superalloys 1984, Metallurgical Society of AIME, Warrendale, PA, 651-87, (1984).
3. F.S. Pettit and G.W. Goward, Applied Science Publishers, (1983).
4. N. Eliaz, G. Shemesh, R.M. Latanision, Engineering Failure Analysis, 9, (2002), 31-43.
5. G.W. Goward, 30th International Gas Turbine Conference and Exhibit, Paper No. 85-GT-60, ASME, (1985).
6. Y. Tamarin, "Protective Coatings for Turbine Blades," ASM International, (2002).
7. N.P. Padture, M Gell, and E.H. Jordan, Science, Vol. 296, (2002), 280.
8. U. Schulz, C. Leyens, K. Fritscher, M. Peters, B. Saruhan-Brings, O. Lavigne, Jean-Marc Dorvaux, M. Poulain, R. Mevrel, Aerospace Science and Technology 7, (2003), 73-80.
9. A.S. Radcliff, Mater. Sci. Technol., Vol. 3, (1987), 554.
10. J.R. Strife and J.E. Sheehan, Ceramic Bulletin, 67, (1988), 369-374.
11. J.H. Wood and E.H. Goldman, "Protective Coatings," in Superalloys II, C.T. Simms, N.S. Stoloff and W.C. Hagel (eds.), Chapter 13, (1987), 359-384.
12. R. Marvel, Materials Science and Engineering, A 120 (1989), 13-24.
13. R. Sivakumar and B.L. Mordike, Surface and Coatings Technology, 37, (1989), 139-160.

14. J.R. Nicholls, MRS Bulletin, (September 2003), 659-670.
15. G.W. Goward, Surface and Coatings Technology, 108-109, (1998), 73-79.
16. S.J. Grisaffe, "The Superalloys," C.T. Simms and W.Hagel (eds.), Wiley, NY, 1972.
17. M.P Brady, B. Gleeson, and I.G. Wright, Journal of Metals, (January 2000), 16-21.
18. J.A. Haynes, B.A. Pint, W.D. Porter, I.G. Wright, Materials at High Temperature, 21, (2004), 87-94.
19. B.A. Pint, I.G. Wright, W.Y. Lee, Y. Zhang, K. Prubner, and K.P. Alexander, Materials Science and Engineering, A245, (1998), 201-211.
20. B.A. Pint, Oxidation of Metals, 49, 531-560.
21. S. Alperine, P. Steinmetz, A.F. Constantini, P. Josso, Surface and Coatings Technology, 43/44, (1990), 347.
22. P. Kuppusami and H. Murakami, Surface and Coatings, 186, (2004), 377-388.
23. P.C. Patnaik, R. Thamburaj, and T.S. Sudarshan, Surface Modification Technologies III, T.S. Sundarshan, D.G. Bhat, eds, TMS, Warrendale, (1990), 759.
24. Y. Zhang, W.Y Lee, J.A. Haynes, I.G. Wright, B.A. Pint, K.M. Cooley, P.K. Liaw, Metallurgical and Materials Transaction, 30A, (1999), 2679.
25. M.C. Meelu, B.G. McMordie, M.H. Loretto, and A. Jones, Processing and Properties of Materials, (1992), 1250.
26. B. Gleeson, B. Li, D. Sordelet, U.S. patent pending, December 2004.
27. D.H. Boone and J.W. Fairbanks, Specialized Cleaning, Finishing and Coating Processes, Conference Proceedings, CA, ASM, Metals Park, Ohio, 1980, 357.
28. W.F. Schilling, NATO Advanced Workshop, Coatings for Heat Engines, Italy, April 1984.
29. Creech, G. E., Naik, S. K., Korinko, P.S., U.S. Patent No. 6406561, 2002.
30. B. Gleeson, Turbine Science and Technology, 2006.
31. H.C. Scott, J. Mater. Sci. Vol. 10, (1975), 1527-1535.
32. B.J. Zimmerman, "Rumpling Phenomenon in Platinum-Modified Ni-Al Alloys," MS Thesis, Iowa State University, (2005).
33. D.S. Rickerby, S.R. Bell and R.G. Wing, U.S. patent No. 5,981,091
34. M.A. DeCrescente and N.S. Bornstein, Corrosion-NACE, 24 (5), (1968), 127-133.
35. N.S. Bornstein, JOM 48, (November 1996), 37-39.
36. P. Hancock, Materials Science and Technology, 3 (7), (1987), 536-544.
37. "Phase Diagrams for Ceramists", vol. II (Westerville, OH: American Ceramic Society, (1969), fig. 2923.
38. J. Stringer, Materials Science and Technology, 3(7), (1987), 482-493.
39. P. Kofstad, "High Temperature Corrosion" Elsevier Applied Science, (1988), 468.
40. D.K. Gupta and R.A. Rapp, J. Electochem. Soc., 127, (1980), 2194.
41. N.S. Bornstein and M.A. DeCrescente, Trans. Met. Soc., AIME, 245, (1969), 1947.
42. N.S. Bornstein and M.A. DeCrescente, Corrosion, 26, (1970), 209.
43. N.S. Bornstein and M.A. DeCrescente, Met. Trans., 2, (1971), 2875.
44. J.A. Goebel and F.S. Pettit, Metall. Trans., 1, (1970), 1943.
45. J.A. Goebel and F.S. Pettit and G.W. Goward, Metall. Trans., 4 (1973), 261.
46. R.A. Rapp and K.S. Goto, Proc. 2nd Int. Symp. On Molten Salts, J. Braunstein and J.R. Selman, (eds.), Electrochemical Society, Pennington, NJ, (1981), 81.
47. D.A. Shores, NACE-6, R.A. Rapp (ed.), Houston, TX, (1983), 493.

48. R.A. Rapp, Corrosion Science 44, (2002), 209-221.
49. K.L. Luthra and D.A. Shores, J. of Electrochemical Society, 127 (1980), 2202-2210.
50. K.L. Luthra, Met. Trans., 13A, 1647, (1982), 1843.
51. K.L. Luthra, J. Electrochem. Soc., 132, (1985), 1293.
52. K.L. Luthra and J.H. Wood, Th. Sol. Films, 119, (1984), 271.
53. N. Otsuka and R.A. Rapp, J. Electrochem. Soc., (1990), 46.
54. K.P. Lillerud and P. Kofstad, Oxid. of Metals, Vol. 21, Nos. 5/6, (1984), 233-270.
55. K. Holthe and P. Kofstad, Corrosion Science, 20, (1980), 919.
56. B. Sand and P. Kofstad, MS Thesis by B. Sand, University of Oslo, 1980.
57. K.L. Luthra and D.A. Shores, J. of Electrochemical Soc., 127, (1980), 2202-2210.
58. R.H. Barkalow and F.S. Pettit, Proceedings of the 14th conference on gas turbine materials in a marine environment, Annapolis, MD, 1979, 493.
59. A.K. Misra, J. Electrochem. Soc., 133, (1986), 1038.
60. F.S. Pettit and G.H. Meier, in Superalloys Proceedings of International Symposium, 5th (1984), Gell Maurice (ed.), 651-687.
61. F.S. Pettit and C.S. Giggins, " Hot Corrosion" in Superalloys II, C.T. Simms, N.S. Stoloff and W.C. Hagel (eds.), Chapter 12, (1987), 327-358.
62. P. Singh and N. Birks, Werkst. Korros., 32(1980), 682.
63. G.M. Kim and G.H. Meier, in Z.A. Munir, D. Cubicciotti and H. Tagawa (eds.), "High Temperature Materials Chemistry IV", The Electrochemical Society, Pennington, NJ, (1988), 79.
64. Y.K. Kim, K. Przybylski and G.J. Yurek, in D.A. Shores and G.H. Yurek (eds.), "Fundamental Aspects of High Temperature Corrosion II" The Electrochemical Society, Pennington, NJ, (1986), 259.
65. F.H. Stott and M.F. Chong, in D.B. Meadowcroft and M.I. Manning (eds.), "Corrosion Resistant Materials for Coal Conversion Systems", Elsvier, Amsterdam, (1983), 491.
66. F.H. Stott, F.M. Chiang and C.A. Stirling, in M.F. Rothman (eds.) "High Temperature Corrosion in Energy Systems" AIME, Warrendale, PA, (1985), 253.
67. P. Deb, D.H. Boone and R. Streiff, Journal of Vacuum Science and Technology, A 3 (6), (1985), 2578-2581.
68. R. Streiff and O. Cerclier, Surf. and Coat. and Technol., 32, (1987), 111-126.
69. H. L. Du, J. Kipkemoi, D.N. Tsipas and P.K. Datta, Surface Coatings and Technology, 86/87, (1996), 1-8.
70. K. Godlewski and E. Godlewska, Materials Science and Engineering, 88, (1987), 103-109
71. K. Shirvani, M. Saremi, A. Nishikata, and T. Tsuru, Materials Science Forum, 461-464, (2004), 335-342.
72. G. R. Krishna, D.K. Das, V. Singh and S.V. Joshi, Materials Science and Engineering, A 251, 1-2, (1998), 40-47.
73. D. K. Das, V. Singh and S.V. Joshi, JOM, 52/1, (2000), 41-48.
74. J.A. Haynes, Y. Zhang, W.Y. Lee, B.A. Pint, I.G. Wright, K. M. Cooley, "Elevated Temperature Coatings: Science and Technology III", N. B. Dahotre, J.M. Hampikian (eds.), Warrendale, PA: TMS, (1999),185.
75. Y. Zhang, W.Y. Lee, J.A. Haynes, I. G. Wright, B. A. Pint, K. M. Cooley, P. K. Liaw, Metallurgical And Materials Transactions 30A, (1999), 2679.

76. R.E. Malush, P. Deb and D. H. Boone, Surface Coatings and Technology, 36, (1988), 13-26.
77. R.E. Malush, P. Deb and D.H. Boone, Surf. Coat. and Technol., 36 (1988) 13.
78. M. Dust, P.Deb D.H. Boone and S. Shankar, Journal of Vacuum Science and Technology, A, 4 (1986), 2571.
79. K. L. Luthra and O. H. LeBlanc, Jr., Materials Science and Engineering, 87 (1987), 329-335.
80. H. Singh, D. Puri, S. Prakash, Metall. and Mater. Trans. A, (2005), 36A(4), 1007.
81. E. Rocca, L. Aranda, M. Vilasi, P. Steinmetz, Mater. Sci. For. (2004), 461-464 (Pt. 2, High Temperature Corrosion and Protection of Materials 6, Part 2), 917-925.
82. M.R. Jackson, J.R. Rairden, Metallurgical Transactions, A 8, (1977), 1697.
83. J. Schaeffer, G.M. Kim, G.H. Meier, F.S. Pettit, E. Lang (ed.), Elesevier, Amsterdam, 231-267, (1989).
84. Y. Cadoret, M.-P. Bacos, P. Josso, V. Maurice, P. Marcus, S. Zanna, Materials Science Forum, 247, (2004), 461-464.
85. Y. Cadoret, D. Monceau, M.-P. Bacos, P. Josso, V. Maurice, P. Marcus, Oxidation of Metals, 64 (314), (2005), 185-205.
86. S. Hayashi, T. Narita, B. Gleeson, "Early-Stage Oxidation Behavior of $\tilde{\gamma}'$-Ni3Al-based alloys with and without Pt addition," Accepted in Mater. Sci. For., (2006).
87. D. Clemens, W.J. Quadakkers, L. Singheiser, High Temperature Corrosion and Materials Chemistry, ed. P.Y. Hou *et al.* (Electro. Soc., 1998), 134.
88. S.G. Young and D.L. Deadmore, Thin Solid Films, 73 (1980), 373-378.
89. M.W. Brumm and H.J. Grabke, Corrosion Science, 33(11), (1992), 1677-1690.
90. B.A. Pint, K.L. More, and I.G. Wright Oxidation of Metals, 59(3/4), (2003).
91. M.A. Phillips and B. Gleeson, Oxidation of Metals, 50, (1998), 399-429.
92. C. Leyens, B.A. Pint, I.G. WrightSurface and Coatings Technology, 133-134, (2000), 15-22.
93. G.J. Smeggil, A.W. Funkenbush, and N.S. Bornstein, Metallurgical Transactions, A17, 923, (1986).
94. J.L. Smialek , The minerals (Metals & Materials Society, 1989), 425.
95. B.A. Pint, Surface and Coatings Technology, 188-189, (2004), 71-78.
96. D.R. Coupland, C.W. Corti, and G.L. Selman, 525-536.
97. D.R. Coupland, I.R. McGill, C.W. Corti, and G.L. Selman, Environmental Degradation of High Temperature Materials, 26-29.
98. G.J Tatlock and T.J Hurd, Oxidation of Metals, 22, 5/6, (1984), 201-226.
99. G.J Tatlock and T.J Hurd, Werkstoffe und Korrosion, 41(12), (1990), 710-715.
100. G.J Tatlock and T.J Hurd, Platinum Metals Review, 31(1), (1987), 26-31.
101. E.J. Felten, Oxidation of Metals, Vol.10, No. I, (1976).
102. B. A. Pint, J. A. Haynes, K. L. More, I. G. Wright and C. Leyens, in T. M. Pollock, R. D. Kissinger, R. R. Bowman, K. A. Green, M. McLean, S. Olson and J. J. Shirra eds., Superalloys 2000, TMS, Warrendale, PA, p.629-38.
103. T. Izumi and B. Gleeson, Accepted in Materials Science Forum, (2006).
104. Y. Zhang, B.A. Pint, J.A. Haynes, I.G. Wright, Surf. Coat. Technol., 200 (5/6), (2005), 1259-1263.
105. V.K. Tolpygo, D.R. Clarke, Acta. Mater., 48 (2000) 3283.
106. D.R. Mumm, A.G. Evans, I.T. Spitsberg, Acta Mater., 49 (2001) 2329

107. G.H. Meier and F.S. Pettit, Surf. Coat. Technol., 39/40 (1989) 1.
108. S. Walston, in: K.A. Green, T.M. Pollock, H. Harada, T.E. Howson, R.C. Reed, J.J. Schirra, S. Walston (Eds.), Superalloys 2004, TMS, 579.
109. J.L. Cocking, P.G. Richards and G.R. Johnston, Surf. Coat. Technol., 36 (1988), 37.
110. J. Schaeffer, G.M. Kim, G.H. Meier and F.S. Pettit, E. Lang (Ed.), Elsevier, Amsterdam (1989) pp. 231-267.
111. G.W. Goward, Mater. Sci. Technol., **2** (1986) 194.
112. A. V. Dean "Investigation into the resistance of various nickel and cobalt base alloys to sea salt corrosion at elevated temperatures" NGTE report, January 1964.
113. E.W. Ross, Journal of Metals, 12, (December 1967).
114. D. Shifler, Office of Naval Research, Personal communication, 2006.
115. K.T. Chiang, F.S. Pettit, and G.H. Meier, in R.A. Rapp (ed.), High Temperature Corrosion Engineers, NACE-6, Houston, TX, (1983), 519-30.
116. Zhu Rizhang and Zheng Xiaoguang, Journal of Chinese Society of Corrosion Protection, 7, (1987), 207.
117. L.P. Kostin, L. L. Pluzhnikov, A. N. Ketov; Perm. Farm. Inst., USSR. Zhurnal Fizicheskoi Khimii, 49(9), (1975), 2235-7.
118. T.R. Ingraham, M.C.B. Hotz; Can. Metall. quarterly; Vol. 7 (3), (1968), 139-146.
119. J.J. Grisik, R. G. Miner and D. J. Wortman, Thin Solid Films, 73 (1980), 397-406.
120. I. Barin, Weinheim; New York: VCH, V1-2, 3rd edition, (1995).
121. Z. F. Gulvanitskaya, N. M. Pavlyuchenko, L. I. Blokhina, and G. N. Zviadadze, Izvestiya Akademii Nauk SSSR, Neorganicheskie Materialy, Vol.15-11, (1979).
122. C. Barrett, "A statistical analysis of elevated temperature gravimetric cyclic oxidation data of 36 Ni- and Co-base superalloys based on an oxidation attack parameter" NASA technical memorandum, 105934, (1992).
123. S. Hayashi, W. Wang, D.J. Sordelet, B. Gleeson, Metall. Mater. Trans., 36A (2005) 1769.